

University of Warwick institutional repository: <http://go.warwick.ac.uk/wrap>

**A Thesis Submitted for the Degree of PhD at the University of Warwick**

<http://go.warwick.ac.uk/wrap/3155>

This thesis is made available online and is protected by original copyright.

Please scroll down to view the document itself.

Please refer to the repository record for this item for information to help you to cite it. Our policy information is available from the repository home page.

# **Discrimination and Control in Stochastic Neuron Models**

A dissertation presented

by

Jing Kang

to

The Department of MOAC

in partial fulfillment of the requirements

for the degree of

Doctor of Philosophy

in the subject of

Computational Neuroscience

University of Warwick

Coventry, UK

July 2009

©2009 - Jing Kang

All rights reserved.

Thesis supervisor

Author

**Prof. Jianfeng Feng**

**Dr. Hugh P. C. Robinson**

**Jing Kang**

## **Discrimination and Control in Stochastic Neuron Models**

### **Abstract**

Major topics of great interest in neuroscience involve understanding the brain function in stimuli coding, perceptive discrimination, and movement control through neuronal activities. Many researchers are designing biophysical and psychological experiments to study the activities of neurons in the presence of various stimuli. People have also been trying to link the neural responses to human perceptual and behavioral level. In addition, mathematical models and neural networks have been developed to investigate how neurons respond and communicate with each other.

In this thesis, my aim is to understand how the central nervous system performs discrimination tasks and achieves precise control of movement, using noisy neural signals. I have studied, both through experimental and modelling approaches, how neurons respond to external stimuli. I worked in three aspects in details. The first is the neuronal coding mechanism of input stimuli with different temporal frequencies. Intracellular recordings of single neurons were performed with patch-clamp techniques to study the neural activities in rats somatosensory cortices *in vitro*, and the simplest possible neu-

ral model—integrate-and-fire model—was used to simulate the observations. The results obtained from the simulation were very consistent with that in the experiments. Another focus of this work is the link between the psychophysical response and its simultaneous neural discharges. I derived that under a widely accepted psychophysical law (Weber’s law), the neural activities were less variable than a Poisson process (which is often used to describe the neuron spiking process). My work shows how psychophysical behaviour reflects intrinsic neural activities quantitatively. Finally, the focus is on the control of movements by neural signals. A generalized approach to solve optimal movement control problems is proposed in my work, where pulses are used as neural signals to achieve a precise control. The simulation results clearly illustrate the advantage of this generalized control.

In this thesis, I have raised novel, insightful yet simple approaches to study and explain the underlying mechanism behind the complexity of neural system, from three examples on sensory discrimination and neural movement control.

# Contents

Title Page . . . . .	i
Abstract . . . . .	iii
Table of Contents . . . . .	v
Citations to Previously Published Work . . . . .	viii
Acknowledgments . . . . .	ix
Dedication . . . . .	xi
<b>1 Introduction</b>	<b>1</b>
1.1 Review . . . . .	2
1.1.1 Neurons are the brain's main signalling units . . . . .	2
1.1.2 Current approaches to studying neurons . . . . .	3
1.2 Research topics of interest . . . . .	4
1.2.1 Neural coding . . . . .	4
1.2.2 Motor control . . . . .	8
1.3 Original work . . . . .	9
1.3.1 Frequency discrimination and its underlying mechanisms . . . . .	9
1.3.2 Weber's law and neural discharge process . . . . .	10
1.3.3 Precise movement control . . . . .	11
1.4 Summary . . . . .	12
<b>2 A Brief Description to the Experiment</b>	<b>13</b>
2.1 Experimental techniques . . . . .	13
2.1.1 Patch-clamp technique . . . . .	14
2.1.2 Dynamic-clamp technique . . . . .	15
2.2 Experimental materials . . . . .	16
2.2.1 The experiment setups . . . . .	16
2.2.2 Solutions . . . . .	19
2.2.3 Fabrication of pipette . . . . .	20
2.2.4 Cell tissue . . . . .	22

---

2.3	Experimental procedure . . . . .	22
2.3.1	Preparation for bath solution and pH value adjustment . . . . .	22
2.3.2	Brain dissection and incubation . . . . .	23
2.3.3	Pipette preparation . . . . .	24
2.3.4	Pipette solution . . . . .	25
2.3.5	Equipment set up: software + hardware . . . . .	25
2.3.6	Forming a seal . . . . .	27
2.3.7	Patch-clamp whole-cell recording . . . . .	27
2.3.8	Stimulus protocol . . . . .	28
2.3.9	Data storage . . . . .	29
2.4	Final remarks . . . . .	29
<b>3</b>	<b>Temporal Frequency Discrimination</b>	<b>32</b>
3.1	Introduction . . . . .	33
3.2	Materials and Methods . . . . .	35
3.2.1	Biophysical Experiments . . . . .	35
3.2.2	Mathematical modelling . . . . .	38
3.3	Results . . . . .	45
3.3.1	Experiment . . . . .	45
3.3.2	Single neuron simulation . . . . .	46
3.3.3	Mechanism of various spiking patterns . . . . .	50
3.3.4	Gain enhancement . . . . .	53
3.4	Discussion . . . . .	55
3.4.1	Experimental responses . . . . .	56
3.4.2	Intrinsic oscillations in increasing response patterns . . . . .	58
3.4.3	Biological function . . . . .	58
3.4.4	Other possible neural models . . . . .	59
3.5	Final Remark . . . . .	60
<b>4</b>	<b>Link between Psychophysical and Neural Responses</b>	<b>63</b>
4.1	Introduction . . . . .	64
4.2	Methods . . . . .	67
4.2.1	Single neurons activities under Weber's law . . . . .	67
4.2.2	Superposition process of population neurons . . . . .	75
4.2.3	Competition attractor network . . . . .	77
4.3	Results . . . . .	80
4.3.1	Weber's law in firing rate . . . . .	80
4.3.2	Single neurons . . . . .	81
4.3.3	Weber's law in single neuronal ISIs . . . . .	82
4.3.4	Superposition of independent neural discharge process . . . . .	86
4.3.5	Superposition of correlated neural discharge process . . . . .	88

4.3.6	Neural network based on competition attractor network	90
4.4	Discussion	92
4.4.1	Nonlinear relation of stimulus-neuronal responses	93
4.4.2	Relation between the mean and variance of neural signal	95
4.4.3	Weber's law in single neuron or system level?	96
4.4.4	Variability of spatial correlation in spike train	98
4.4.5	Argument on Weber's law	99
4.5	Final Remarks	100
<b>5</b>	<b>A Novel Approach of Precise Movement Control</b>	<b>103</b>
5.1	Introduction	104
5.2	Young measure	108
5.3	Example 1: Saccadic eye movement model	110
5.3.1	Ordinary solution when $\alpha > 0.5$	114
5.3.2	Generalized control when $\alpha < 0.5$	118
5.3.3	Numerical simulations	126
5.4	Example 2: Straight-trajectory arm movement control	126
5.5	Discussion	133
<b>6</b>	<b>Conclusion and Future Work</b>	<b>135</b>
6.1	Conclusion and contribution	135
6.2	Further extensions	138
6.2.1	Frequency coding extension	138
6.2.2	More systematic study on links between psychophysical laws and neural activities	140
6.2.3	Applications of movement control	141
<b>A</b>	<b>Bibliography</b>	<b>143</b>
<b>B</b>	<b>Matlab code used in this thesis</b>	<b>155</b>
B.1	Code for modelling in chapter 3	155
B.2	Code for simulation in chapter 4	158
B.3	Code for simulation in chapter 5	164

## Citations to Previously Published Work

Large portions of Chapters 3, 4, and 5 will appear in the following three papers:

“Diversity of Intrinsic Frequency Encoding Patterns in Rat Cortical Neurons - Mechanisms and Possible Functions”, Jing Kang, Hugh P.C. Robinson, and Jianfeng Feng, PloS One (under revision).

“Weber’s Law Implies Neural Discharge More Regular than a Poisson Process ”, Jing Kang, Jianhua Wu, Anteo Smerieri and Jianfeng Feng, European Journal of Neuroscience (under revision).

“Controlling Precise Movement with Stochastic Signals”, Enrico Rossoni, Jing Kang and Jianfeng Feng, Biological Cybernetics (under revision).

# Acknowledgments

Completing this doctoral work has been a wonderful and cherishing experience. I have gained a lot during the past three years, not only in academia, but also in personal development.

I have been very lucky and privileged to have my current supervisor, Prof Jianfeng Feng and Dr. Hugh P. C. Robinson, who are undoubtedly the most intuitive and supportive supervisors anyone could ask for. Prof. Feng has always been encouraging and stimulating, and he is always with constant flow of good ideas all the time. He has fostered certainly the most open, friendly, collaborative and least competitive research group in our department. Dr. Robinson is always patient to his students and rigorous on research. He set me a very good example in academia that I will follow in my life. I benefit a lot from both my supervisors and am grateful to their supervision, guidance and care during the past three years.

From being an undergraduate student majored in Mathematics, I learnt to appreciate the skill and effort required for designing and carrying out biological experiments. I have widened my horizon as being a PhD student in interdisciplinary subjects of biology and mathematics, and have learnt to think as an experimentalist as well as a mathematician. I thank MOAC, the interdisciplinary centre, which provided a platform and options for me to explore the scientific field that I am interested in.

I would like to show my appreciation to my husband, Jianhua Wu. He is very supportive, understanding and helpful throughout my PhD study, espe-

cially the period of my write up. I feel very lucky to meet him and have him in my life, and I love him forever.

Throughout my PhD study, I was supported for three years by MOAC and department of Computer Science, University of Warwick, through the generosity of the University and my supervisor.

Prof. Feng and Dr. Robinson's other students and post-docs, both past and present, comprise a superb research group. The ability to bounce ideas off so many excellent minds has been priceless. They are not only my colleagues but also very good friends.

I would also like to thank my parents for their selfless love, understanding and supports all the time.

*Dedicated to my mother, Qing Mo  
my father, Yulin Kang  
my husband, Jianhua Wu*

# Chapter 1

## Introduction

The brain is capable of discriminating an enormous variety of events in a noisy environment and can precisely control movements that respond to external stimuli. All of these are accomplished by the brain using neurons (the main signalling units of the nerve system that process and transmit information by electrochemical pulses) and the connections among them. This discussion seeks to address these issues from three aspects: how the brain codes external stimuli in terms of individual neuron activities, how the variability of neural responses reflects the nature (such as intensity or frequency) of the stimuli, and how noisy neural signals control our movement accurately.

## 1.1 Review

### 1.1.1 Neurons are the brain's main signalling units

Neurons are cells specializing in the integration and propagation of electrical events. They form the fundamental units of information processing within the brain. All neurons are similar and share the same basic architecture, which includes the cell body (*soma*), the dendrites (for receiving signals), the axon (for emitting signals), and the presynaptic terminals (where the neuron transmits signals from one cell to another).

Neurons use action potentials as the primary way for information exchange and communication with each other as well as with muscles and other end organs (Williams and Herrup, 1988; Djuricic et al., 2004; Drachman, 2005). Action potentials are rapid, transient electrical impulses by which the neurons in the brain transmit information. Action potentials usually have amplitudes of 100 mV and a duration of approximately 1 ms. The neural signals (action potentials) are highly stereotyped throughout the nervous system (Adrian, 1932) although they are initiated by a great variety of events in the environment that impinge on our bodies—from light to mechanical contact, from odorants to pressure waves. Moreover, the information conveyed by an action potential is determined not by the form of the signal, but by the pathway along which the signal travels in the brain. Many researchers argue that two features of the conducting signal convey information: the number of action potentials (spike *frequency*) and the time intervals between them (interspike

intervals [*ISIs*]).

## 1.1.2 Current approaches to studying neurons

### Experimental techniques

Understanding basic electrophysiology is fundamental to appreciating the functions of neurons, neural systems, and the brain. The methods and techniques used in animal studies for understanding the electrical functioning of neurons in the central nervous system have been developed over many years. These methods differ fundamentally in the level of analysis, from subcellular levels (patch-clamping single-ion channels) to behavioural approaches (neuronal recordings in awake primates) (Bear et al., 1996; Kandel et al., 2000).

Using different recording techniques (Bear et al., 1996; Kandel et al., 2000; Dayan and Abbott, 2001), electrophysiological recordings can be divided into intracellular recordings (voltage-clamp, current-clamp, and patch-clamp technique) and extracellular recordings (single-unit recording and local field potentials).

Intracellular recording involves measuring voltage and/or current across the membrane of a cell, usually *in vitro*. To carry out an intracellular recording, the tip of a fine (sharp) microelectrode must be inserted inside a cell, so that the membrane potential can be measured. Such a recording is essential for understanding the mechanisms underlying the generation of action potentials in neurons. As my PhD studies relied exclusively on intracellular recording

techniques in experiments, this thesis will focus on this technique.

## **Neural modelling**

Understanding the principles of neural coding are of fundamental importance if we are to determine how brains work. The problem of how information is encoded and transmitted within the nervous system has challenged neurophysiologists for decades (Dayan and Abbott, 2001; Nicolelis, 2003). Many attempts to find and describe some general principles for such neural coding have been made.

In modelling, given a certain stimulus and the corresponding neural activity, the central problem is how to find a processing algorithm or coding principle that can adequately and accurately describe the input-output relationship between stimulus events and neural responses. This thesis attempts to explain how neurons code temporal information and how the coded neural signals are related to the behaviour at the perception level by building simple but reliable mathematical neural models. It further examines how the neural signals can precisely control movement using a novel mathematical approach.

## **1.2 Research topics of interest**

### **1.2.1 Neural coding**

The problem of neural coding has stimulated a large amount of research in neuroscience. The link between the activity of cells in the nervous system and

sensory perception remains one of the most significant and puzzling problems in neuroscience. Researchers have combined psychophysical and neurophysiological experiments, especially in behaving monkeys (Talbot et al., 1968; Romo and Salinas, 2003), to provide new insights into how several cortical areas integrate efforts to solve a discrimination task through neural coding.

Two critical components of the strategy associate neurons with perceptually relevant signals, especially within the cerebral cortex. The first is the formulation of a clearly defined perceptual task at the behavioural level. This is essential in order to provide an objective and rigorous framework in which to study perceptual events and the neuronal signals that underlie them. The second is an emphasis on the signals provided by individual neurons as these signals represent a fundamental medium of information transfer within the nervous system. Because of my interest in both components of the neural coding strategy, this thesis involves studies on single neuron activity in response to external stimuli as well as the possible link between neural activities and perceptual responses.

### **Encoding input temporal frequency in neural activities**

A central issue to neuroscience is understanding the mechanism of encoding and decoding of temporal sensory signals in the nervous system. However, due to the nonlinear input-output relations of neurons and their intrinsic stochastic properties, a solution to this problem remains elusive. A series of experiments on frequency discrimination has been conducted on monkeys

(Talbot et al. 1968; Mountcastle et al. 1969; Recanzone et al. 1992; Romo et al. 1999; Romo and Salinas 2003; Brody et al. 2003; Luna et al. 2005; Romo et al. 2006), in which the task for monkeys was to discriminate the frequencies of two sequential stimuli in the form of both mechanical vibrations applied on the finger tip and electrical currents pulsed applied directly to the single neurons in somatosensory cortex. Single-cell recordings *in vivo* (Salinas et al. 2000) indicated that a subset of neurons in S1 and S2 areas do modulate their firing rates with the input frequency and that the output firing rate may decrease, increase, or remain constant in different areas of the somatosensory cortex as the input frequency increases.

However, it is unclear if these heterogeneous frequency response functions of neurons in different areas of the cortex are caused by the local neural network effect and receptor properties or if it is the intrinsic characteristics of single neurons that are sensitive to the stimulus frequency. Hence, during my PhD studies, I performed single-neuron recordings *in vitro* by injecting artificial stimulus at various frequencies. It was found that some of the neurons did modulate their firing rates with the temporal input frequency, showing the discrimination ability of a single neuron in encoding input information. The rest of the recorded neurons were not sensitive to various input stimulus frequencies. This observation indicated that single neurons might be capable of discriminating input temporal frequencies based on their firing rates.

In simulations, many researchers question the ability of the leaky integrate-and-fire (LIF) model to describe the behaviours of real biophysical neurons

because of its simplicity. However, others believe LIF is sufficient for simulating and predicting spiking neuron behaviours with a high accuracy (Jolivet et al., 2004, 2006) and have used LIF in modelling the coding mechanisms at the single neuron level (Feng, 2001; Koulakov et al, 2002; Feng and Brown, 2004; Miller and Wang, 2006). In this study, the LIF model will be used to simulate neural responses in the experiments, as it is simple and analytically tractable, and the results of experiments and modelling are consistent.

### **Perception of stimulus intensity on neuronal level**

The capacity of the sensory system to extract information about the magnitude of the stimulus is important for sensory discrimination. However, the transformation between sensory cortical neuronal signals and the perceptual responses remains unclear, although many researchers have intensively studied the link between the neuronal activity and psychophysical judgment of sensory processing (Shadlen and Newsome, 1994; Sawamura et al., 2002). People believe that the quantitative features of sensory stimuli measured in psychophysical studies are signalled by the firing rate of the activated population of sensory neurons while the details of neural activity encode the intensity and time course of the sensory experience.

One of the widely accepted psychophysical laws is Weber's law, by which psychophysicists Weber and Fechner quantified the intensity of sensations in the form of mathematical laws that allowed them to predict the relationship between stimulus magnitude and sensory discrimination. This phenomenon

has been observed in a wide range of moderately intense stimuli experiments in sensory perception (in terms of weights, pure tones, light intensities, sizes, distances, numbers, etc.), but it still lacks a link between this psychophysical property and neuronal activity. This thesis worked out a possible link between this psychophysical law and its corresponding neural discharge process.

### 1.2.2 Motor control

In contrast to sensory systems, which transform physical energy into neural signals, motor systems produce movement by translating neural signals into a contractile force in muscles. Motor control of human movement has been a subject of investigation for several decades. In a broad sense, the motor control problem can be stated as the generation of the muscle activations that best fit the purpose of a movement, given the proprioceptive and external world information available through the body's sensors (Campos and Dalado, 2009).

Despite the complexity of motor control problems, the nerve system shows amazing regularities when generating movement. Early research has focused directly on the kinematic regularities<sup>1</sup>, developing theories expressed in terms of the kinematic variables. Dynamic variables<sup>2</sup> were subsequently used to find a unifying principle that fits a broader range of movements. A major breakthrough in understanding the nature of human motor control was introduced

---

<sup>1</sup>*Kinematics* is a branch of classical mechanics that describe the motion of objects without considering the causes leading to the motion.

<sup>2</sup>*Dynamics* is the study of the relationship between the motion of objects and its causes.

by Harris and Wolpert (1998), who suggested that noise in control signals within the sensorimotor loop was a determining factor in overall motor behaviour. In their papers, the concept of movement planning was regarded as an integration of kinematic and dynamic concepts. They suggested that movement planning relied on the minimization of the final position variation. This approach used an optimization procedure, taking the end-point variance as the quantity to minimize. Harris and Wolpert (1998) pointed out the fact that muscle commands were corrupted by noise and the noise increased linearly with the amplitude of the command signals (Schmidt et al., 1979; Meyer et al., 1988; Jones et al, 2002; Hamilton et al., 2004).

The current work generalized the signal-noise relation and proposed a new method in achieving a precise control in the presence of noisy neural signals based on the model proposed by Harris and Wolpert (1998).

## **1.3 Original work**

### **1.3.1 Frequency discrimination and its underlying mechanisms**

Extracellular recordings of single neurons in primary and secondary somatosensory cortices of monkeys *in vivo* have shown that their firing rate can increase, decrease, or remain constant in different cells, as the external stimulus frequency increases. I observed similar intrinsic firing patterns (increas-

ing, decreasing or constant) in rat somatosensory cortex in vitro, when stimulated with oscillatory input using conductance injection (dynamic clamp). The underlying mechanism of this observation is not obvious, and presents a challenge for mathematical modelling.

I proposed a simple principle for describing this phenomenon using a leaky integrate-and-fire model with sinusoidal input, an intrinsic oscillation and Poisson noise. Additional enhancement of the gain of encoding can be achieved by local network connections amongst diverse intrinsic response patterns. I demonstrated this principle using higher-order comparison neurons to illustrate the necessity of these opposite (increasing and decreasing) output firing patterns.

This work sheds light on the possible cellular and network mechanisms underlying these opposing neuronal responses, which serve to enhance signal detection.

### **1.3.2 Weber's law and neural discharge process**

Weber's law is one of the basic laws in psychophysics, but the link between this psychophysical behavior and the neuronal response has not yet been established.

I carried out an analysis on the spike train statistics when Weber's law holds, and found that the efferent spike train of a single neuron is less variable than a Poisson process. For population neurons, Weber's law is satisfied only when the population size is small (less than 10 neurons). However, if

the population neurons share a weak correlation in their discharges and individual neuronal spike train is more regular than a Poisson process, Weber's law is true without any restriction on the population size. Biased competition attractor network also demonstrates that the coefficient of variation of interspike interval in the winning pool should be less than one for the validity of Weber's law.

Our work links Weber's law with neural firing property quantitatively, shedding light on the relation between psychophysical behavior and neuronal responses.

### **1.3.3 Precise movement control**

In a noisy system such as the nervous system, movements can be precisely controlled as experimentally demonstrated. However, the existing theory of motor control fails to provide viable solutions.

This work used a generalized approach to the nonconvex optimization problems with the Young measure theory and demonstrated that a precise moment control is possible even with stochastic control signals. Two numerical simulations were presented, with a clear demonstration of significant improvement of movement precisions. This generalized approach paves a new way for solving optimization problems when a precise control is needed.

## **1.4 Summary**

The major contributions of this PhD study are the investigation of the neural coding to distinguish the temporal frequencies of the stimulus, the derivation of the link between psychophysical perception and neural activity on discrimination of stimuli intensity, and the proposal of a constructive approach to precisely control the movement through neural signalling.

Chapter 2 presents a detailed description of the experiment. Chapters 3, 4 and 5 provide the main results from the past few years of my PhD study. Stimuli frequency coding mechanisms are examined in Chapter 3, using both experiment and modelling approaches. Chapter 4 studies the link between the psychophysical response and neural discharge process, while Chapter 5 studies the effect of neural signal noise, where a novel approach was applied in precise movement control. The conclusion and further research are discussed in the last chapter.

## **Chapter 2**

# **A Brief Description to the Experiment**

Experiments on the study of temporal frequency decoding ability of single neurons *in vitro* had been carried out at Dr. Hugh P. C. Robinson's lab at the Department of Physiology, Development and Neuroscience, University of Cambridge, UK. In this chapter, I would like to give a brief description on the experimental techniques, materials, and procedures that I learned in Dr. Robinson's lab during the past few years.

### **2.1 Experimental techniques**

The techniques commonly used in neuroscience on the study of single-cell behaviour *in vitro* involve patch clamp (Sakmann and Neher, 1995) and dynamic clamp (Sharp et al., 1993). Dynamic clamp is also called conductance

injection technique (Robinson and Kawai, 1993).

The patch-clamp and dynamic-clamp techniques have been intelligently combined by Dr. Hugh P. C. Robinson to carry out intracellular recordings on rat cortical brain slices. The experiment main devices include a Multiclamp 700B (Molecular Devices, Union City, CA), a conductance injection amplifier (SM-1) with software running on a DSP analog board (SM-2, Cambridge Conductance, Cambridge, UK), micromanipulators for positioning the patch pipette, an infrared microscope, and a customer software written in Matlab (MathWorks, Natick, MA) to design artificial stimulus and store data of neuronal response.

### **2.1.1 Patch-clamp technique**

Patch-clamp technique was firstly developed by Erwin Neher and Bert Sakmann. They used this technique to demonstrate single channels in a biological membrane (Neher and Sakmann, 1976). Nowadays, patch clamp is an extremely powerful and versatile method for studying electrophysiological properties of biological membranes.

The patch-clamp technique refers to both voltage clamp and current clamp of measures using patch-clamp type micropipettes. This electrophysiological method allows one to monitor the changes in membrane potential in response to current flowing cross ion channels (current clamp), or to manipulate the voltage of the whole cell to a command value to study the current flowing across membrane (voltage clamp).

In my experiments, I used the tight-seal whole-cell configuration to record from the soma of cortical neurons in brain slices of rat, and modify their internal environment by injecting various stimuli using patch-clamp pipette.

### **2.1.2 Dynamic-clamp technique**

Though the dynamic clamp is a relative new technique developed in the recent 15 years (Robinson and Kawai, 1993; Sharp et al., 1993), it has become a widely used tool to study the neural system at the cellular and circuit levels around the world. The dynamic clamp uses computer simulation to introduce artificial conductance (that is why it is called conductance injection technique as well) into biological neurons. The term 'dynamic clamp' refers to a variety of hardware and software implementations. The dynamic clamp can effectively alter the conductance of a neuron by using the measured membrane potential to control the amount of current injected into a neuron. The reversal potentials set in the conduction injection amplifier  $E_{\text{AMPA}}$ ,  $E_{\text{NMDA}}$  and  $E_{\text{GABA}}$  were set to be 0, 0, and  $-70$  mV, respectively in my experiments.

With the help of modern computer technology, dynamic clamp is used in my experiment with good performance to measure the membrane response voltage at the presence of artificially designed conductance stimuli.

## **2.2 Experimental materials**

The experimental materials section includes the experiment setups, solutions, pipettes, and cell tissues.

### **2.2.1 The experiment setups**

The setups in the experiment during recording includes (Fig. 2.1, picture taken at the lab):

#### **Vibration isolation table and Faraday cage**

The vibration isolation table can reduce the vibrations beyond a few Hertz, which is sufficient for the purpose of patch clamping because mechanical stability is crucial for patch clamp stable recording.

Faraday cage is surrounding the patch-clamp setup, and its main function is to shield the sensitive patch-clamp preamplifier from electrical noise.

#### **Infrared microscope**

The infrared microscope is used for cell visualization, and it is placed on the vibration isolation table within the Faraday cage. The usefulness of the infrared microscope is at the observation of the cell during measurement, and even more importantly, is at the approach to the cell by the patch pipette for seal formation which requires a good optical visualization.

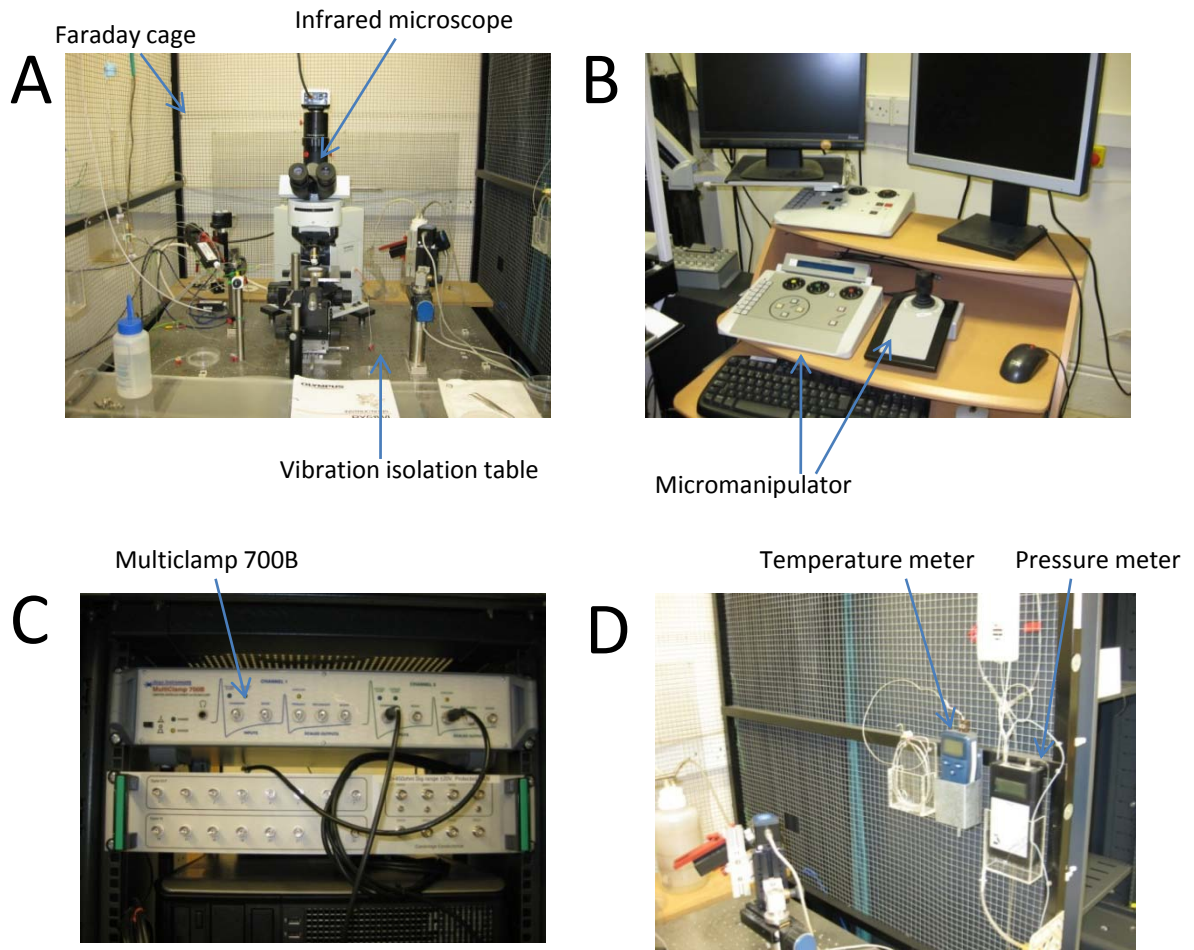


**Fig. 2.1** Experimental setups. The panels illustrate the major instruments used in my experiment, but there are some apparatus not shown here. (A) vibration isolation table with Faraday cage, infrared microscope, (B) controller units for manipulator, (C) Patch clamp amplifier, and (D) temperature and pressure meters.

### **Micromanipulator**

This manipulation device can precisely control the movement of the patch pipette and hold the amplifier probe for positioning the attached patch pipette in the sub-micrometer range. The position of the pipette needs to be free of drift after seal formation to maintain stable recording.

### **Stimulus generator and patch clamp amplifier**

Multiclamp 700B together with Matlab software can design the stimuli and apply a steady command current or voltage to the soma through the pipette electrode under the whole-cell recording.

### **Data recording device**

Computer is used as the data recording device to store the time-varying membrane potential values at different designed current or conductance stimuli.

### **Thermal machine and temperature meter**

During the whole-cell recording, the temperature of the cell bath solution is kept at biophysical temperature between 32-34°C. The temperature of the bath solution is maintained by the thermal machine and monitored by the temperature meter.

**Pressure meter**

Pressure meter indicate the positive pressure (usually generated by mouth) applied to the patch pipette interior environment to make sure the pipette intracellular solution will not be contaminated when the pipette tip dips into the bath solution.

**Perfusion device**

The bath solution around the cell in the recording device is maintained fresh throughout the experiment with oxygenated bath solution fusing in from one side of the recording device and being pumped out from the other side, such that the tissue slice is kept at good status as long as possible.

**2.2.2 Solutions**

Bath solution refers to the solutions applied to the extracellular surfaces of the membrane, where the cells are place in. Pipette solution is the solution contact with the internal cytoplasmic surface of the membrane which is held in the pipette tip surrounding the electrode. Composition of the bath solution and the pipette solution used in the experiments with brain slice neurons are given in Table 2.1. The pipette solution is filtered before transferred into the pipette tips, because contamination of the pipette tip can prevent formation of seal.

Table 2.1: Ingredients of solutions.

	Bath solution (mM)	Pipette solution (mM)
NaCl	125	-
KCl	2.5	30
CaCl <sub>2</sub>	2	-
NaHCO <sub>3</sub>	25	-
Glucose	25	-
phosphocreatine	-	10
NaH <sub>2</sub> PO <sub>4</sub>	1.25	-
K-gluconate	-	105
Buffer	pH 7.4, oxygenated with 95% O <sub>2</sub> and 5% CO <sub>2</sub>	10 HEPES, 4 ATP and 0.3 GTP, pH 7.35 with KOH

### 2.2.3 Fabrication of pipette

The following equipment and materials are used for the fabrication of the patch pipettes.

#### Pipette puller

This device pulls the glass capillary tubes through a metal filament and uses gravitation to pull the glass apart as the center of the capillary starts to melt the glass.

#### Pipette capillary

The pipette capillary is a thin-walled glass capillary containing an internal glass filament that aids the filling of the pipette with electrolyte solution.

A



B



**Fig. 2.2** Brain dissection tools and brain slice incubator. (A) The tools of dissection prepared according to the order they are used. (B) Brain slices in incubators being oxygenated and incubated at the physiological temperature for recording.

## **2.2.4 Cell tissue**

The method we used for brain slice is the 'blow and seal' technique (Stuart et al., 1993). The detailed procedure to prepare for the brain slice tissue and perform the whole-cell recording is presented in the next section.

## **2.3 Experimental procedure**

The following procedure is presented by the time order of carrying out experiments.

### **2.3.1 Preparation for bath solution and pH value adjustment**

The constituent of the bath solution (extracellular solution) is listed in Table 2.1. The chemicals (NaCl 7.305 g, KCl 0.186 g, NaHCO<sub>3</sub> 2.1 g, NaH<sub>2</sub>PO<sub>4</sub> 0.15 g and glucose 4.5 g) stored in a cool dry place were measured by an electric scale, and the stock solutions (CaCl<sub>2</sub> 2 ml, MgCl<sub>2</sub> 1 ml and Glycine 100  $\mu$ l) kept in a refrigerator were measured by the marked pipette with different volumes. To prepare the bath solution, all components were mixed up with distilled water up to 1 L with the solution being stirred by a magnetic stirring bar inside the measure beaker all the time.

The pH value was adjusted to 7.4 by gassing the solution with 95% O<sub>2</sub> and 5% CO<sub>2</sub> at medium speed of the gas flow for at least 30 minutes, making

the bath solution mimic the natural extracellular environment of the cell.

### **2.3.2 Brain dissection and incubation**

#### **Preparation for dissection**

While the bath solution is being oxygenated for pH adjustment, the tools for the dissection were prepared simultaneously. In accordance with United Kingdom Home Office guidelines for Schedule 1 killing, the surgeon equipments for killing a rat include a screw driver (for neck dislocation), a big scissors (for decapitation), a smaller scissors (for cutting off the head skin), a special designed scissors (for cutting of the skull), a nipper (for peeling off the skull and exposing the brain), a small specula (for getting the brain out of the skull), a blade (for cutting off the unwanted brain tissue) and a super glue (for fixation of the brain left-hemisphere for dissection). Also, a platform for holding the brain slice with the gauze placed at the bottom is prepared beforehand, and the platform is placed inside the bath solution in a medium size beaker with oxygen perfusing at lower flow to prevent killing the cells at high speed of gas flow (Fig. 2.2).

Then, a postnatal days 7-21 Wistar rat is decapitated (killed according to United Kingdom Home Office guidelines). The left-hemisphere of brain is kept for experiment. Rest of the brain and body are disposed for recycle. This procedure takes no longer than 1.5 minutes, usually completed within 1 minute. The brain left-hemisphere is immediately submerged in ice-cold oxy-

generated bath solution. Cooling of the tissue is particularly important, minimizing the damages from anoxia and improves the texture of the tissue for slicing.

### **Dissection**

The surface of the left-hemisphere is glued to the stage of the slicer. The slicing chamber is then immediately filled with ice-cold bath solution. 300  $\mu\text{m}$  thick sagittal brain slices were obtained with healthy cells near the surface using vibrating tissue slicer. The first slice is discarded before slices of a uniform thickness are obtained. The slicing procedure is monitored continuously, by sucking off the contaminant glutamate released from the brain while slicing and refilled with clean ice-cold bath solution.

### **Incubation of slices**

Each slice is immediately placed in a holding chamber containing oxygenated bath solution at room temperature for at least 30 min before recording. The condition of the tissue is optimal over the first 3 or 4 hours, however, stable recordings can still be obtained 10-12 hours after slicing.

### **2.3.3 Pipette preparation**

The capillary is placed in the centre of the pulling machine vertically and it is a two-step pull mechanism: the first pull (adjust to mark 70 degree) softens the glass and pulls it a short distance to thin the capillary 200-400  $\mu\text{m}$  at

the narrowest point over 7-10 mm region (central symmetrical breaks), after which the 2nd pull (adjust to mark 50 degree) with lower heat separates the capillary, yielding two pipettes with large-diameter tips. The pipette tips are typically of 5-10 M $\Omega$  of resistance. The pipette tips need to be used within 5-8 hours after being made.

### **2.3.4 Pipette solution**

Pipette solutions (intracellular solution) are frozen in smaller stocks and thawed before experiment. Supplements (ATP + GTP solution) are added from frozen stocks to the pipette-filling solution as needed shortly before the experiment. The pipette solution is filtered with a syringe filter and then back filled to the pipette tips with a long tip cartridge. The bubbles in the pipette tips can be removed by tapping the side of the pipette. The pipette tip is partially filled, just far enough to make reasonable contact with the electrode wire.

### **2.3.5 Equipment set up: software + hardware**

#### **Placing brain slice**

One brain slice is placed into a circular, glass bottomed recording chamber. The slice is held in place with a grid of parallel threads. The chamber holds a volume of about 1 ml bath solution and during recording is perfused with oxygenated bath solution at a flow rate of 1 to 2 ml/min, and the overflow

is sucked out by a pipe to avoid flooding over the sample.

### **Ground and heat the bath solution**

The ground electrode is intact with the bath solution so that the extracellular solution is zeroed to ground potential and the recorded intracellular potential is the membrane potential.

The bath solution is heated to mimic the biophysical temperature 32-34°C.

### **Software adjustment**

The softwares used in the experiment include Multiclamp (for patch clamp stimuli amplifying and injection control), Capture Infinity (infrared microscope software), and Matlab m-file ginj.m (to design stimulus of interests). Multiclamp mode is switched to voltage-clamp mode first, measuring the pipette tip resistance (5 to 10 M $\Omega$ ) by applying a step voltage (2 mV) written by Matlab. Before the pipette is inserted into the bath solution, the current trace should be flat except for very small capacitive transients caused by the stray capacitance of the pipette. Membrane potential, including stated reversal potential for injected conductances, was corrected afterwards for the pre-nulling of the liquid junction potential (10 mV). Signals were filtered at 6-10 kHz (Bessel), sampled at 20 kHz with 16-bit resolution.

## **Visualization of the neurons**

Brain slices are viewed with an upright compound microscope using 64 contrast optics. Initially, the slice is illuminated with visible light and the pipette tip should be adjusted to a position where the image captured by the infrared camera appears darkest in the center of the infrared image.

### **2.3.6 Forming a seal**

Positive pressure is applied to the recording patch pipette so that the solution pushes the connective tissue away from the pipette tip as it advances through the slice. The approaching angle of the pipette tip to the target cell is approximately 15 degree to the horizontal. After touching the targeted cell membrane, the positive pressure (60-100 Pa) is released and the applied suction (slight negative pressure) leads to formation of a tight seal (high resistance is in excess of  $10^9\Omega$ ) onto the cell membrane at the contact area, which is characterized by the current trace becoming essentially flat. The success rate for formation of high- $G\Omega$  seal can be as high as 100% when recording are made from large structures such as the soma.

### **2.3.7 Patch-clamp whole-cell recording**

After the forming the 'gigaseal', the fast capacitance compensation is adjusted to cancel the transient caused by the capacitance of the pipette holder and pipette wall. Pulses of suction are applied to the pipette interior until a

sudden increase in the size of the capacitive transients is observed. This additional current reflects the contribution of the cell membrane to the pipette input capacitance following the destruction of the patch membrane. An alternative method to break the patch membrane is to apply to the pipette very short volt pulses (10-500  $\mu$ s) of large amplitude to induce membrane breakdown ('zapping'). Series resistances were in the range of 10-20 M $\Omega$  and were measured and compensated for by the Auto Bridge Balance function of the Multiclamp 700B. Then, artificial current and conductance stimuli can be applied to the interior of the cell and the membrane voltage trace is recorded according.

### **2.3.8 Stimulus protocol**

After whole-cell recording mode is on, sequence of designed stimuli can be applied to the target neuron. Step current injections from negative value (-50 or -100 pA) gradually increasing with a fixed step size (50 pA) were applied usually at the beginning, in order to assess the different feasible range of current for stimulating each individual neuron. In between each sweep, an interval normally of 10 times length of the stimulus time was allowed for cell recovery. A small hyperpolarizing holding current (< 50 pA) can be applied if necessary to ensure a fixed resting potential (between -65 to -75 mV) between sweeps.

### **2.3.9 Data storage**

Data recorded from single neuron membrane potential is stored automatically by the computer in the form of .mat file executed by Matlab, including the designed stimulus program, the time-variant membrane potential values and sample frequency.

## **2.4 Final remarks**

The patch-clamp and dynamic-clamp techniques are widely used with a lot of advantages enabling us to study the neuronal properties, but there are still artefacts that need to be improved during the experiment. The following are a few examples that cause the inaccuracy of recordings in my experiment, and sometimes they even give unreliable recorded data.

### **The offsets potential (liquid junction potential)**

Liquid junction potentials are variable offset, depending on ionic conditions. Some offsets arise in the external circuit (e.g. in patch pipette, experimental chamber, or at the silver chloride electrode).

### **Solution contamination**

Contaminations of the solution with foreign substances that might affect ion channels are very difficult to eliminate completely, because containers,

syringes, tubings, needles or filters may release small amounts of leachable substances or detergents into the solution.

### **Electrode coating**

The electrode in the pipette holder is silver wires coated with AgCl. This coating gets scratched during multiple exchanges of pipettes and may also degrade with time when large currents are passed (effectively dissolving the AgCl coating as the  $\text{Cl}^-$  ions are released into the saline). Electrodes need to be regularly chlorided, or shifts in the electrode potential may become so severe that voltage drifts become noticeable in the course of an experiment, making the measurements inaccurate.

### **Brain slices**

Neurons in the brain slices are relatively silent compared with the recordings in an intact brain, because each neuron receives much less ongoing synaptic inputs. Neurons in slices are studied in an environment that is significantly different from that in which they normally operate.

However, despite all these artifacts, the most advantage of this technique is that it breaks down barriers between mathematical modelling and experimental electrophysiology by allowing theorists to model 'in the dish' and experimentalist to perturb their system in ways that, only a mathematicians

would imagine. In my experiments, I combine the control and flexibility of computer simulation with the accuracy and realism of electrophysiological recording, using computer modelling as an experimental tool. The experimental results on single cell discrimination ability on stimulus temporal frequency are presented in the following chapters.

## **Chapter 3**

### **Temporal Frequency**

#### **Discrimination**

Cortical neurons in the somatosensory areas show disparate patterns of tuning to oscillatory input as the frequency of the input increases. A subset of neurons generates more action potentials at higher stimulus frequencies, and is relatively less responsive at low frequency. Another type behaves in an opposite way, decreasing its firing rate with respect to the increasing stimulus frequency. Other neurons show an essentially constant firing frequency as input frequency is varied. These patterns are observed in response to either mechanical vibrations of the skin, or to direct intracellular sinusoidal current stimulation.

In this chapter, I carried out experiments to test if this phenomenon could be due to the intrinsic properties of different neurons, or if it requires a more

complicated explanation, for example particular local network interactions, receptor properties or input connectivity. I found that single neurons in brain slices were sensitive to the temporal frequency of conductance inputs mimicking oscillatory synaptic input, and were able to generate both increasing and decreasing as well as constant responses with respect to the stimulus frequency, depending on the neuron and on the stimulus amplitude and offset. I am able to account for these observations using a simple integrate-and-fire neuronal model and to suggest a possible underlying mechanism. This work reveals the powerful sensory discrimination capabilities of single neurons and simple neuron models, and proposes a minimal mechanism of input frequency encoding in the brain.

### 3.1 Introduction

In a series of experiments on somatosensory frequency discrimination in monkeys, responses of single neurons in somatosensory cortex to mechanical vibrations on the finger tips or direct oscillatory electric current stimulation were recorded (Romo, Brody et al. 1999; Salinas, Hernandez et al. 2000; Brody, Hernandez et al. 2003; Romo and Salinas 2003). A subset of neurons in primary (S1) and secondary (S2) somatosensory cortices showed modulations of their firing rates with the temporal input frequency ( $F$ ). Most neurons in S1 tune with a positive slope to the input frequency, but some neurons in S2 behave in an opposite way, with a high firing rate at low stimulus frequency

which is reduced at high frequency. It is unclear if these heterogeneous frequency response functions of neurons in different areas of somatosensory cortex are due to local neural network properties, receptor properties or input connectivity, or to the intrinsic integrative characteristics of single neurons.

To investigate the characteristics of single neurons, I performed whole-cell patch clamp recordings from the somas of layer 2/3 pyramidal neurons in rat somatosensory cortex *in vitro*, (Sakmann and Neher 1995), and stimulated firing by directly injecting oscillatory artificial synaptic conductance and current into neurons through the patch-clamp pipette (Robinson and Kawai 1993). I found that some neurons generated a higher firing rate as stimulus frequency increased, while others showed a reduced firing rate at high frequency. I also observed a lot of frequency-insensitive neurons, which fired at a constant rate as stimulus frequencies vary. In addition, the types of neuronal responses (increasing, decreasing or constant) were affected in some cases by the mean, or offset, of stimulus intensity (see Fig. 3.1C, stimulus illustration). With the diversity of firing patterns observed in individual neurons in my experiments, it appears possible that the intrinsic properties of neurons can explain much of the diversity of response patterns observed *in vivo*. A reasonable goal in modelling these responses would be a simple model which could generate these different patterns as its parameters are varied.

The leaky integrate-and-fire (LIF) model is simple, analytically tractable and computationally efficient, compared with other complex biophysical models (e.g. Hodgkin-Huxley models). A number of studies have concluded that

LIF neurons can not be used for simulating temporal frequency coding mechanisms at the single neuron level (Feng 2001; Koulakov, Raghavachari et al. 2002; Feng and Brown 2004; Machens, Romo et al. 2005; Miller and Wang 2006), and that the LIF model is blind in the temporal domain owing to the fact that its efferent firing rate is independent of the input temporal frequency (Feng and Brown 2004). This is true under certain circumstances, but not all. Here, I have managed to generate output firing rates in LIF models with three different patterns (increasing, decreasing or flat) as a monotonic function of the input frequency  $F$ , under a wider, but still biologically feasible, parameter region than considered previously. I am able to provide a simple mathematical explanation for the underlying mechanism of these three different firing patterns in the LIF model. I have also studied the behavior of prototypical networks of these neurons, introducing higher order neurons which integrate the response of heterogeneously-responding neurons, so enhancing the gain of frequency encoding.

## **3.2 Materials and Methods**

### **3.2.1 Biophysical Experiments**

#### **Electrophysiology**

300  $\mu\text{m}$  sagittal slices of somatosensory cortex were prepared from post-natal days 7 – 21 Wistar rats (killed according to United Kingdom Home

Office guidelines), in chilled solution composed of the following (in mM): 125 NaCl, 25 NaHCO<sub>3</sub>, 2.5 KCl, 1.25 NaH<sub>2</sub>PO<sub>4</sub>, 2 CaCl<sub>2</sub>, and 25 glucose (oxygenated with 95% O<sub>2</sub>, 5% CO<sub>2</sub>). Slices were held at room temperature for at least 30 min before recording and then perfused with the same solution at 32 – 34°C during recording. Whole-cell recordings were made from the soma of pyramidal neurons in cortical layers 2/3. Patch pipettes of 5 – 10 MΩ resistance were filled with a solution containing of the following (in mM): 105 K-gluconate, 30 KCl, 10 HEPES, 10 phosphocreatine, 4 ATP, and 0.3 GTP, adjusted to pH 7.35 with KOH. Current-clamp recordings were performed using a Multiclamp 700B (Molecular Devices, Union City, CA). Membrane potential, including stated reversal potential for injected conductances, was corrected afterwards for the pre-nulling of the liquid junction potential (10 mV). Series resistances were in the range of 10 – 20 MΩ and were measured and compensated for by the Auto Bridge Balance function of the Multiclamp 700B. Signals were filtered at 6 – 10 kHz (Bessel), sampled at 20 kHz with 16-bit resolution, and recorded with custom software written in Matlab (MathWorks, Natick, MA).

### **Conductance injection**

Recorded neurons were also stimulated using conductance injection, or dynamic clamp (Robinson and Kawai, 1993; Sharp et al., 1993; Destexhe, 2009). A conductance injection amplifier (SM-1) or software running on a DSP analog board (SM-2; Cambridge Conductance, Cambridge, UK) imple-

mented multiplication of the conductance command signal and the real-time value of the driving force, with a response time of  $< 200$  ns (SM-1) or  $< 25$   $\mu$ s (SM-2), to produce the current command signal. Voltage dependence of NMDA current was simulated by multiplying the command signal by an additional factor  $(1 + 0.33[\text{Mg}^{2+}] \exp(-0.06V))^{-1}$  (Harsch and Robinson, 2000), where  $V$  is the membrane potential and  $[\text{Mg}^{2+}]$  is the extracellular magnesium concentration set to 1 mM. The reversal potentials  $E_{\text{AMPA}}$ ,  $E_{\text{NMDA}}$  and  $E_{\text{GABA}}$  were set to be 0, 0, and  $-70$  mV, respectively.

### Stimulus protocol

Randomly permuted sequences of stimuli were calculated for each combination of different values of the mean offset, amplitude and frequency of the sinusoidal input (Fig. 3.1C stimulus), either as injected positive current or excitatory conductance, in order to obviate the effects of any progressive adaptation to monotonic changes of any single parameter. Individual sweeps consisted of 2 s of stimulus, with data from the initial 200 ms discarded to eliminate transient onset responses. A 15 second interval between sweeps was allowed for recovery. A small hyperpolarizing holding current ( $< 50$  pA) was applied if necessary to ensure a fixed resting potential between sweeps, usually between  $-65$  to  $-75$  mV. Step current injections from  $-100$  pA gradually increasing with a step size of 100 pA were applied at the beginning, in order to determine the neuron's capacity to stimulus intensity and assess the feasible range of the current and conductance injection within which neurons

were able to generate action potentials.

### Data analysis

The occurrence of spikes was defined by a positive crossing of a threshold potential, usually  $-40$  mV. Spike rate is calculated by the number of occurrence of spikes over the total time period (1.8 s). Of 23 cortical neurons recorded in the experiment, 11 regular-spiking (RS) cells were selected for detailed analysis, whose average membrane time constant was  $22.7 \pm 8.5$  ms. For each selected RS cell, tens to hundreds of good recordings were chosen for the study of neuronal tuning to the stimulus frequencies.

## 3.2.2 Mathematical modelling

### Single neuron model

I choose the integrate-and-fire model for simulation because it is simple and analytical traceable. Action potentials are generated by a threshold process. Let  $v(t)$  be the membrane potential of the neuron,  $V_\theta$  the threshold, and  $V_{rest}$  the resting potential. Suppose  $V_\theta > V_{rest}$ , and when  $v(t) < V_\theta$ , the leaky integrate-and-fire model has the form

$$\begin{cases} dv(t) &= -\frac{v(t)-V_{rest}}{\gamma} dt + dI_{syn}(t) \\ v(0) &= V_{rest} \end{cases}, \quad (3.2.1)$$

where  $\gamma$  is the decay time constant,  $I_{syn}(t)$  is the synaptic input defined by  $dI_{syn}(t) = \mu(t)dt + \sigma(t)dB_t$ ,  $\mu(t) \geq 0$ ,  $\sigma(t) \geq 0$ , and  $B_t$  is the standard Brownian motion. The synaptic current is composed of two terms: the deterministic driving force  $\gamma\mu$ , that depolarize the cell to fire, and the noise term  $\gamma\sigma$ , that introduces perturbation of the system. I assume that a model neuron receives synaptic inputs from  $N_s$  active synapses, each sending Poisson EPSPs (excitatory post-synaptic potentials) inputs to the neuron with rate  $\lambda_E(t) = \frac{a}{2}(1 + \cos(2\pi Ft))$ , where  $a$  (magnitude),  $F$  (temporal frequency) are both constant, and  $t$  is the time (Feng and Brown, 2004). More specifically,  $\lambda(t) = \lambda_E(t)N_s$  as the input rate, and the Poisson process inputs are defined by  $\mu(t) = \lambda(t), \sigma^2(t) = \lambda(t)$ . A refractory period  $t_{ref}$  from 1 to 5 ms is also introduced in the model, matching the observation of membrane potentials in the experiment. The input temporal frequency  $F$  is confined within the range from 1 to 50 Hz, consistent with the feasible biological frequency (Salinas et al., 2000; Romo et al., 2003). In this work I concentrate on the mean output firing rate with respect to different input information frequencies.

### Analytical solution of integrate-and-fire model

Suppose that initially  $t = 0$ , the neuron has just fired and the membrane potential is reset to  $v(0) = V_{rest}$ . Before a spike has occurred, it is easy to get the analytical solution for this integrate-and-fire model (Eq. 3.2.1) with the sinusoidal synaptic current driving force  $I_{app}(t) = C(1 + \cos(2\pi Ft))$  when

no noise term is presented, and  $C = aN_s/2$ . The solution is

$$v(t) = V_{rest} + \int_0^t \exp\left(-\frac{s}{\gamma}\right) I_{app}(t-s) ds. \quad (3.2.2)$$

This expression (Eq. 3.2.2) describes the membrane potential for  $0 < t < t^*$  and is valid up to the moment of the next threshold crossing, where  $v(t^*) = V_\theta$ . After a spike is generated, the membrane potential is reset to  $V_{rest}$  and the integration restarts. Using integration by parts, Eq. 3.2.2 can be solved explicitly as

$$v(t) = V_{rest} - C\gamma \left( \exp\left(-\frac{t}{\gamma}\right) - 1 \right) + C \left( \frac{2\pi F\gamma^2 \sin(2\pi Ft) - \gamma \exp\left(-\frac{t}{\gamma} + \gamma \cos(2\pi Ft)\right)}{(2\pi F)^2\gamma^2 + 1} \right). \quad (3.2.3)$$

If time  $t$  is infinitely long and no threshold is applied in the system, the limit membrane potential  $v(t)$  would lie in the range between

$$\left[ V_{rest} + C\gamma - \frac{C\gamma}{\sqrt{((2\pi F)^2\gamma^2 + 1)}}, V_{rest} + C\gamma + \frac{C\gamma}{\sqrt{((2\pi F)^2\gamma^2 + 1)}} \right].$$

If the threshold is greater than the maximal value of  $v(t)$ , i.e.,

$$V_\theta > V_{rest} + C\gamma + \frac{C\gamma}{\sqrt{((2\pi F)^2\gamma^2 + 1)}},$$

the output firing rate would be zero and the corresponding critical value of the input frequency  $F^*$  can be calculated explicitly by setting  $V_\theta = V_{rest} + C\gamma +$

$\frac{C\gamma}{\sqrt{((2\pi F)^2\gamma^2+1)}}$ . Therefore,

$$F^* = \frac{\sqrt{\left(\frac{C\gamma}{V_\theta - C\gamma}\right)^2 - 1}}{2\pi\gamma}. \quad (3.2.4)$$

When  $F < F^*$ , periodic spiking is guaranteed to be generated.

### Equivalent ordinary differential equation system and its limit cycle

To explore the dynamic behavior of the system and to show the properties of the model with sinusoidal input signal, the integrate-and-fire model (Eq. 3.2.1) can be converted into an autonomous dynamic system, by introducing two more variables  $x$  and  $y$  from the periodicity of the input frequencies. Let

$$\begin{cases} x = C \cos(2\pi Ft) \\ y = C \sin(2\pi Ft) \end{cases}$$

Excluding the noise term, the ODE system equivalently becomes:

$$\begin{cases} \frac{dv}{dt} = -\frac{v(t) - V_{rest}}{\gamma} + C + x \\ \frac{dx}{dt} = -2\pi Fy \\ \frac{dy}{dt} = 2\pi Fx \end{cases} \quad (3.2.5)$$

Because of the periodicity in  $x$  and  $y$ , a solution can be regarded as a curve winding on a cylinder:  $x^2 + y^2 = C^2$ . The limit cycle (a trajectory in phase space having the property that at least one other trajectory spirals into it as

time approaches infinity) of this ODE system is not explicit. However, the maximal and minimal values of the limit cycle can be solved analytically by assuming that no threshold is applied to the neuron firing model, and the time tends to infinity, where the solution (Eq. 3.2.3) will tend to be the limit cycle. In this case, the exponential terms in Eq. 3.2.3 tend to zero, and the remaining sinusoid terms remain oscillating:

$$v(t) = C\gamma + \frac{C(2\pi F\gamma^2 \sin(2\pi Ft) + \gamma \cos(2\pi Ft))}{(2\pi F)^2\gamma^2 + 1}.$$

According to the properties of the sinusoid formula, I can set

$$\sin \phi = \frac{2\pi F\gamma^2}{\sqrt{(2\pi F\gamma^2)^2 + \gamma^2}}, \quad \text{and} \quad \cos \phi = \frac{\gamma}{\sqrt{(2\pi F\gamma^2)^2 + \gamma^2}}.$$

so that

$$\begin{aligned} \lim_{t \rightarrow \infty} v(t) &= \lim_{t \rightarrow \infty} C\gamma + \frac{C(2\pi F\gamma^2 \sin(2\pi Ft) + \gamma \cos(2\pi Ft))}{(2\pi F)^2\gamma^2 + 1} \\ &= \lim_{t \rightarrow \infty} C\gamma + \frac{C\gamma \cos(2\pi Ft - \phi)}{\sqrt{(2\pi F)^2\gamma^2 + 1}}. \end{aligned}$$

Since  $\cos(2\pi Ft - \phi) \in [-1, 1]$ , the two optimal points on the limit cycle  $t \rightarrow \infty$  can be found as

$$C\gamma \pm \frac{C\gamma}{\sqrt{(2\pi F)^2\gamma^2 + 1}}. \quad (3.2.6)$$

From the above equation, it is not hard to see that the difference between the maximal and minimal values of limit cycle becomes smaller and smaller if  $F$

becomes bigger and bigger. In other words, the degree of tilt of the limit cycle decreases as  $F$  increases (Fig. 3.5).

### Recurrent excitatory network neurons

In a neural network of size  $N$ , we assume that neuron  $i$  is connected to neuron  $j$  by a connection weight  $w_{i,j}$  (drawn randomly from a standard normal distribution),  $i, j = 1, \dots, N$ , and  $w_{i,i} = 0$  (see Fig. 3.6A for an illustration of the network structure). Assume that the  $i$ th neuron generates a spike at time  $t_{i,p}$ ,  $1 \leq p \leq k_i$ , where  $k_i$  is the number of spikes that the  $i$ th neuron generated within a certain time. The  $i$ th neuron receives the sensory synaptic current input  $I_{i,syn}(t)$  and local synaptic input from the other  $N - 1$  neurons. The behavior of the membrane potential  $v_i(t)$  of the  $i$ th neuron at time  $t$  is then given by

$$dv_i(t) = -\frac{v_i(t) - V_{rest}}{\gamma} dt + dI_{i,syn}(t) + dt \sum_{j=1, j \neq i}^N \sum_{t_{i,p} < t_{j,q} < t} w_{j,i} \delta(t - t_{j,q}).$$

When neuron  $i$  fires, it induces synaptic current in its connected neurons in the network, and their membrane potential will either increase or decrease in proportion to the synaptic connection weight, depending on the type of the synaptic input (EPSP, IPSP).

**Higher hierarchy neuron (comparison neuron)**

Because in the nervous system, neural signals are transmitted from lower levels to higher levels, it is possible that higher hierarchy neurons exist whose function is to integrate the outputs of all neurons with opposite spiking patterns to enhance the gain of encoding. We refer to this higher order neuron as a comparison neuron. The comparison neuron has the same parameter values as other neurons, except that it takes the output spike trains of the neural network as inputs (Fig. 3.7B). The membrane potential behavior of the comparison neuron at time  $t$  is

$$dv_c(t) = -\frac{v_c(t) - V_{c,rest}}{\gamma_c} dt + dt \left( \sum_{j=1, j \neq i}^n \sum_{t_{ip} < t_{jq} < t} w_{inc,j,i} \delta(t - t_{jq}) - \sum_{l=1, l \neq k}^m \sum_{t_{kr} < t_{ls} < t} w_{dec,l,k} \delta(t - t_{ls}) \right).$$

When neurons from the pool (of size  $m$ ) of decreasing-rate neurons fires, it generates IPSPs in the comparison neuron, while the increasing-rate pool (of size  $n$ ) excites the membrane potential of the comparison neuron, in proportion to their connection weights.

## 3.3 Results

### 3.3.1 Experiment

We carried out experiments to record from neurons in acutely-isolated slices of somatosensory cortex of the rat. Although in these conditions, the normal peripheral afferent pathways are of course removed, the intrinsic spike-generating properties of neurons are believed to be largely intact, and can be investigated under controlled conditions. Regular-spiking neurons were selected by their pyramidal appearance and their membrane potential responses to constant step current stimuli (Fig. 3.1A). 113 sets of stable recordings suitable for analysis in different conditions of stimulus amplitude, offset and frequency in 11 neurons were obtained. Of these, 21 out of 113 recordings showed an increasing firing rate as the input frequency increased from 10 Hz to 50 Hz, 28 recordings showed a decreasing firing rate with respect to the stimulus frequency, and the remaining 64 recordings showed no significant changes of firing rate as input frequency was varied. The averaged response rates of each category of firing pattern as a function of input frequency are plotted in Fig. 3.1B (mean  $\pm$  STD). We found that when the stimulus offset was relatively small in comparison to the neuronal input conductance (see Methods), some neurons were able to fire at low frequency but decreased their response rate as the stimulus frequency increased (Fig. 3.1B, blue line). In other recordings, neurons fired in proportion to the stimulus frequency, with a positive slope, when the stimulus offset was relatively high (Fig. 3.1B, green

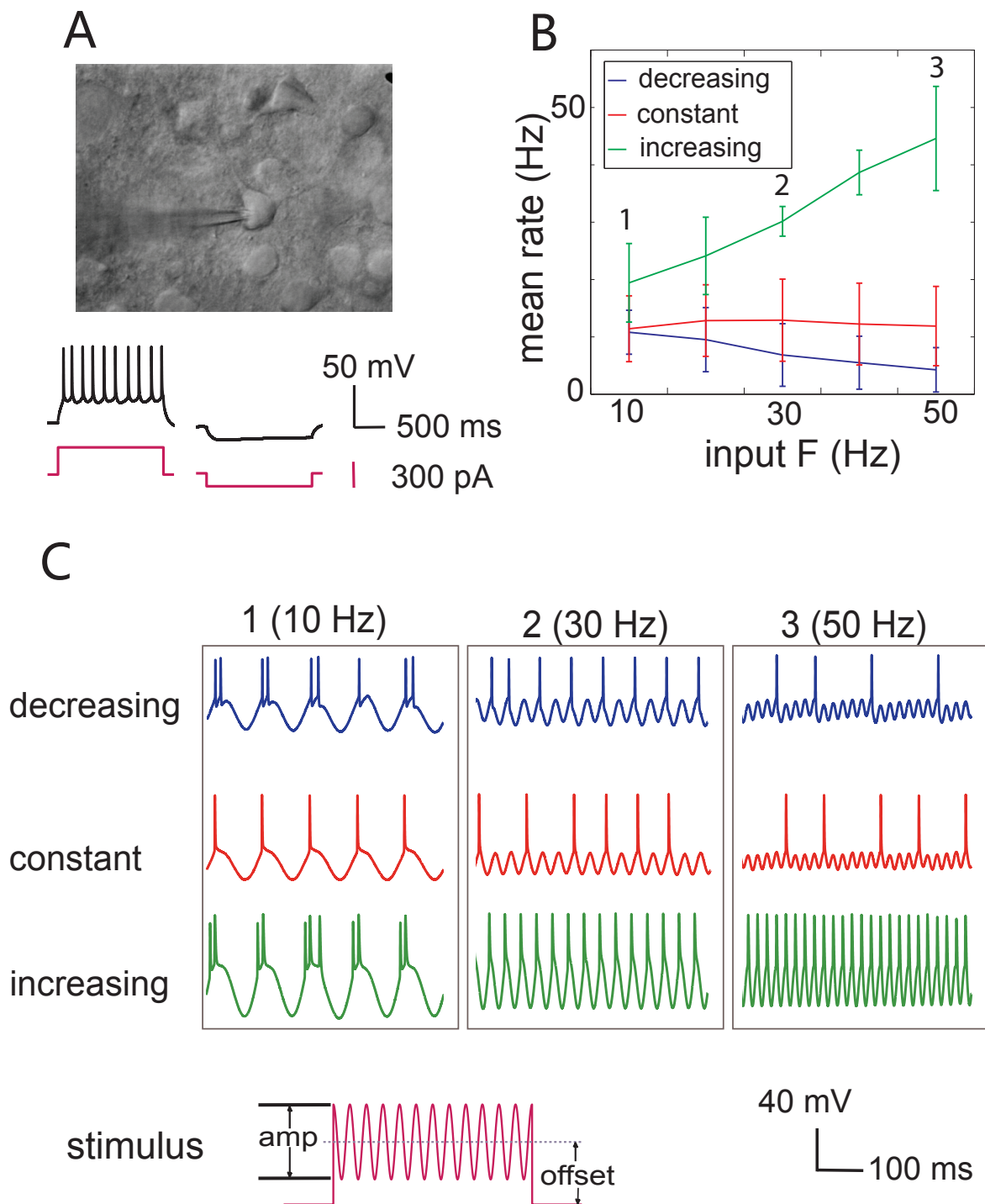


**Fig. 3.1:** Experimental result. **(A)** Infrared differential interference contrast photograph of a whole-cell patch-clamp recording from a regular-spiking pyramidal neuron: stimulation and recording are carried out through the pipette on the soma. Below: recorded membrane potential (black) filtered with a Gaussian digital filter when injected constant current (pink) is 300 pA (left) and -100pA (right). **(B)** Average tuning curves of neurons when the offset values of the injected stimuli varies. The output spiking rate is a decreasing function of the input frequency (blue) when stimuli were of relatively small offset magnitude, and the neuron's firing rate was steady (red) or even increasing (green) for stimuli with larger offset. **(C)** Membrane potential with sinusoidal current injection (pink) of different frequencies of 10, 30 and 50 Hz, respectively (blue: decreasing, red: flat, and green: increasing).

line). A pattern in which firing rate remained constant as for stimulus frequency varied was commonly observed as well (Fig. 3.1B, red line). Fig. 3.1C shows examples of the recorded membrane voltage in different types of response patterns at 10 Hz, 30 Hz and 50 Hz stimulus frequencies. In some cases, individual neurons could shift from a decreasing pattern of response (with increasing stimulus frequency) at low stimulus offset amplitude, to an increasing pattern, at higher offset amplitude. This undoubtedly reflects the relationship between the threshold, the timescale of subthreshold leaky integration, and stimulus offset amplitude, which is clearly an important feature for determining the type of response. Such a shift in response pattern may not be physiologically significant, if the sensory synaptic input is in a restricted range of amplitudes.

### 3.3.2 Single neuron simulation

We used an integrate-and-fire model for the simulation, studying the neuronal responses to the deterministic and stochastic (Poisson noise) oscillatory current stimuli. Every simulation was run 1000 times for the stochastic Poisson inputs. The simulation time for each neuron was 1000 ms. The modelling parameter values are  $V_\theta = 20$  mV,  $V_{rest} = 0$  mV, and  $N_s = 100$ , unless otherwise specified. We choose parameter values in agreement with our experimental data from the single cell recordings and with data from the literature (Keener, Hoppensteadt et al. 1981; Feng and Brown 2004).

### Constant efferent firing rate

The LIF model had a constant firing rate when the parameters satisfied  $C\gamma > V_\theta$ , where  $C = aN_s/2$ . With the parameters  $\gamma = 20$  ms,  $a = 20.5$  Hz, and the refractory period  $t_{ref} = 5$  ms, the firing rate was essentially invariant with respect to the input frequency, no matter if noise is applied in the model (Fig. 3.2A, purple) or not (Fig. 3.2A, black), consistent with the biological data (Fig. 3.1B, red line). Although the tuning curve for spike rate showed a local peak at around 20 Hz (compare to fluctuations in the flat experimental response pattern, Fig. 3.1B), this is smoothed when Poisson noise is added. Membrane potential responses are plotted in Fig. 3.2B for three different input frequency values  $F = 10$  (top), 30 (middle), and 50 (bottom) Hz, and for both deterministic and noisy input. A constant efferent firing rate means that no information about the temporal input frequency  $F$  is contained in the output firing rate. Hence, by reading the efferent firing rate alone, it is impossible to perform discrimination tasks between various input frequencies, for this kind of response pattern.

One hypothesis to explain this phenomenon is that the model averages out the information in time domain. This was proposed by Feng and Brown (2004) to explain why the integrate-and-fire model neuron is insensitive to the input temporal frequency in the. They examined low input rates varying from 1 to 10 Hz, and found that the output firing rate remained a constant. When

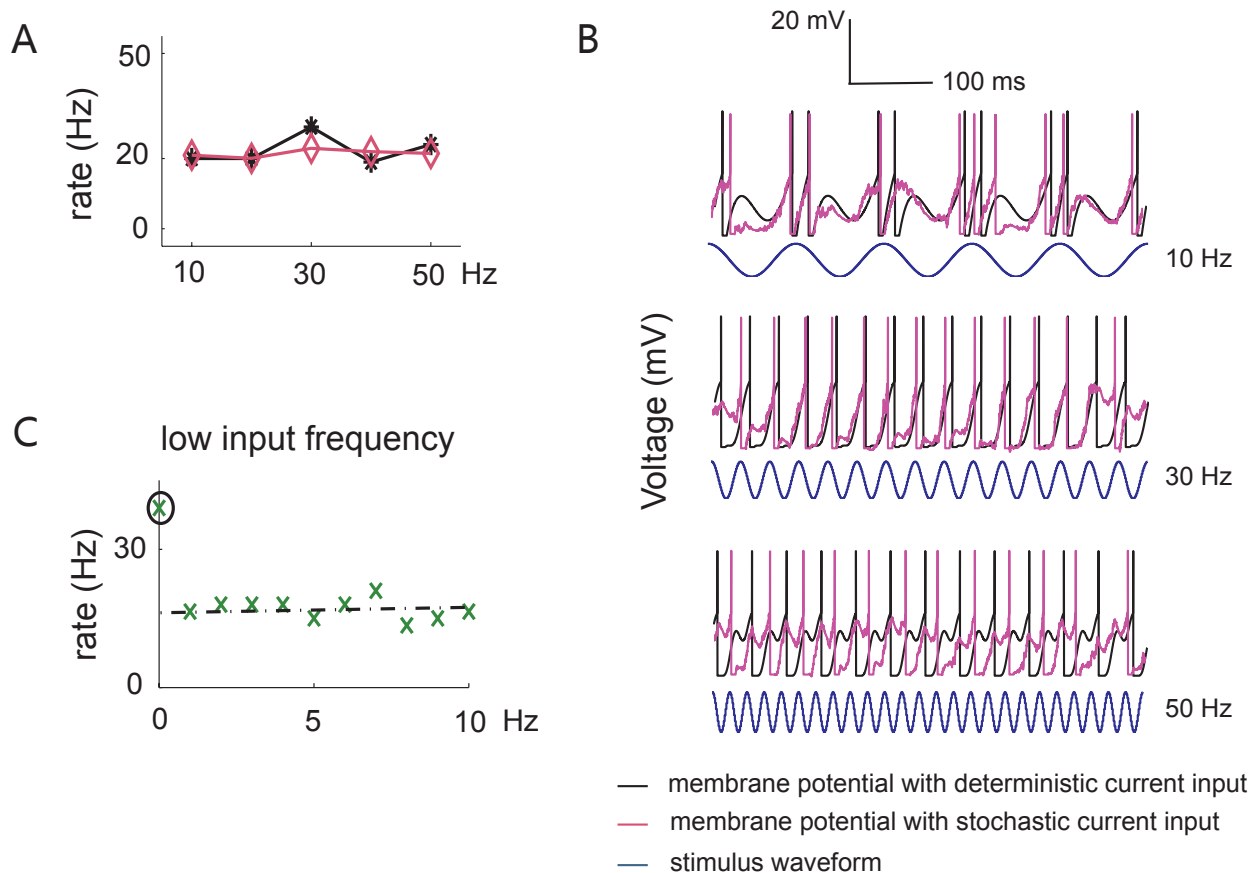


**Fig. 3.2:** Simulation results for single neurons with flat output firing rates. **(A)** Tuning curve of a simulated neuron with parameter values:  $a = 20.5$ ,  $\gamma = 20$  ms, and  $t_{\text{ref}} = 5$  ms, with (pink) or without (black) noise. **(B)** Membrane potential responses of the integrate-and-fire model to different input frequencies (top:  $F = 10$  Hz; middle:  $F = 30$  Hz; bottom:  $F = 50$  Hz). **(C)** Except at  $F = 0$  Hz, the resting output firing rate remains constant when  $F$  is close to zero.

$F$  is high, the firing rate of the neuron model is given by

$$\lambda(t) = \frac{a}{2} \lim_{T \rightarrow \infty} \left[ 1 + \int_0^T \frac{\cos(2\pi Ft)}{T} dt \right] = \frac{a}{2}.$$

This finding is reproduced here in Fig. 3.2C. Another interesting phenomenon is that there is a sudden decrement in the value of efferent firing rates from  $F = 0$  to  $F > 0$  (Fig. 3.2C), which means that the integrate-and-fire model can easily detect whether there or not an oscillating signal is present, but cannot tell how fast the period of the signal is.

### Decreasing efferent firing rate

When  $C\gamma < V_\theta$ , the neuronal efferent firing rate is a decreasing function of the stimulus frequency (Fig. 3.3A). The parameter values used here are  $\gamma = 20$  ms,  $a = 16.8$  and  $t_{ref} = 1$  ms. The neuron stops firing when the input frequency reaches the critical value  $F^* = 41$  Hz (Eq. 3.2.4 for detailed calculation). Membrane potential responses and input synaptic current are shown in Fig. 3.3B at three different frequencies ( $F = 10$  (top), 30 (middle), and 50 (bottom) Hz), for deterministic and stochastic input. This clearly illustrates that firing rate decreases with increasing input frequency.

To further elucidate the cause of this decreasing relationship, we plotted neuronal response rate at three different stimulus amplitudes  $a$  (16.8, 15 and 14) for deterministic input (Fig. 3.3C, top) and stochastic input (Fig. 3.3C, bottom). Before the neuron's firing is quenched (when  $F > F^*$ ), even though

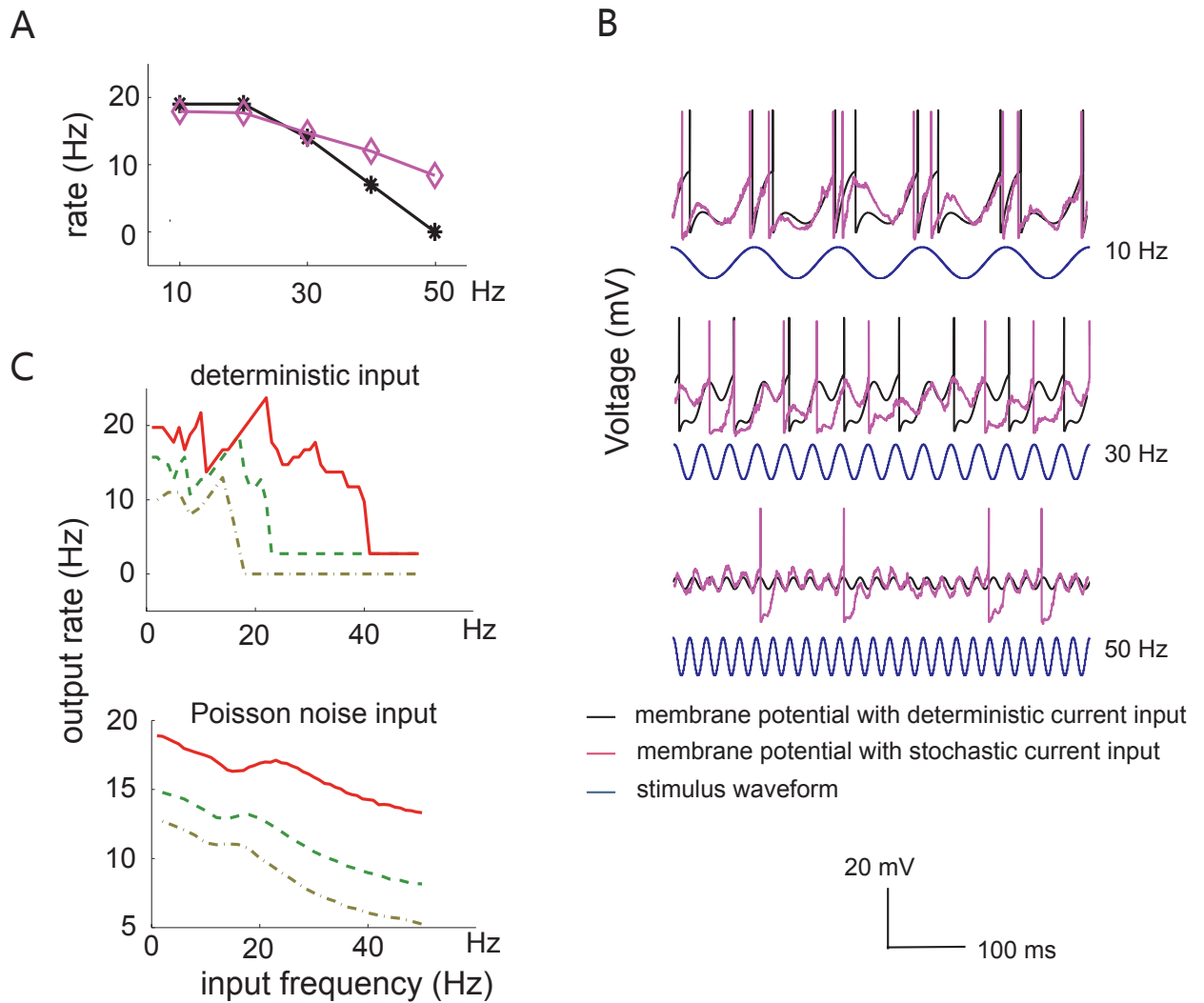


**Fig. 3.3:** Simulation results for neurons with decreasing output firing rate. **(A)** Simulated output firing rate versus the input frequency at 10, 20, 30, 40 and 50 Hz with (black) and without (pink) noise, when parameters are:  $a = 16.8$ ,  $\gamma = 20$  ms, and  $t_{\text{ref}} = 1$  ms, over the range up to 50 Hz. **(B)** Membrane potential responses of the integrate-and-fire model at different input frequencies (top:  $F = 10$  Hz; middle:  $F = 30$  Hz; bottom:  $F = 50$  Hz) when noise was absent (black) or present (purple). **(C)** Input-output relation of the output firing rate versus the input frequency from 1-50 Hz continuously with deterministic input (top panel) and Poisson noise (bottom panel). The parameters are  $a = 16.8$  (red solid line), 15 (green dash line), and 14 (brown dotted line). Here,  $\gamma = 20$  ms, and the neuronal response rates for Poisson noise were averaged over 1000 runs.

the output firing rate is increasing over some segments of the input range (due to the phase locking under this parameter region, see the following section for a detailed explanation), its overall trend is decreasing. When Poisson noise is added, the relationship is smoothed, giving an almost monotonically decreasing trend.

### Increasing efferent firing rate

To generate an increasing spiking rate with respect to the stimulus frequency, a subthreshold intrinsic oscillation  $k(\cos(2\pi\omega_0 t) + 1)$  is added to the model, where  $k$  and  $\omega_0$  are constant. The peak response rate is reached at the value where the input frequency  $F$  fully resonates with the intrinsic neuronal frequency  $\omega_0$ . Neglecting the noise term in the system, the model is fully defined by

$$\begin{cases} \frac{dv}{dt} = -\frac{v(t)-V_{rest}}{\gamma} + \frac{dI_{syn}(t)}{dt} + k(\cos(2\pi\omega_0 t) + 1) \\ v(0) = V_{rest} \end{cases}$$

When  $\gamma = 9$  ms,  $a = 10$ ,  $t_{ref} = 5$  ms and  $k = 1.5$ , the efferent firing rate is an increasing function of the temporal input frequency  $F$ . The maximal response rate is reached at  $F = \omega_0 = 50$  Hz (Fig. 3.4A, black). When the Poisson noise is presented, the tuning curve becomes smoothly monotonically linearly increasing (Fig. 3.4A, purple). Fig. 3.4B illustrates the membrane potential trajectories for different frequency values ( $F = 10, 30, 50$  Hz).

The goal of our mathematical modelling is to seek a simplest or minimal

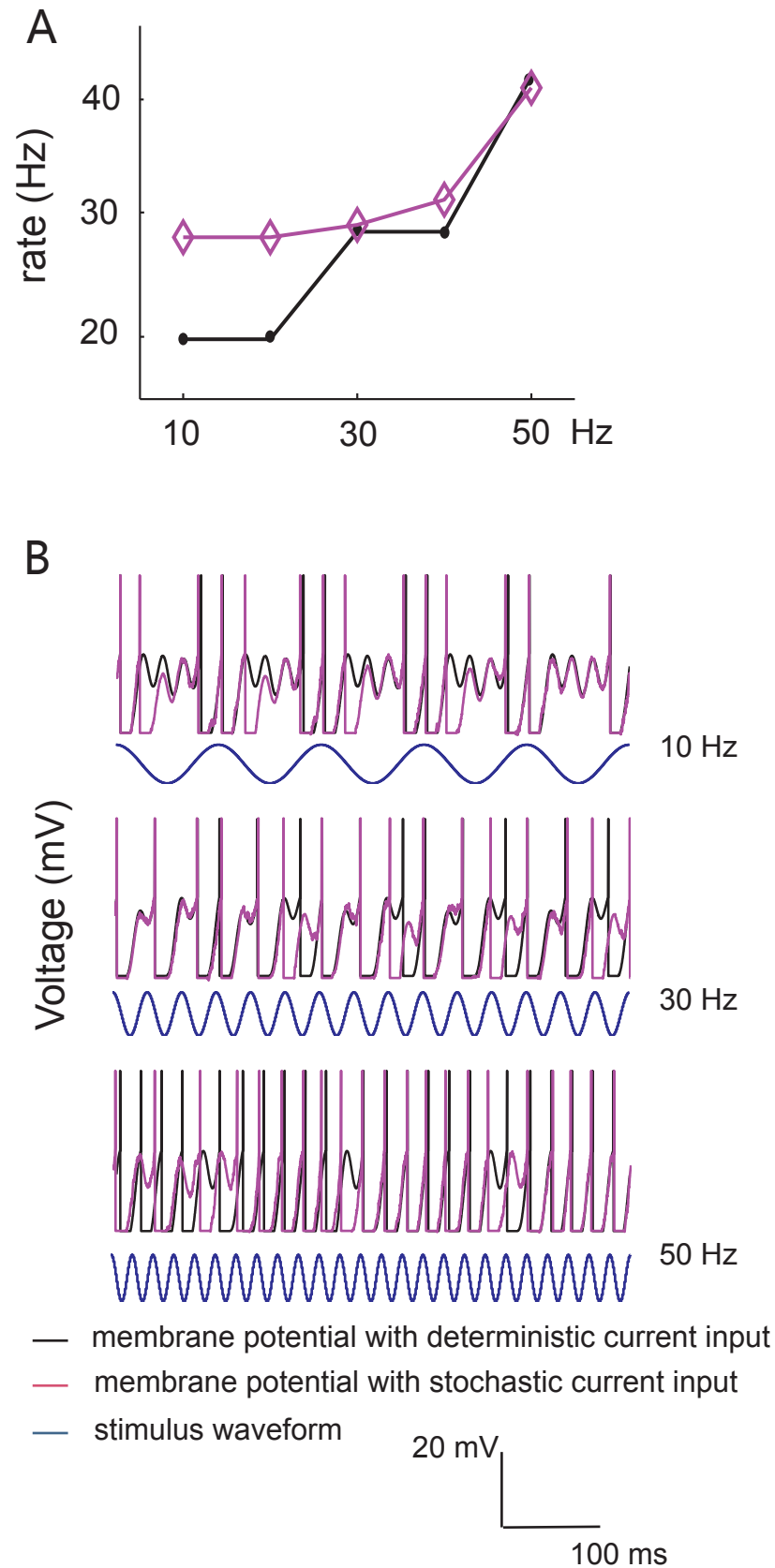


**Fig. 3.4:** Simulation of a neuron with increasing output firing rate, when an additional subthreshold intrinsic oscillation ( $\omega_0 = 0.05$ ,  $k = 1.5$ ) is included in the dynamic system. Other parameter values used for modeling are  $a = 10$ ,  $\gamma = 9$  ms, and  $\text{tref} = 10$  ms. **(A)** Response frequency rises as input frequency increases. **(B)** Membrane potential of the integrate-and-fire model with different values of input frequencies (top:  $F = 10$  Hz; middle:  $F = 30$  Hz; bottom:  $F = 50$  Hz). It is seen that the neuron is more active at high frequency, and has a monotonically increasing firing pattern.

mechanism to mimic the three response patterns shown by biological neurons, rather than giving a detailed biophysical model of spike generation. The simplest LIF model without any modification is capable of generating constant and decreasing firing patterns in terms of input frequency. However, in order to make the spiking rate an increasing function of input frequency, the minimal addition to the model is to include an intrinsic oscillation, where firing increases up to a peak value when the external frequency resonates with the intrinsic oscillatory frequency.

### 3.3.3 Mechanism of various spiking patterns

We next analyze the underlying mechanism of these three different response patterns. The reason for these distinct patterns can be understood in the relative location of the limit cycle of the neuronal dynamics, defined by the sinusoidal input and the "integrate" part of the integrate-and-fire model (in the absence of the spiking mechanism), and the threshold (Fig. 3.5). A limit cycle is obtained when there is no threshold operation applied to the membrane potential, so that the three-dimensional dynamical system of the membrane potential is attracted to its stable trajectory (Eq. 3.2.5).

#### *Mechanism for constant firing pattern*

When the limit cycle is located totally above or below the threshold, the output firing rates are all constant. In fact, when the limit cycle is below the value of the threshold, the neuron's firing rate would be zero. This is because when the membrane potential reaches the limit cycle, it will stay there forever,

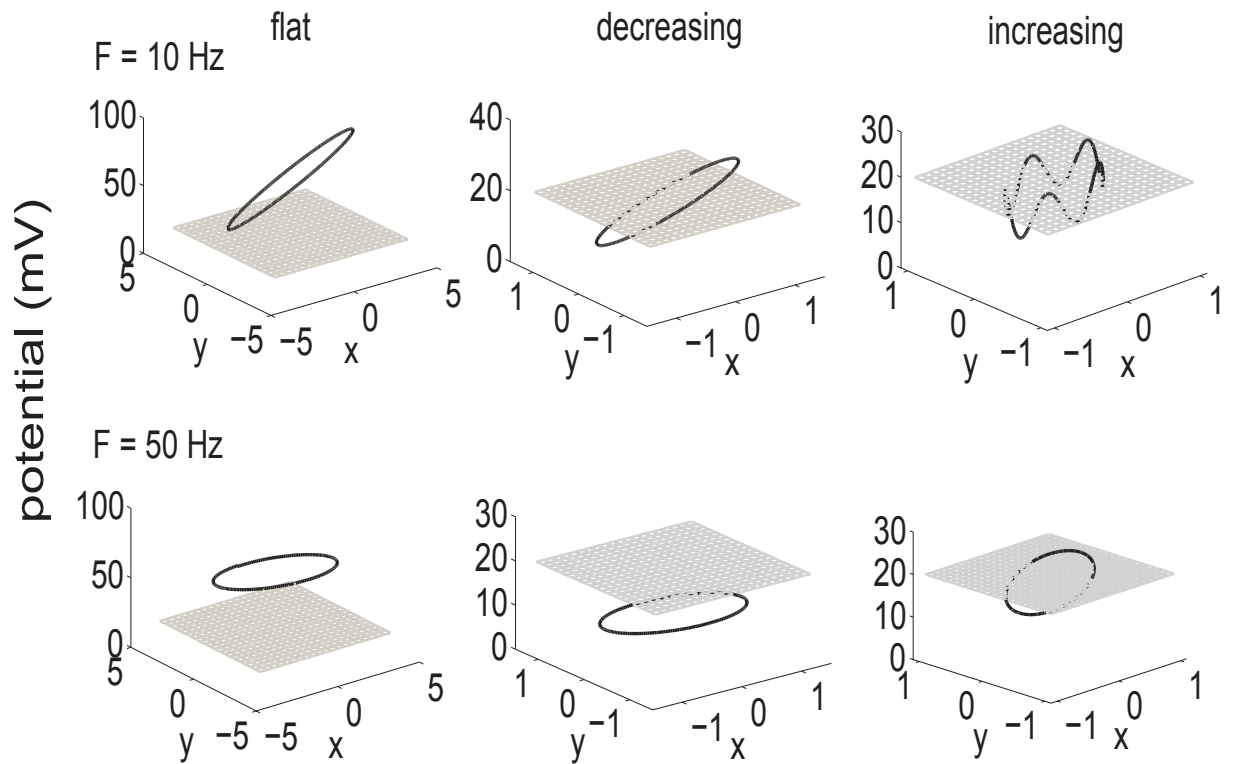


**Fig. 3.5:** Limit cycle plots for the flat, decreasing and increasing firing patterns, when no threshold is applied in the neuron model. A detailed explanation of this autonomous dynamic system can be found in the Method section, where x axis represents  $x = C \cos(2\pi Ft)$ , and y axis is  $y = C \sin(2\pi Ft)$ . The degree of tilt when  $F = 10$  Hz is much larger than when  $F = 50$  Hz. Threshold value is represented by the grey grid square.

never crossing threshold. If the limit cycle lies above the threshold, the output firing rate is roughly constant. This is the case for flat efferent firing rate ( $\gamma = 20.5$  ms). The limit circle is located above the threshold (Fig. 3.5 left column), and consequently, the membrane potential  $v(t)$  reaches the threshold before it reaches the limit circle and is then reset to the initial value. Thus, the input frequency  $F$  cannot influence the system's firing rate much. As a result, whenever the limit cycle is located completely below or above the threshold, the output firing rate is constant (zero for subthreshold case) and does not contain any information about the input frequency. An additional point is that the limit cycle is more tilted for small values of  $F$  ( $= 10$  Hz) than for big values (50 Hz) (see Fig. 3.5 left column for detailed analysis).

#### *Mechanism for decreasing firing pattern*

When the limit circle intersects with the threshold (Fig. 3.5, middle column), the output spiking rate decreases until the input frequency  $F$  increases to the critical frequency  $F^*$ , when the firing rate becomes zero. This pattern occurs because the limit cycle becomes flatter as  $F$  goes up, causing slower spiking, but eventually comes to lie completely below the threshold, whereupon the neuron stops firing.

An alternative explanation for the constant and decreasing output firing rate versus input frequency comes from the view of phase mapping, the mapping from phase of forcing at one firing time to the next (Keener et al., 1981). Keener et al (1981) classified the LIF neuron responses to oscillatory input into three parameter regions for different dynamical properties:

1. Phase locking for a subset  $T$  of parameter values, and ergodic behavior on its complement, where  $\text{meas}(T^C) \neq 0$ .
2. Phase locking for almost all parameter values and aperiodic behavior otherwise ( $\text{meas}(T^C) = 0$ )
3. Quenching, where firing eventually stops.

Here,  $\text{meas}(\cdot)$  refers to the measure of a set, and  $T^C$  denote the complementary of set  $T$ . The parameter values used in our model fall into region 2 (piecewise phase locking) and region 3 (firing termination) in Keener's paper. When Poisson noise is presented, the fluctuation of piece-wise phase locking pattern in neuronal firing rate is smoothed out and the response curves have a consistently flat or decreasing trend versus the input frequency.

The dimensionless version of integrate-and-fire model proposed in their paper is

$$\frac{du}{d\tau} = -\sigma u + S(1 + B \cos \tau),$$

and  $u(\tau^+) = 0$  if  $u(\tau) = 1$ . The parameters used in their model correspond to our model in this way

$$\begin{cases} \sigma &= \frac{1}{2\pi F\gamma} \\ F &= \frac{aN_s/2}{2\pi FV_\theta} \\ \tau &= 2\pi Ft \\ B &= 1 \end{cases}$$

Hence, our suprathreshold case where  $C\gamma > V_\theta$  that having a constant output firing rate corresponds exactly to the parameter region 2 ( $S > \sigma$ ) in their paper, where the circle mapping  $\tau_{N+1} = f(\tau_N)$  is a piecewise monotonic function and phase locked almost everywhere except parameter values on a set of measure zero. When  $S < \sigma$  and  $B > \left(\frac{\sigma}{S} - 1\right) \cdot \frac{\sqrt{\sigma^2+1}}{\sigma}$ , (which is the same as  $F < F^*$  in our model), where phase locking occurs for all parameters except on a set of measure zero; when  $S < \sigma$  and  $B < \left(\frac{\sigma}{S} - 1\right) \cdot \frac{\sqrt{\sigma^2+1}}{\sigma}$  (which is  $F > F^*$ ), the firing process terminates.

#### *Mechanism for increasing firing pattern*

Introducing an intrinsic oscillation in the neuron model is necessary to generate an increasing output spiking pattern as input frequency increases. The right column of Fig. 3.5 shows the limit cycle with an intrinsic oscillation term (at 50 Hz) at input frequency  $F = 10$  and  $F = 50$  Hz. The threshold value lies between the maximum and minimum values on the limit cycle.

### **3.3.4 Gain enhancement**

#### **Network neurons**

Even though the single neuron is sophisticated enough to generate different patterns of firing rate with various input frequencies, a population of neurons connected with each other in a network can perform much better than single neuron. We assume that neurons in the network are identical, receive the same input, and are connected with each other by excitatory synapses

(Yoshimura, Dantzker et al. 2005). The LIF parameters used in the network neurons are the same as for single neurons, and their connection weights are assigned randomly from a standard normal distribution. The simulation results showed that a neural network's spiking rates at different input frequencies were more distinguishable than that of a single neuron. Fig. 3.6 shows the decreasing and increasing firing rate patterns of the integrate-and-fire model network with random connection weights of various sizes ( $N = 1, 25,$  and  $40$  for decreasing responses;  $N = 1$  and  $10$  for increasing responses). It can be seen that the discrimination ability of the network is better than that of a single neuron since the difference of spike rates between two frequencies in neural network is much bigger than for a single neuron, for networks of both decreasing and increasing response patterns. Neural networks with non-identical neurons whose threshold values varies ( $V_\theta$  uniformly distributed within range  $[19.5, 20.5]$  mV) were also simulated, to test for the robustness of the network model, and no significant differences were found compared to identical-neuron networks (data not shown).

### **Comparison neuron**

What is the biological function of these different, opposed neural tunings, especially the opposite tuning in the cortex? In experiments on electric fish (Vonderemde and Bleckmann 1992; Vonderemde and Bell 1994; Goenechea and von der Emde 2004), opposite types (increasing and decreasing) of frequency responses of electroreceptor cells in the lateral line organs have also

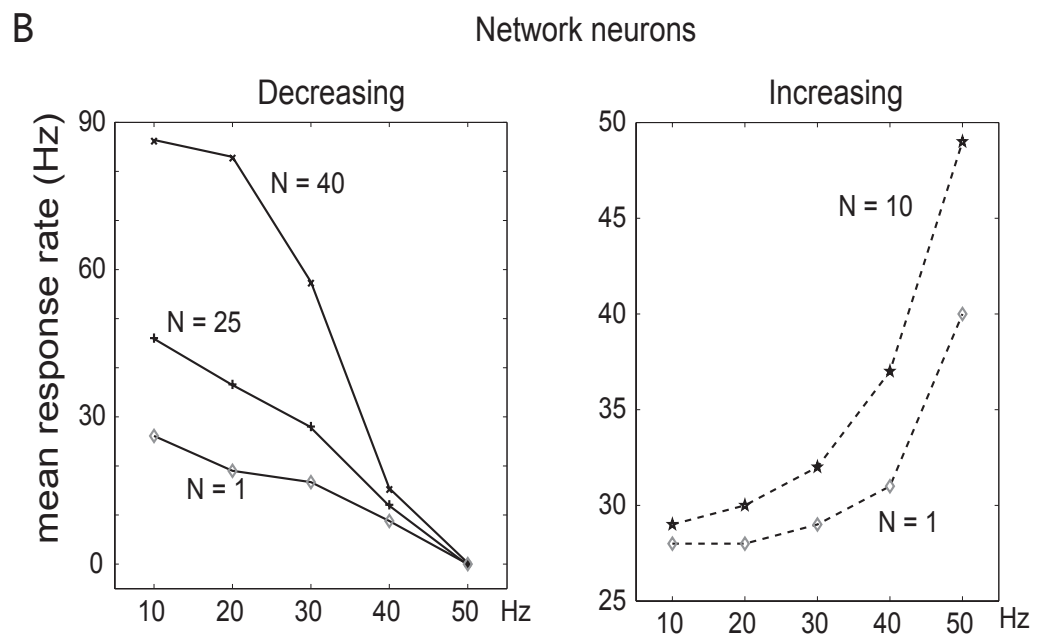
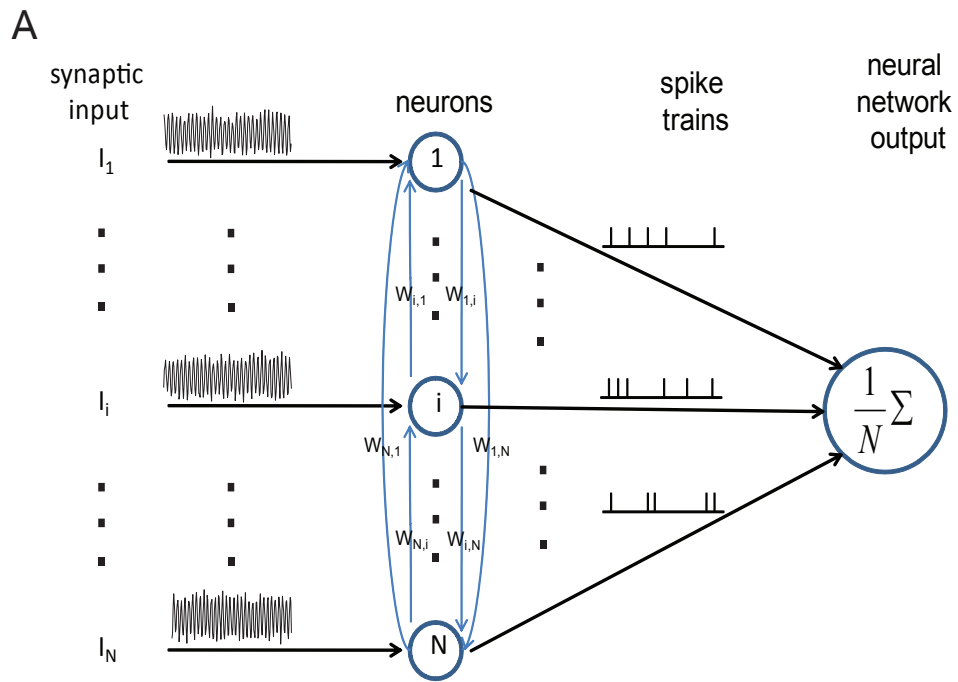


**Fig. 3.6:** (A) Illustration of the structure of the neural network. (B) The average firing rate of network neurons, for both the increasing (right) and decreasing (left) patterns. The network neurons revealed a bigger difference between the minimum and maximum firing rate than that of single neurons, both for increasing and decreasing patterns. The larger the neural network size, the more significant was the difference among neural response rate at various input frequencies. The connection weights among neurons in the network are randomly generated following a normal distribution.

been observed, and it was shown that electric fish recognize objects by centrally comparing the responses from these two different types of receptor cells.

Following this idea for the biological advantage of the heterogeneous spiking patterns in the neuronal population (Romo, Hernandez et al. 2003), we consider a comparison neuron which integrates the activity of multiple types of unit (increasing and decreasing, Fig. 3.7B), further enhancing the gain of encoding of input frequencies via the differences in spike rate amongst increasing and decreasing response types.

Fig. 3.7A shows how the gain of comparison neuron exceeds any of the previous cases (single neuron and network neurons). The gain here is defined as the ratio between the output rate differences  $\Delta F_{out}$  over the input frequency differences  $\Delta F_{in}$ . The structure of the network is illustrated in Fig. 3.7B, with the increasing rate neural network exciting the comparison neuron and the decreasing rate neural network inhibiting the comparison neuron. Fig. 3.7C shows raster plots of the comparison neuron response in each trial when the input frequency is 10 Hz (left) and 50 Hz (right).

### 3.4 Discussion

We measured experimentally the discrimination ability of single somatosensory neurons *in vitro* for temporal input frequency, in terms of their mean response rate. The LIF model was used to reproduce the results by simulation, allowing us to propose a simple underlying mechanism of the various patterns

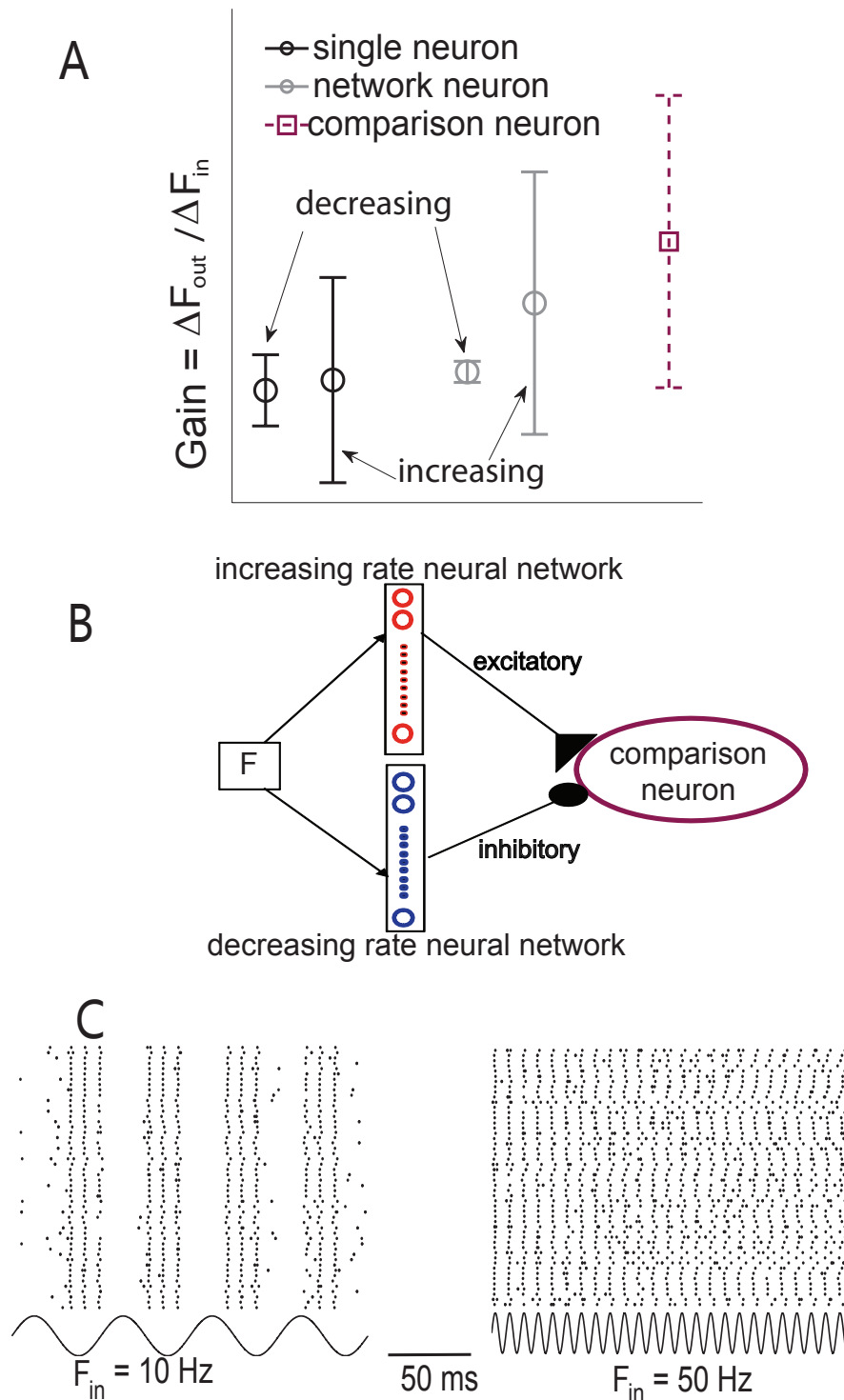


**Fig. 3.7:** Illustration of the properties and behavior of the comparison neuron in the model. **(A)** Gain control (mean  $\pm$  SD) of the comparison neuron (red dotted line), compared with single neuron (black) and network neurons (grey). **(B)** The overall neural network scheme. Stimulus input frequencies were applied to two mutually independent neural populations, with one population showing an increasing firing pattern, and the other a decreasing firing pattern. The network with increasing firing rate generates excitatory synaptic current to another individual neuron called “comparison neuron”, while decreasing neural network generates inhibitory synaptic input to the comparison neuron. The comparison neuron is also in form of an integrate-and-fire model and has a refractory period of 1 ms. **(C)** Raster plot for the comparison neuron over 100 trials with input frequency  $F = 10 \text{ Hz}$  (left) and  $F = 50 \text{ Hz}$  (right).

of neuronal responses. We illustrated a possible function for these heterogeneous spiking patterns, by considering a comparison neuron which integrates the activity of multiple types of unit (increasing and decreasing), which further increases the gain of input information. Our work sheds light on the possible cellular and network mechanisms for this heterogeneous frequency tuning of somatosensory cortical neurons.

### 3.4.1 Experimental responses

In (Salinas, Hernandez et al. 2000; Romo, Hernandez et al. 2003), it was found that some neurons in the somatosensory S2 area have a lower firing rate (around 20 Hz) for high-frequency stimuli compared to the strong responses (around 40 Hz) they show to the low-frequency stimulus, but high stimulus frequencies did not completely stop the neurons from firing. However, in the present experiments, we observed a progressive reduction in firing rate with increasing input frequency, and in many instances, quenching of firing at relative high frequency. This dissimilarity might be from the differences between *in vitro* and *in vivo* conditions, affecting the intrinsic spike-generating dynamics of neurons, but could also reflect receptor and synaptic adaptation, and locally-recruited cortical inhibition.

Nevertheless, the quenching of firing observed experimentally is consistent with the behaviour of the LIF neuronal model. Experimentally, neurons decreased their firing rate versus the input frequency only when the injected current offset was close to the minimal feasible range of stimuli, for which

generation of spikes was guaranteed. This minimal feasible range of stimuli of real neurons corresponds to the mathematical explanation of intersection (see Fig. 3.5, middle column for details) between the threshold value and the limit cycle of the dynamics. Biological neurons appeared to have a constant or increasing response versus input frequency when the oscillatory stimulus offset is in the middle range of the feasible stimuli intensity, and this is consistent with our model parameter region as well.

To compare how accurately experimental and modelled neuronal responses encode stimulus frequency, we compare them using neurometric performance curves, as shown in Fig. 3.8. A detailed description of the generation of neurometric curves can be found in (Romo, Hernandez et al. 2003). In Fig. 3.8, neurometric curves were generated by plotting the percentage of each recorded data at different comparison stimulus frequencies ( $F = 10, 20, 30, 40$  and 50 Hz) in which the comparison frequencies was called higher than the base frequency fixed at 30 Hz (because it is the middle point of the stimulus frequency range), as a function of the comparison frequency. Points near 0% or 100%, where the base frequency and comparison frequency are very different, correspond to easy discriminations, whereas points near 50% correspond to difficult discriminations. Both for the increasing and decreasing neural responses, the neurometric functions of the modeling were considerably better than the experimental data.

## Neurometric functions

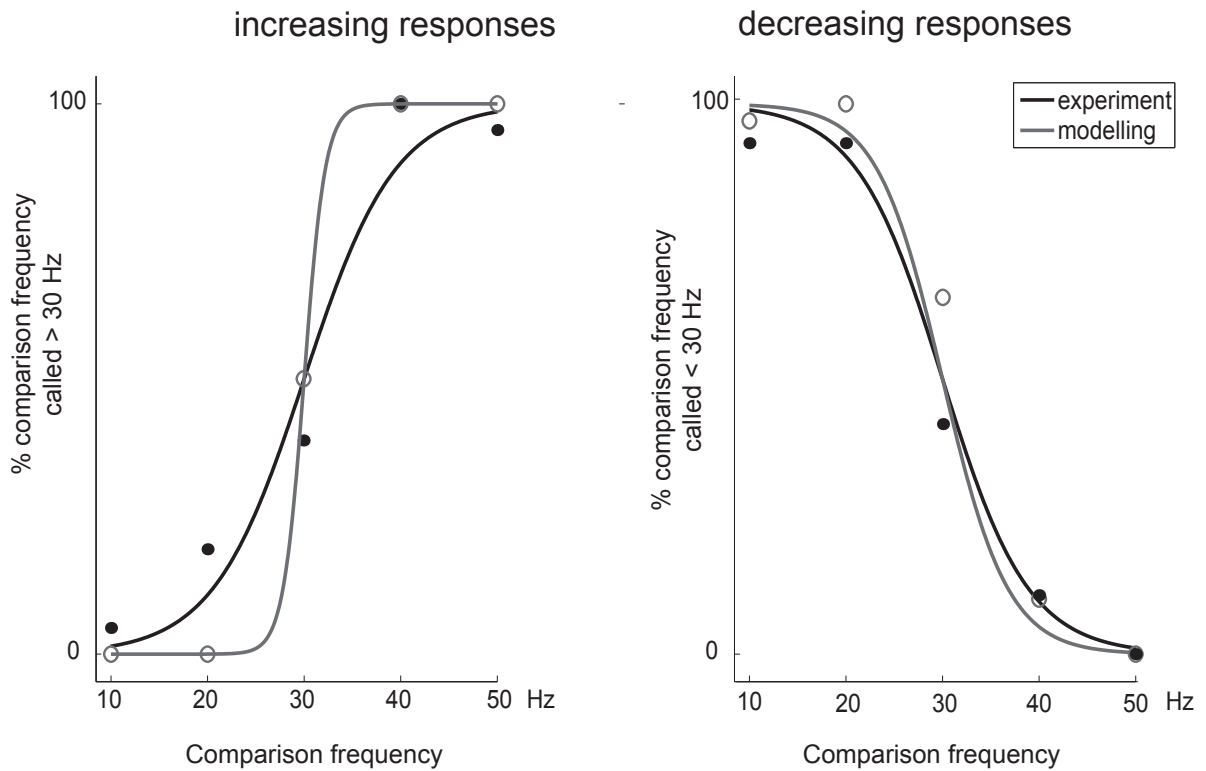


**Fig. 3.8:** Neurometric functions for the increasing and decreasing responses of the experimental recordings and the mathematical models. **Left:** For neuronal response with a positive slope. Continuous curves are sigmoidal fits ( $\chi^2$ ,  $p < 0.001$ ) to the data points for the five comparison stimulus frequencies (10, 20, 30, 40 and 50 Hz) paired with reference stimulus frequency fixed at 30 Hz. y axis is equivalent to the probability that the comparison frequencies is judged higher than the reference frequency (30 Hz). Gray line is neurometric function of experimental data; black line is of modeling data. **Right:** Same format as panel on the left, but for neuronal responses with a negative slope.

### **3.4.2 Intrinsic oscillations in increasing response patterns**

An intrinsic oscillation in the frequency range of 40 to 50 Hz of pyramidal neurons, as is predicted to be required by the model to generate increasing responses, has not been clearly described in the literature. However, it should be pointed out that what is predicted is not necessarily a detectable subthreshold oscillation of membrane potential, but an intrinsic oscillation within the suprathreshold spiking dynamics which interacts with and resonates with an "integrate-and-fire" like component of the dynamics. A strong candidate for this would be recruitment of the local fast-spiking inhibitory interneuron network, and its feedback on the recorded pyramidal neuron (Galarreta and Hestrin 1999; Gibson, Beierlein et al. 1999; Cardin, Carlen et al. 2009). Thus, it would be of interest in further studies to characterize input frequency responses in the presence of synaptic blockers of glutamate and GABA receptors to disconnect this component of the network.

### **3.4.3 Biological function**

In the nervous system, encoding and decoding is accomplished at a system level rather than at a single neuron level. Network neurons gain an advantage in generating more distinguishable efferent spike rates at different input frequency levels, by the connectivity of the neurons in the network: one neuron's action potential will contribute to other neurons' membrane potential in proportion to the connection weight. As a result, the output firing rate of the

whole neural network is boosted by positive feedback over the output rate of an individual neuron. In (Romo, Hernandez et al. 2003), it is shown that cortical networks can enhance the neural representation of features from the complementary populations with positive and negative responses slopes as a possible coding strategy. In our model, the maximal gain is about 0.3 for a single neuron and network neurons, while the comparison neuron is able to boost the gain up to around 0.7 by integrating the information from networks of opposing types of neurons (increasing and decreasing), making a discrimination task much easier to perform.

#### **3.4.4 Other possible neural models**

The leaky integrate-and-fire model is not the only model that is able to decode the input frequency from its efferent firing rate, although using LIF alone we can account for many biological phenomena, see for example (Rossoni, Feng et al. 2008). One of the other possible forms is the quadratic integrate-and-fire model (Burkitt 2006) that we have found can make the output firing rate a decreasing function of the input frequency (data not shown). The principle is similar to what we analyzed in the leaky integrate-and-fire neuron. A more biophysically-realistic neuron model is the Hodgkin-Huxley (HH) model (Brown, Feng et al. 1999). According to Feng and Brown (2001), the tuning curve has two maximum points and one minimum point, but it is not possible to uniquely read out the input temporal frequency (Feng and Brown 2004). The reason why the Hodgkin-Huxley model is able to generate an in-

creasing pattern at low input frequencies is believed to be that the HH model itself contains an intrinsic subthreshold oscillation with a defined frequency, which makes it possible to generate two peaks at 60 Hz and 120 Hz, respectively, for the standard Hodgkin-Huxley model (refer to the Appendix of Feng and Brown (2004) for detailed equations and parameters).

### **3.5 Final Remark**

In the current study, we have also tested if single neurons and network neurons can discriminate input stimulus frequencies following Weber's law<sup>1</sup>. However, by examining the number of spikes of neurons generated at a certain time alone does not give the behavior described by this psychophysical law, and we realized that it is not only the mean spike rate, but also the variability of the spike rate that matter. Hence, we propose a question to ourselves: under what condition the mean and the variance of the neuronal spike rate must follow, that the Weber's law can be satisfied on neuronal level? This leads to our study at the next chapter—link between psychophysical and neuronal responses.

---

<sup>1</sup>Weber's law is one of the mostly accepted psychophysical law, describing the relation between the just noticeable difference and the reference stimulus intensity. The detailed description of this law is presented in the next chapter

## Chapter 4

# Link between Psychophysical and Neural Responses

In the previous chapter, we discussed how the *neurons* respond to a series of *stimuli* of the same properties (e.g. frequency), while in psychophysical studies, people are studying the correlation between human *perception* and environmental *stimuli*. Therefore, it would be interesting to study the relation between the *neuronal* response and the *psychophysical* behavior in the presence of the same stimuli. In this chapter, I propose a quantitative link between neural activities and perceptual responses.

## 4.1 Introduction

It is of little doubt that there exists a relation between the exquisite psychophysical sensitivity of human and animal observers and the sensitivity of individual cortical neurons. The transformation between sensory cortical neurons signals and the perceptual responses remains unclear, despite the fact that the link between the neuronal activity and psychophysical judgment of sensory processing has been intensively studied by many researchers (Shadlen and Newsome, 1994; Sawamura et al., 2002). The idea of quantitatively relating cortical neuronal activities to sensory experiences was first proposed by Werner and Mountcastle (Werner and Mountcastle, 1963), who enunciated some fundamental principles for the analysis of neuronal discharge in a psychophysical context. Weber's law (also called Weber-Fechner law) (Fechner et al., 1966), one of the classical psychophysical laws, states that the ratio between the just noticeable differences (JNDs) in stimulus intensity ( $\Delta I$ ) and the reference stimulus intensity ( $I$ ) is a constant  $k$  (Weber's constant), i.e.,  $\Delta I/I = k$ . This phenomenon has been observed in a wide range of moderately intense stimuli experiments in sensory perception in terms of weights (Fechner et al., 1966), pure tones (Gescheider et al., 1990), light intensities (Wald, 1945), sizes (Smeets and Brenner, 2008), texture roughness (Johnson et al., 2002), numbers (Dehaene, 2003) and etc., but there still lacks of a link between this psychophysical property and neuronal activity.

Weber's law describes the relationship only between the stimulus intensity

and psychophysical behavior, so the challenge to study this law in neuronal level is how to characterize the unclear intermediate connections of stimulus-neuronal and neuronal-psychophysical responses. In most biophysical and psychophysical experiments, the relation of neural response rate and input stimulus intensity generally follows a nonlinear sigmoid function. The middle range of a sigmoid function is asymptotically a straight line reflecting the linear relation between neural firing and the stimulus intensity. Starting from the analysis on the simplest linear case of the input-output relation between the stimulus intensity and neuronal response rate, we further extend our analysis on the nonlinear input-output relation (sigmoid function). Under Weber's law, it is found that for both linear and nonlinear relations of input stimulus and output neuronal responses, the final results are similar in terms of the neuronal spiking process. For a more biological realistic setup on neuronal input-output relation, we also investigate the neuronal spike train properties in spiking network model when Weber's law holds. Therefore, we can establish the intermediate link between the psychophysical law (Weber's law) and neuronal spike train statistics.

On neuronal level, the cortical cells exhibit tremendous variability in terms of their discharges at the repeated presentations of an identical stimulus over large regions of the cerebral cortex (Shadlen and Newsome, 1998), thalamus (Kara et al., 2000) and hippocampus (Fenton and Muller, 1998). Neuronal spike trains are regarded as random process and thus can be characterized by corresponding statistics. Spike rate is one of the most commonly used statis-

tics. Another statistic is the spiking time, and it is usually expressed in terms of the dimensionless coefficient of variation of interspike interval ( $CV_{ISI}$ , the ratio of the standard deviation (STD) to the mean of the ISI distribution), a measurement of dispersion widely used by experimentalists to determine the degree of variability of neuronal discharge. The range of  $CV_{ISI}$  of cortical neurons of extracellular recording *in vivo* has been reported to be from 0.5 to 1 through a series of experiments in monkey primary visual cortex (Knierim and Vanessen, 1992), middle temporal visual cortex (Newsome et al., 1989; Shadlen and Newsome, 1998), and inferotemporal cortex (Douglas and Martin, 1991). The spike train may be more variable than a Poisson process when non-stationary stimulus is presented (Hirase et al., 1998). The idea of renewal theory (Tuckwell, 1989) is employed here to link the statistics of spike rate and spike interval. This theory enables us to express Weber's law in terms of the irregularity of the interspike interval ( $CV_{ISI}$ ).

I theoretically derived a relationship between the mean ( $\mu$ ) and the standard deviation ( $\sigma$ ) of the neuronal spike rate when Weber's law holds, and expressed the relation in terms of the dispersion of interspike intervals which require  $CV_{ISI} \in [0.5, 1]$ . Started from single neurons, I studied the independent and correlated superimposed population neuronal discharge patterns, as well as competition attractor network neurons. The competitive attractor neural network also indicates that the neuronal interspike interval should be more regular than a Poisson process in the winning pool so that Weber's law holds. This work links Weber's law with neural firing property quantitatively: We-

ber's law indicates the variability of neuronal spike train; meanwhile given a series of spike train data stimulated at different intensities, we can determine whether this psychophysical law is satisfied. This study sheds light on the relation between the psychophysical behavior and neuronal responses.

## 4.2 Methods

### 4.2.1 Single neurons activities under Weber's law

#### Single neural firing rate statistics

Applying a constant stimulus  $I$  to a single neuron repeatedly, the neuron will fire at mean rate  $\mu$  with variance  $\sigma^2$  over a certain time. If the increment of input stimulus intensity  $\Delta I$  is just noticeable, the mean output firing rates  $\mu$  and  $\mu + \Delta\mu$  should be statistically discriminable under some criterion  $\varepsilon$ . We firstly assume the linear relation between the input stimulus intensity  $I$  and the mean output firing rate  $\mu$  (spikes/sec), as linearity of input-output relation between stimulus intensity and neuronal response rate is widely accepted and intensively used in simulation modeling (Holt and Koch, 1997), and also supported by experiments (Leng et al., 2001; Enoki et al., 2002; Johnson et al., 2002). Therefore,

$$\mu = aI,$$

where  $a$  is the scale, and

$$\frac{\Delta\mu}{\mu} = \frac{a\Delta I}{aI} = \frac{\Delta I}{I} = k \quad (4.2.1)$$

where  $k$  is the Weber's constant.

### **Discriminant $x_0$**

#### *Discriminant $x_0$ for two Normal distributions*

Assume we have two neural firing rate distributions with different means and variances  $(\mu_1, \sigma_1^2)$  and  $(\mu_2, \sigma_2^2)$ , respectively. Without loss of generality, assume that  $\mu_1 < \mu_2$ , and that  $\mu_1$  and  $\sigma_1$  follows the same relation as  $\mu_2$  and  $\sigma_2$ . First of all, we consider the case when the output firing rate of a neuron follows Gaussian distribution at given constant input stimulus intensity. For two Gaussian distributions  $N(\mu_1, \sigma_1^2)$  and  $N(\mu_2, \sigma_2^2)$ , let  $x_0$  be the linear discriminant which minimizes the weighted classification error  $\gamma P_{1,2} + P_{2,1}$ , where  $P_{i,j}$  is the probability that a point from distribution  $i$  is classified by  $x_0$  as being from class  $j$ , and  $\gamma$  is the weight. Here, only two classes will be considered, so  $i, j = 1, 2$ .

Hence, the weighted classification error for Normal distribution will be given by

$$\frac{1}{2}\gamma \operatorname{erfc}\left(\frac{x_0 - \mu_1}{\sqrt{2}\sigma_2}\right) + \frac{1}{2}\operatorname{erfc}\left(\frac{\mu_2 - x_0}{\sqrt{2}\sigma_1}\right), \quad (4.2.2)$$

where  $\text{erfc}(\cdot)$  is the complementary error function

$$\text{erfc}(x) = \frac{2}{\sqrt{\pi}} \int_x^{\infty} \exp(-t^2) dt.$$

The linear discriminant  $x_0$  which minimize Eq. (4.2.2) will occur when its derivative with respect to  $x_0$  become zero, which yields

$$\gamma \frac{1}{\sqrt{2\pi\sigma_1^2}} \exp\left(\frac{-(x_0 - \mu_1)^2}{2\sigma_1^2}\right) - \frac{1}{\sqrt{2\pi\sigma_2^2}} \exp\left(\frac{-(x_0 - \mu_2)^2}{2\sigma_2^2}\right) = 0,$$

after rearranging, this gives

$$\frac{(x_0 - \mu_1)^2}{\sigma_1^2} - \frac{(x_0 - \mu_2)^2}{\sigma_2^2} = \ln\left(\gamma^2 \frac{\sigma_2^2}{\sigma_1^2}\right).$$

Choosing  $\gamma = \sigma_1/\sigma_2$  simply implies one of the possible discriminant

$$x_0 = \frac{\sigma_2}{\sigma_1 + \sigma_2} \mu_1 + \frac{\sigma_1}{\sigma_1 + \sigma_2} \mu_2,$$

and this is the discriminant  $x_0$  we use in this section.

#### *Discriminant $x_0$ for any distributions*

Furthermore, this discriminant  $x_0$  can be used in *any* distribution to obtain the minimal misclassification rate, even if only the mean and variance are known for that particular distribution. The detailed explanation is presented as follows by showing this discriminant  $x_0$  being able to minimize the worst possible error.

Cooke and Peake (Cooke and Peake, 2002) showed the probability density function of distribution having mean  $\mu$  and variance  $\sigma^2$  that *maximize* the classification error of the discriminator  $x_0$  is of the form

$$f(x) = \frac{\sigma^2}{\sigma^2 + (x_0 - \mu)^2} \delta(x - c^+) + \frac{(x_0 - \mu)^2}{\sigma^2 + (x_0 - \mu)^2} \delta\left(x - \mu + \frac{\sigma^2}{x_0 - \mu}\right),$$

where  $\delta$  is the Dirac delta function, while  $c^+$  is defined to be a number infinitesimally larger than  $x_0$ . As a result, the worst possible weighted classification error  $\gamma P_{1,2} + P_{2,1}$  will be

$$\gamma \frac{(x_0 - \mu_1)^2}{\sigma_1^2 + (x_0 - \mu_1)^2} + \frac{(x_0 - \mu_2)^2}{\sigma_2^2 + (x_0 - \mu_2)^2}.$$

Minimizing this by setting the derivative with respect to  $x_0$  to zero provides

$$\gamma \frac{(x_0 - \mu_1)\sigma_1^2}{(\sigma_1^2 + (x_0 - \mu_1)^2)^2} + \frac{(x_0 - \mu_2)\sigma_2^2}{(\sigma_2^2 + (x_0 - \mu_2)^2)^2} = 0. \quad (4.2.3)$$

One can easily check that

$$x_0 = \frac{\sigma_2}{\sigma_1 + \sigma_2} \mu_1 + \frac{\sigma_1}{\sigma_1 + \sigma_2} \mu_2$$

is a solution of Eq. (4.2.3) when the weight  $\gamma = \sigma_1/\sigma_2$ .

Therefore,  $x_0$  can be the discriminator that minimizes the misclassification rate  $\varepsilon$  for any two distributions with known  $(\mu_1, \sigma_1^2)$  and  $(\mu_2, \sigma_2^2)$ .

**Misclassification rate**

To begin with a simple situation, we assume that the neuronal spiking rate of single neuron follows Normal distribution with parameters  $\mu$  and  $\sigma^2$ . Thus the misclassification rate is

$$\varepsilon = \frac{1}{2} \left( 1 + \operatorname{erf} \left( \frac{x_0 - \mu_2}{\sqrt{2}\sigma_2} \right) \right) + \frac{1}{2} \left( 1 - \operatorname{erf} \left( \frac{x_0 - \mu_1}{\sqrt{2}\sigma_1} \right) \right)$$

for two Normal distributions  $N(\mu_1, \sigma_1^2)$  and  $N(\mu_2, \sigma_2^2)$ . Then we have

$$\operatorname{erf}(x_2) - \operatorname{erf}(x_1) = 2(\varepsilon - 1),$$

where

$$x_1 = \frac{x_0 - \mu_1}{\sqrt{2}\sigma_1} \text{ and } x_2 = \frac{x_0 - \mu_2}{\sqrt{2}\sigma_2}.$$

By substituting  $x_0$  into  $x_1$  and  $x_2$ , we have  $x_1 = -x_2$ , and since the error function is odd function, we have

$$\operatorname{erf}(x_2) = \varepsilon - 1.$$

**Derivation of error function approximation**

The error function is defined as

$$\operatorname{erf}(x) = \frac{2}{\sqrt{\pi}} \int_0^x \exp(-x^2) dx.$$

We rewrite the integral  $\int_0^x \exp(-x^2)dx$  as

$$\sqrt{\left(\int_0^x \exp(-x^2)dx\right) \left(\int_0^y \exp(-y^2)dy\right)},$$

and represent it as a surface integral

$$\sqrt{\int_0^x \int_0^y \exp(-(x^2 + y^2)) dydx}.$$

In polar coordinate, we have  $x^2 + y^2 = r^2$  and  $dx dy = r dr d\theta$ , and the integral above becomes

$$\sqrt{\int_0^{\pi/2} d\theta \int_0^r \exp(-r^2) r dr} = \sqrt{\frac{\pi}{4} (1 - \exp(-r^2))}. \quad (4.2.4)$$

Note that the surface integrals in  $x$ - $y$  plane and  $r$ - $\theta$  plane must be equal. Replacing  $y$  by  $x$  gives

$$A_{x,y} = A_{x,x} = x^2 = A_{r,\theta} = \frac{\pi r^2}{4},$$

and this is the approximation. Substituting  $r = \frac{2}{\sqrt{\pi}}x$  to Eq. (4.2.4) and multiply the scale  $\frac{2}{\sqrt{\pi}}$ , the error function finally becomes

$$\text{erf}(x) \approx \sqrt{1 - \exp\left(-\left(\frac{2x}{\sqrt{\pi}}\right)^2\right)}. \quad (4.2.5)$$

Note that although areas  $A_{x,y}$  and  $A_{r,\theta}$  have the same numerical values, geometrically they differ. It is known fact that the difference of integral  $\int_0^x \exp(-x^2)dx$  evaluated in polar coordinate and Euclidean coordinate vanishes at the limit when  $x \rightarrow 0$  and  $x \rightarrow \infty$ . When the integral is evaluated in finite value of  $x$ , there exists a small but acceptable difference with maximal 0.787% difference at  $x = 1.169$ .

### **$\sigma$ - $\mu$ relationship**

From the approximation of the error function Eq. (4.2.5), we can work out the relation between the means ( $\mu_1, \mu_2$ ) and variances ( $\sigma_1^2, \sigma_2^2$ ) of the two distributions to be discriminated. After simple calculation, the relation between  $\mu_1, \mu_2, \sigma_1$  and  $\sigma_2$  becomes

$$\mu_2 - \mu_1 = C(\sigma_1 + \sigma_2), \quad (4.2.6)$$

where

$$C = \sqrt{\frac{\pi}{2} \ln \left( \frac{1}{1 - (\varepsilon - 1)^2} \right)}$$

is a constant determined by the misclassification rate  $\varepsilon$  under Normal distribution.

Besides, relation (4.2.6) is true for any distributions under Weber's law. The reason is stated as follows.

It is stated earlier that for the worst possible probability density function that maximize the classification error of discriminator  $x_0$  gives a classification

error (Cooke and Peake, 2002)

$$\varepsilon = \frac{\sigma^2}{\sigma^2 + (x_0 - \mu)^2}.$$

If we have two distributions with only known mean and variance  $(\mu_1, \sigma_1^2)$  and  $(\mu_2, \sigma_2^2)$ , the worst possible misclassification rate is

$$\varepsilon = \frac{\varepsilon_1 + \varepsilon_2}{2} = \frac{\sigma_1^2}{\sigma_1^2 + (x_0 - \mu_1)^2} + \frac{\sigma_2^2}{\sigma_2^2 + (x_0 - \mu_2)^2}.$$

Taking the form of  $x_0$  given earlier, the equation above is simplified as (compare with Eq.(4.2.6))

$$\mu_2 - \mu_1 = C'(\sigma_1 + \sigma_2),$$

where

$$C' = \sqrt{\frac{1}{\varepsilon} - 1}.$$

For this worst possible case, the relation of the mean and standard deviation is still the same as that derived from the Normal distribution, but only the scale term  $C'$  is of different expression. For this case, the error  $\varepsilon$  is the maximal possible error for misclassification, so  $C'$  would not be much different from  $C$ , whose value is derived from the misclassification rate of Normal distribution

To derive the relation between  $\sigma$  and  $\mu$ , assume  $\sigma$  is a function of  $\mu$ , i.e.  $\sigma = f(\mu)$ . Substitute  $\sigma_1 = f(\mu_1)$  and  $\sigma_2 = f(\mu_2)$  into Eq. (4.2.6), and apply

the first order Taylor expansion on function  $f$  at point  $\mu$ , we have

$$C(2f(\mu) + f'(\mu)(\mu_1 + \mu_2 - 2\mu)) = \mu_2 - \mu_1. \quad (4.2.7)$$

From Weber's law, the relation for  $\mu_1$  and  $\mu_2$  obeys  $\frac{\mu_2 - \mu_1}{\mu_1} = k$ . Substitute  $\mu_2 = (k + 1)\mu_1$  in Eq. (4.2.7) and let  $\mu_1 = \mu$ , it yields

$$f'(\mu) + \frac{2}{k\mu}f(\mu) - \frac{1}{C} = 0.$$

When the neural response rate has a nonlinear relation with respect to the input stimulus intensity (e.g. sigmoid function), the analysis is relatively complicated but the theoretical solution can still be obtained (see Discussion session for details).

## 4.2.2 Superposition process of population neurons

In neural system, discrimination task is not performed by single neurons, but it is processed by a population of neurons interconnected with each. The superposition process (or superimposed process)  $N(t)$  for population neurons is defined as the total number of arrivals of spikes for all neurons that occur up to time  $t$ :

$$N(t) = \sum_{i=1}^p N_{t,i} \quad t \geq 0,$$

where  $N_{t,i}$  is the spike count for the  $i$ th neuron during the time interval  $[0, t]$ . Assume that each neuronal ISI in the population is identical and indepen-

dently following Gamma distribution  $\Gamma(A, B)$ . Even though the expression of the density function of the superimposed ISIs is complicated (Cox and Miller, 1965; Lawrance, 1973), the superimposed counting statistics (mean and variance) in a small time window  $W$  can be found theoretically.

Define the correlation among network neurons by the spike train correlation between pair-wised cells spike counts  $n_i$  and  $n_j$  over a sliding window of length  $W$ :

$$\rho_W = \frac{\text{cov}(n_i, n_j)}{\sqrt{\text{var}(n_i)\text{var}(n_j)}}.$$

The superposition process of correlated spike trains of population neurons of size  $p$  over sliding window  $W$  can be found as:

$$Y = \mu + \frac{1}{p} \cdot \mathbf{1}_{1 \times p} M^{\frac{1}{2}} (\mathbf{X} - \boldsymbol{\mu})$$

where  $Y$  stands for the standard superimposed spike count and

$$\mathbf{X} = \begin{pmatrix} x_1 \\ x_2 \\ \vdots \\ x_p \end{pmatrix}$$

is the spike rate of each neuron in the network with

$$\begin{aligned} \mathbb{E}(\mathbf{X}) &= \mu \mathbf{1}_{p \times 1} = \boldsymbol{\mu} \\ \text{cov}(\mathbf{X}) &= \sigma^2 \mathbb{I}_{p \times p} \end{aligned}$$

( $\mathbb{I}$  is the identical matrix) and  $M$  is the correlation matrix of the form

$$M = \begin{bmatrix} 1 & \rho & \dots & \rho \\ \rho & 1 & \rho & \vdots \\ \vdots & \rho & \ddots & \rho \\ \rho & \dots & \rho & 1 \end{bmatrix}.$$

Therefore, the standard superimposed spike count rate is

$$\begin{aligned} \mathbb{E}(Y) &= \mu \\ \text{var}(Y) &= \sigma^2 \left( \frac{1 + (p-1)\rho}{p} \right). \end{aligned}$$

If  $\rho = 0$ , this is independent superposition process  $Y$  with  $\mathbb{E}(Y) = \mu$ , and  $\text{var}(Y) = \sigma^2/p$ .

### 4.2.3 Competition attractor network

The model of a competition based network for decision making was originally proposed by Brunel and Wang (Brunel and Wang, 2001) and further studied by Deco and Rolls (Deco and Rolls, 2006). The task of the network is

to make a decision between two possible alternatives, according to the characteristics of a sensory input, by reaching one of two predetermined firing states. A typical task is the comparison of two different stimuli, e.g. vibrotactile stimulation frequency.

The network is composed of four pools of fully connected leaky integrate-and-fire neurons, both excitatory and inhibitory. The pools are divided according to the strength of the connections between the neurons (Fig. 4.7A). Each pool receives external inputs in the form of excitatory spikes with a Poisson distribution; the frequency of the inputs depends on the stimuli characteristic to be compared. A decision is reached when one of two specialized excitatory neurons pools (pool A or pool B) reaches a high frequency (30 to 60 Hz) firing state, while the other is almost silent. Competition is made possible by a pool of inhibitory neurons, which usually fire at about 20 Hz. Inhibitory pool suppresses the activity of one of the two specialized pools, while the nonspecific pool is consisted of nonspecialized excitatory neurons which do not react to the stimuli characteristics. More details on the network architecture can be found in the supplementary material and Wang (Wang, 2002).

The network reaches a correct decision when the high-rate firing pool is the one with the larger input frequency; otherwise the decision is considered "wrong". Deco and Rolls have shown (Deco and Rolls, 2006) that for a certain input range the network follows Weber's law, in the sense that the difference between input frequencies required to achieve, over many trials, a certain success rate (85% in this paper) is proportional to the amplitude of one of the two

input frequencies.

We rebuilt the competition based neural network model (Fig. 4.7A) and measured the value of  $CV_{ISI}$  for each pool, verifying that Weber's law holds for our implementation of the model. The input ( $F_{in}$ ) to one of the specialized pools (say, pool A) is considered as the reference input (Fig. 4.7A), while the reference input frequency  $\Delta F_{in}$  was chosen in a range that allows the network not to be saturated by the inputs. The input frequency  $F_{in} - \Delta F_{in}$  applied to pool B is set between 30% and 100% of the reference input frequency (thus,  $\Delta F_{in}$  varied between 0 and  $0.7F_{in}$ ). For each pair of input frequencies, 200 simulations were run, and the success rate achieved for each pair was recorded. A curve of the success rate versus  $\Delta F_{in}$  can be drawn for each reference value  $F_{in}$ . By fitting the curve for each value of  $F_{in}$ , the  $\Delta F_{in}$  value achieving a certain success rate can be found.

We then altered the input spike train so that Weber's law does not hold for the discrimination task, by applying a different input spike distribution. The distribution of the interspike intervals was altered to be uniform between 0 and twice the average interval, which is the reciprocal of the input frequency. The rest of the network setup remains the same.

## 4.3 Results

### 4.3.1 Weber's law in firing rate

In the previous section, we have derived the relation between the mean ( $\mu$ ) and standard deviation ( $\sigma = f(\mu)$ ) of the neuronal discharge rate from Normal distribution when Weber's law holds

$$f'(\mu) + \frac{2}{k\mu}f(\mu) - \frac{1}{C} = 0.$$

where  $k$  is the Weber's constant ranging from 0.05 to 0.3 (Gescheider et al., 1990) and  $C$  is a constant determined by the misclassification rate  $\varepsilon$ . The value of the misclassification criterion  $\varepsilon$  (ranging from 5% to 20%) is not crucial to the final result.  $\varepsilon$  is fixed to be 15% (Deco and Rolls, 2006) in this section and as a result  $C \approx 1.4$ . The ordinary differential equation (4.2.7) describes the relationship between the first two order statistics of the neuronal firing rate. A general solution for this first order non-homogeneous ODE is

$$\sigma = f(\mu) = \frac{k}{C(k+2)}\mu + \mu^{-2/k}c_0 \quad (4.3.1)$$

where  $c_0$  is a constant determined by the initial condition. The second term  $\mu^{-2/k}c_0$  in Eq. (4.3.1) can be neglected (since  $k$  is much smaller than 1, and discharge rate  $\mu$  is fixed within 0 to 200 spikes/sec), so the standard deviation

$\sigma$  and the mean  $\mu$  of the discharge rate have a linear relation.

$$\sigma = \frac{k}{C(k+2)}\mu \quad (4.3.2)$$

We call Eq. (4.3.2) *Weber's Equation*. On the one hand, Weber's Equation is derived from Weber's law; on the other hand, Weber's law is satisfied when the mean and standard deviation of the neuronal discharge rate obey Weber's Equation. Theoretical derivation can be found in method section. Moreover, even though this linear relation between  $\sigma$  and  $\mu$  in Weber's Equation is derived from Normal distribution, this result can be generalized to any distribution, even a distribution with only known mean and variance, by just varying the expression of the scaling parameter  $C$ .

We firstly test Weber's law on single neuron level, by examining the neuronal firing rate and interspike intervals in the presence of various stimulus intensities. The detailed simulation results are presented in the following sessions.

### 4.3.2 Single neurons

A simulation for this normally distributed spiking rate with its mean  $\mu$  and STD  $\sigma$  satisfying Weber's Equation is shown in Fig. 4.1A for different values of  $k$ . The simulated ratio of  $\Delta\mu/\mu$  is smaller than the given Weber constant  $k$  (simulated slopes = 0.04, 0.07, 0.14 and 0.22, respectively). This smaller ratio can be caused by the truncation error at the higher order of the

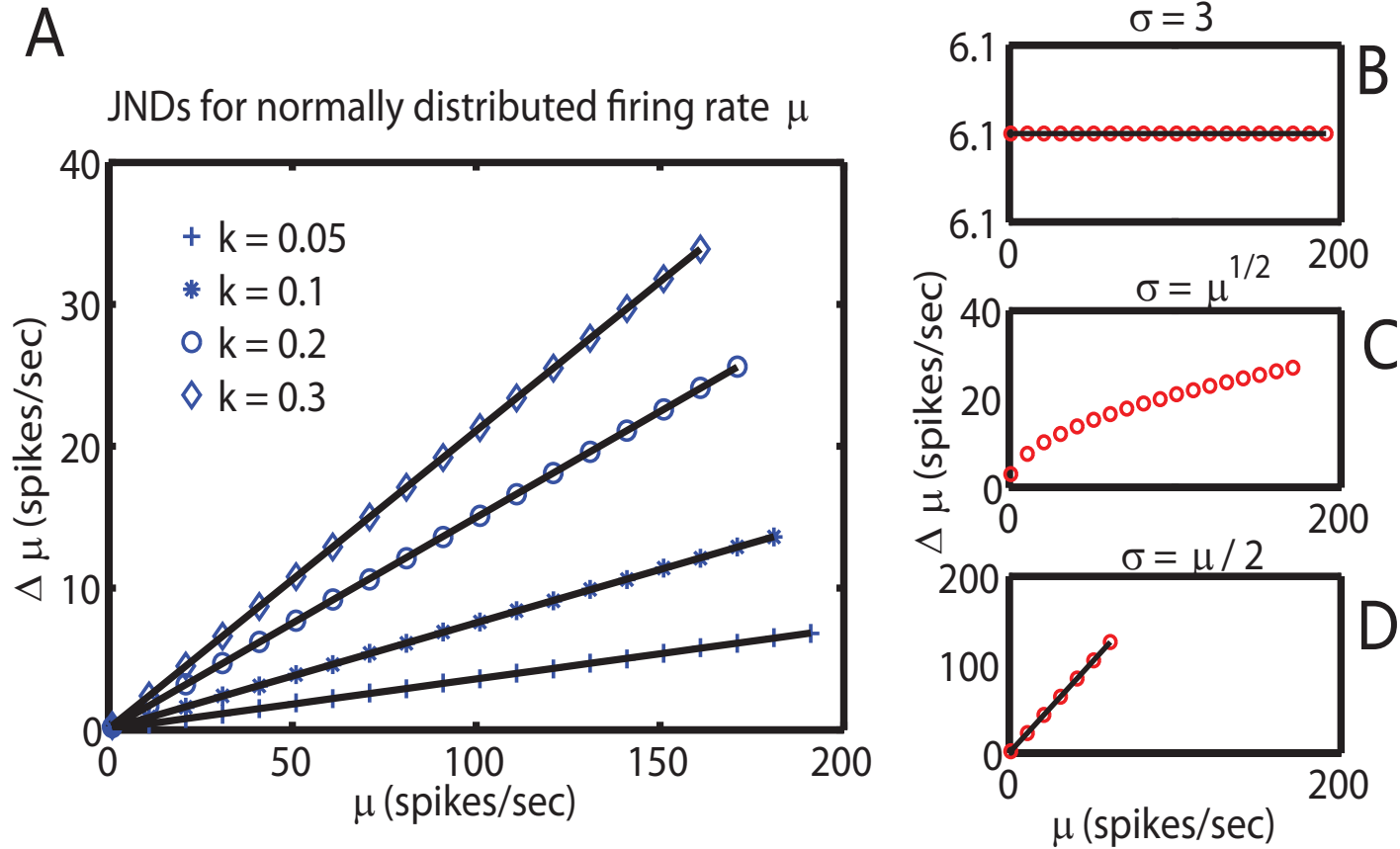


**Figure 4.1** The relation of JNDs and reference spiking intensity  $\mu$  for normally distributed firing rate under different  $\sigma - \mu$  relations. **(A)** Under Weber's Equation, the JNDs is a linearly increasing function of the firing rate with different slopes at different values of Weber's constant  $k$ . The simulated JNDs have a relatively smaller slope than  $k$ , possibly raised from the truncation error from the approximation form. **(B-D)** Examples for  $\sigma - \mu$  relation not satisfying Weber's Equation, where **(B)** STD is constant  $\sigma = 3$ , **(C)**  $\sigma = \mu^{1/2}$ , and **(D)**  $\sigma = \mu / 2$ .

Taylor expansion and the approximation of the error function (see Method). However, Weber's law provides a perfect description of linearity between the JNDs  $\Delta\mu$  and reference firing intensity  $\mu$ .

The relation between JNDs  $\Delta\mu$  and  $\mu$  is also shown when they do not follow Weber's Equation as counter examples. In Fig. 4.1B, when the standard deviation  $\sigma$  of the Normal distribution is constant, and consequentially, the JNDs  $\Delta\mu$  is a constant value for any reference rate  $\mu$ . The reason is that the Normal distribution with different means but constant variance is just a shift without changing its shape. Thus, for fixed misclassification rate ( $\varepsilon = 15\%$ ),  $\Delta\mu$  is always the same for discrimination. When the STD ( $\sigma$ ) equals to the square root of mean  $\mu$  ( $\sigma = \mu^{1/2}$ , Fig. 4.1C), and in turn  $\Delta\mu$  has a non-linear relation with respect to  $\mu$  ( $\Delta\mu = \frac{2C\mu}{\sqrt{\mu-C/2}}$ ), the plausible range of the scale parameter in Weber's Equation ( $\sigma = b\mu$ ) is  $b \in [0.02, 0.1]$  (since  $C \approx 1.4$  in Eq.(4.3.2)). If coefficient parameter  $b$  goes beyond the plausible range ( $\sigma = \mu/2$ , Fig. 4.1D), the JNDs  $\Delta\mu$  is still a linear function of the reference rate  $\mu$  but with the slope  $k' \approx 2.1$  (since the slope  $k' = \frac{2bC}{1-bC}$ ,  $b = 1/2$  in Fig. 4.1D), which is much larger than realistic psychophysical values ( $k \in [0.05, 0.3]$ ).

### 4.3.3 Weber's law in single neuronal ISIs

Many researchers have pointed out that Poisson or renewal process is more appropriate to describe the neuronal firing activity (Cox D. R, 1954; Cox and Miller, 1965). Assume that the interspike interval  $T$  of a spiking neuron

follows Gamma distribution, i.e.  $T \sim \Gamma(A, B)$ , with mean  $\mu_T = AB$  and variance  $\sigma_T^2 = AB^2$ . Exponential distribution is a special case of Gamma distribution when the parameter  $A = 1$ . The coefficient of variation of the interspike interval ( $CV_{\text{ISI}}$ ) equals to

$$CV_{\text{ISI}} = \frac{\sigma_T}{\mu_T} = \frac{\sqrt{AB}}{AB} = \frac{1}{\sqrt{A}}.$$

If ISIs follow Gamma distribution, the corresponding neural spike rate can be described by a renewal process, and the spike rate have mean  $\mu = 1/E(T) = 1/(AB)$  and variance  $\sigma^2 = \text{var}(T)/(E(T))^3 = 1/(A^2B)$  (Cox and Isham, 1980). Substitute the mean spiking rate  $\mu$  and variance  $\sigma^2$  in the Weber's Equation by the two parameters  $A$  and  $B$  of the Gamma distribution, and express the Weber's Equation by  $CV_{\text{ISI}}$ ,

$$CV_{\text{ISI}} = \frac{k}{C(k+2)} \sqrt{\frac{1}{AB}} = \frac{k}{C(k+2)} \sqrt{\mu}.$$

In the above expression,  $\mu$  only represents the quantity of the firing rate and is invariant under different dimensions. If  $CV_{\text{ISI}} = 1$ , the neural discharge follows Poisson process. If  $CV_{\text{ISI}} > 1$ , we call the renewal process *super-Poisson process*; when  $CV_{\text{ISI}} < 1$ , it is *sub-Poisson process* (in physics, the super-Poisson process is defined by the index of dispersion variance-mean ratio (VMR) of the counting of events with  $\text{VMR} > 1$ , and sub-Poisson is similarly defined as  $\text{VMR} < 1$  (Kolobov, 1999). Besides,  $\text{VMR} = CV_{\text{ISI}}^2$  in

renewal process). For a very regular spike train ('pacemaker'), the histogram of ISIs has a very narrow peak and  $CV_{\text{ISI}} \rightarrow 0$ . In the case of a random spike train (Poisson process), the ISIs are exponentially distributed and  $CV_{\text{ISI}} = 1$ . The  $CV_{\text{ISI}}$  can be larger than one in the case of a multistate neuron (Wilbur and Rinzel, 1983). The range of  $CV_{\text{ISI}}$  under Weber's law can be determined from the range of the Weber's constant ( $k \in [0.05, 0.3]$ )

$$\frac{\sqrt{\mu}}{100} < CV_{\text{ISI}} = \frac{k}{C(k+2)}\sqrt{\mu} < \frac{\sqrt{\mu}}{10}, \quad (4.3.3)$$

where  $C = 1.4$ . Define Eq.(4.3.3) as *Weber's range* for single neuron. The detailed relation between the parameters is presented in Table 4.1. For single neuron,  $CV_{\text{ISI}}$  is rather small (0.14 - 0.3) for biological feasible firing rate ( $10 \leq \mu \leq 200$  Hz), which means the neuron fires very regularly. However, the small value of  $CV_{\text{ISI}}$  contradicts the irregularity of the cortical neuronal discharge behavior *in vivo*.

Several simulation examples are presented to demonstrate the range of the feasible firing rate under which Weber's law holds, by examining the spike count over a small sliding time window ( $W = 20$  ms). In the simulation, the ISIs follow Gamma distribution with fixed parameter  $A = \frac{1}{CV_{\text{ISI}}^2}$  and rate-dependent parameter  $B = \frac{1}{\mu A}$ .

Fig. 4.2 demonstrates the relation between the JNDs of firing rate  $\Delta\mu$  and  $\mu$  for sub-Poisson, Poisson and super-Poisson discharge process. For sub-Poisson process (Fig. 4.2A), linear relationship between  $\Delta\mu$  and  $\mu$  is

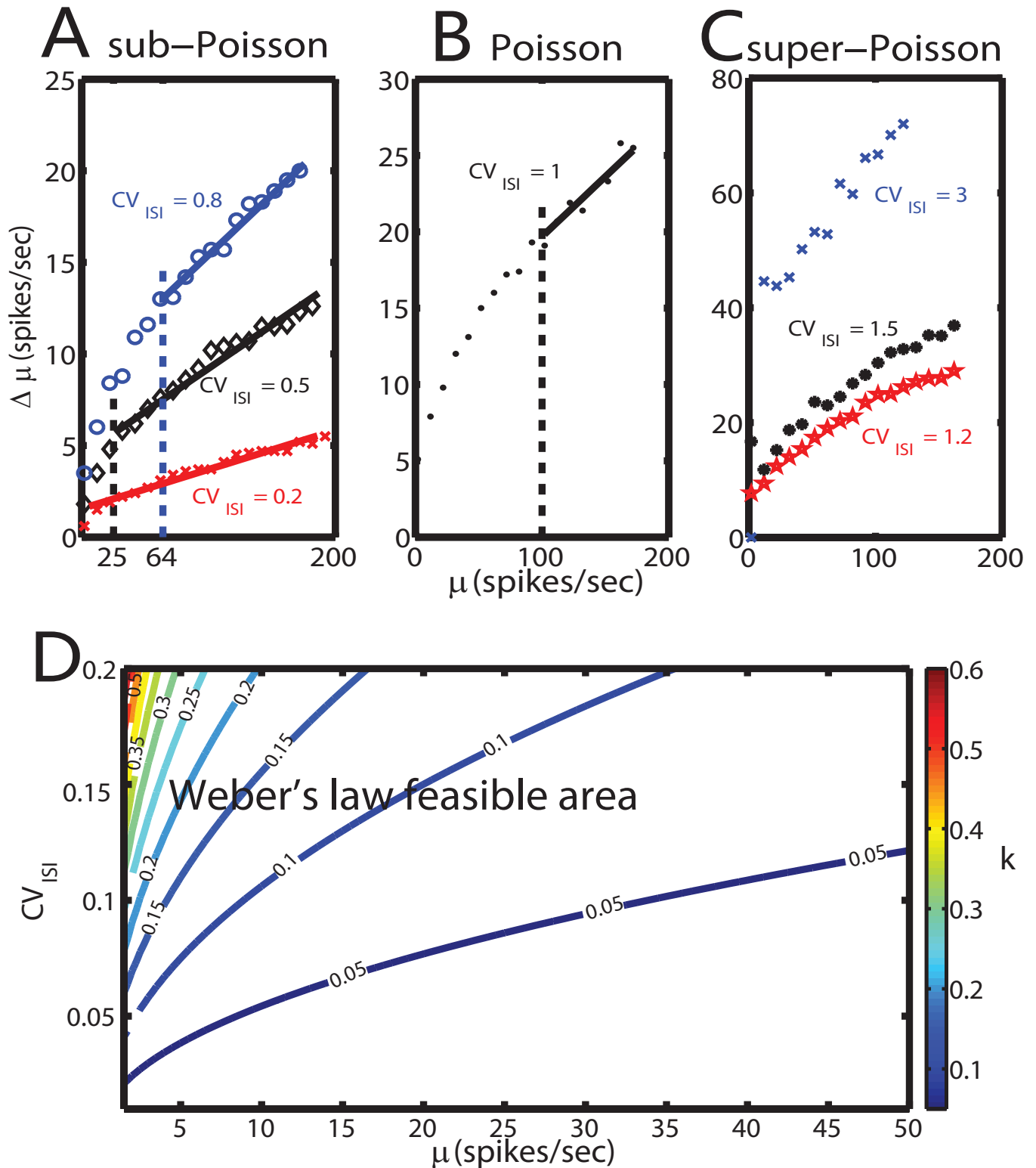


**Figure 4.2** The relation of JNDs and reference spiking intensity  $\mu$  for (A) sub-Poisson, (B) Poisson, and (C) super-Poisson neural discharge process. The vertical dashed line represents the lower bound of the feasible ranges of the neuronal firing rate under Weber's range. (D) The contour plot of Weber's constant  $k$  indicating Weber's law feasible region in terms of the firing intensity ( $\mu$ ) and dispersion of the ISI ( $CV_{ISI}$ ).

more notable for relatively small value of  $CV_{\text{ISI}}$  (0.2) than that of large values of  $CV_{\text{ISI}}$  (0.5 and 0.8), but the slope of the linear regression curve for  $CV_{\text{ISI}} = 0.2$  is much smaller (0.02) than Weber's constant. For Poisson process, Weber's law does not hold when the firing rate  $\mu < 100$  Hz (Fig. 4.2B and Table 2.1), since the increasing trend of  $\Delta\mu$  is nonlinear with respect to  $\mu$ . In contrast, when  $\mu > 100$  Hz, the relation between JNDs  $\Delta\mu$  and reference firing rate  $\mu$  is linear (slope = 0.06). For super-Poisson process ( $CV_{\text{ISI}} = 1.2, 1.5$  and 3, Fig. 4.2C), Weber's law cannot be satisfied because of the nonlinearity of the curves. Moreover, the  $y$ -axis intercept of these curves does not pass the origin (0, 0). Fig. 4.2D is the contour plot of Weber's constant  $k$  versus  $CV_{\text{ISI}}$  and firing rate  $\mu$ . It illustrates the range of  $CV_{\text{ISI}}$  and firing rate  $\mu$  when  $k$  lies within [0.05, 0.3].

Fig. 4.3 shows the ISI distribution when  $CV_{\text{ISI}}$  and firing rate  $\mu$  follows Weber's Equation. The interspike interval distribution bends towards longer ISI time for larger  $CV_{\text{ISI}}$  because of the nonlinear relation between  $CV_{\text{ISI}}$  and the mean firing rate  $\mu$  under Weber's Equation (Eq.(4.3.2)).

From the experimental observations on cortical neuronal discharge variability, the  $CV_{\text{ISI}}$  should be from 0.5 to 1, which is much bigger than the  $CV_{\text{ISI}}$  value under Weber's range (0.14 to 0.3) for single neuron. The discrimination behavior cannot be performed by single cortical neurons, and thus, population neurons need to be considered.

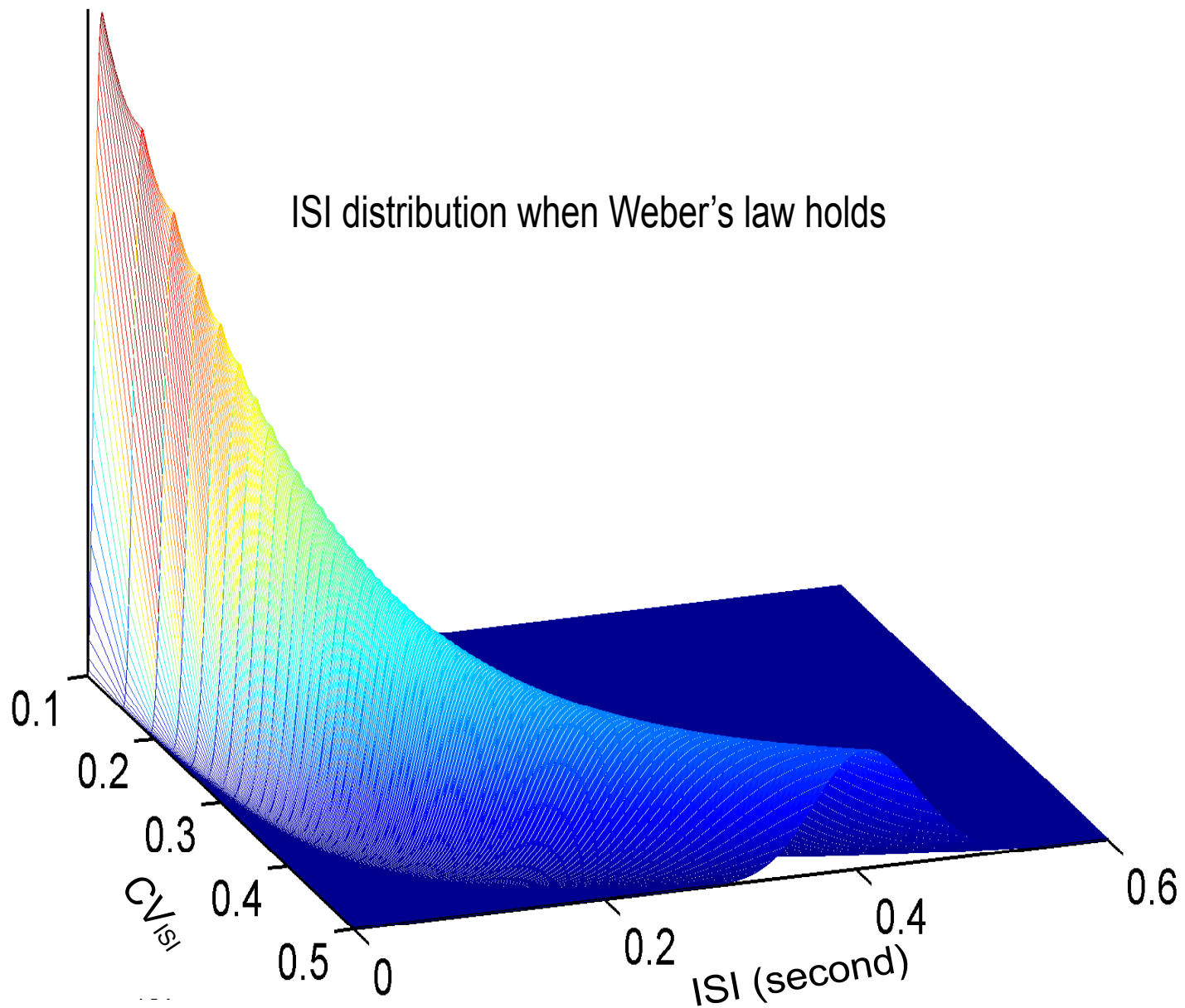


**Figure 4.3** ISI distribution when Weber's law is satisfied. The ISI is assumed to follow Gamma distribution, and the histogram of the ISI under Weber's Equation reveals the property that the distribution is wider at low firing intensity and has big dispersion of ISI. It becomes narrower as the firing rate increases and the discharge process becomes more regular ( $CV_{ISI}$  becomes smaller).

### 4.3.4 Superposition of independent neural discharge process

Let us begin with the superimposed population neurons, with each neuron firing independently. Assume each individual neuron's firing pattern follows identical distribution with mean discharge rate  $\mu$  and standard deviation  $\sigma$ . If each neuron fires independently, the mean discharge rate  $\mu$  after superposition is still the same as single neuron, but the variance of the instantaneous spike count becomes  $\sigma^2/p$ , where  $p$  is the population size. Therefore, substitute  $\mu$  and  $\sigma^2/p$  into Weber's Equation, we have

$$CV_{\text{ISI}} = \frac{k}{C(k+2)} \sqrt{\mu p}$$

As a result, Weber's range can be derived from Inequality (4.3.3)

$$\frac{\sqrt{\mu p}}{100} < CV_{\text{ISI}} < \frac{\sqrt{\mu p}}{10},$$

where the value of  $CV_{\text{ISI}}$  depends on neuronal discharge rate  $\mu$  and population size  $p$ . The range for the firing rate  $\mu$  can be determined for a given population size  $p$  such that Weber's law holds (see Table 4.1 for detailed range of parameters).

The simulation results and illustrative parameter relation are shown in Fig. 4.4. and 4.5A. The first row of Fig. 4.4 shows the case for a large population size ( $p = 1000$ ). From Table 4.1,  $CV_{\text{ISI}}$  has to be large if the population

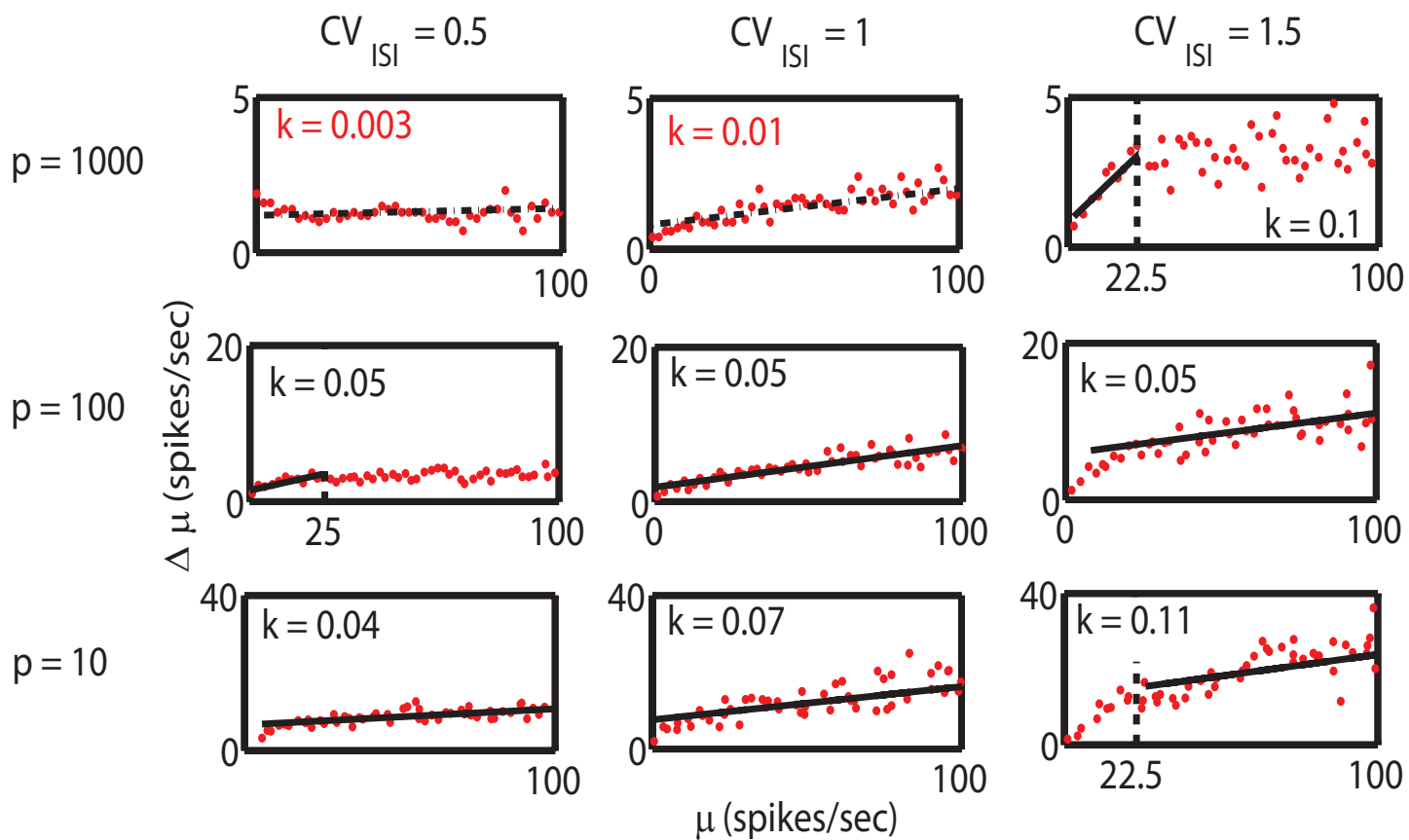


**Figure 4.4** The relation of JNDs and standardized reference spiking intensity  $\mu$  for sub-Poisson ( $CV_{ISI} = 0.5$ ), Poisson ( $CV_{ISI} = 1$ ) and super-Poisson ( $CV_{ISI} = 1.5$ ) neural discharge under independent superposition process with different population size ( $p = 1000, 100$  and  $10$ ). The simulated data are fitted by linear regression and the slopes are indicated in each plot. One can see that Weber's law cannot describe the relation of JNDs and reference intensity  $\mu$  well when the population size is big (upper panel) and when neuronal discharge process are more regular (left column). The vertical dashed line represents the lower or upper bounds of the feasible range of firing intensity, and the red  $k$  indicates the situation when Weber's law does not hold at all.

size is large ( $CV_{\text{ISI}} > 4.5$ ). Thus, for a large population, each individual neuron should have a very irregular discharge process ( $CV_{\text{ISI}} \gg 1$ ) so that Weber's law is satisfied, but it is biologically unrealistic and impossible. From the simulation, if the value of  $CV_{\text{ISI}}$  is small (e.g.  $CV_{\text{ISI}} = 0.5$ , Fig. 4.4. upper left panel), the JNDs are very small as the population firing rate is extremely narrowly distributed, so Weber's law does not hold for independent superposition of large population. When the population size is relatively small ( $p = 100$ ), the Poisson process describes Weber's law the best (Fig. 4.4. central plot, and Table 4.1). If population size is very small ( $p = 10$ ), the firing intensity should be bigger than a certain minimal value (refer to Table 4.1), and Weber's law holds for sub-Poisson and Poisson neural discharge process (Fig. 4.4, bottom panel). Fig. 4.5A depicts the  $CV_{\text{ISI}}$  values versus different firing rates and population sizes. The value of  $CV_{\text{ISI}}$  is unrealistically large (30) at high firing rate (100 Hz) and large population size (1000). The different layers in Fig. 4.5A represented different values of the Weber's constant  $k$ , and  $CV_{\text{ISI}}$  increases with  $k$  dramatically.

This result is interesting. For Weber's law implementation on independent population neurons, it demonstrates that a small group of neurons, rather than large population neurons, can perform the discrimination task very well (actually  $p = 10$  is sufficient for  $0.5 < CV_{\text{ISI}} < 1$ , see Table 4.1). If population size is too large ( $p > 1000$ ), Weber's law can be satisfied only if each single neuron generates its action potential at a highly irregular process ( $CV_{\text{ISI}} > 4$ ), which is biologically impossible. The result is consistent with the experimen-

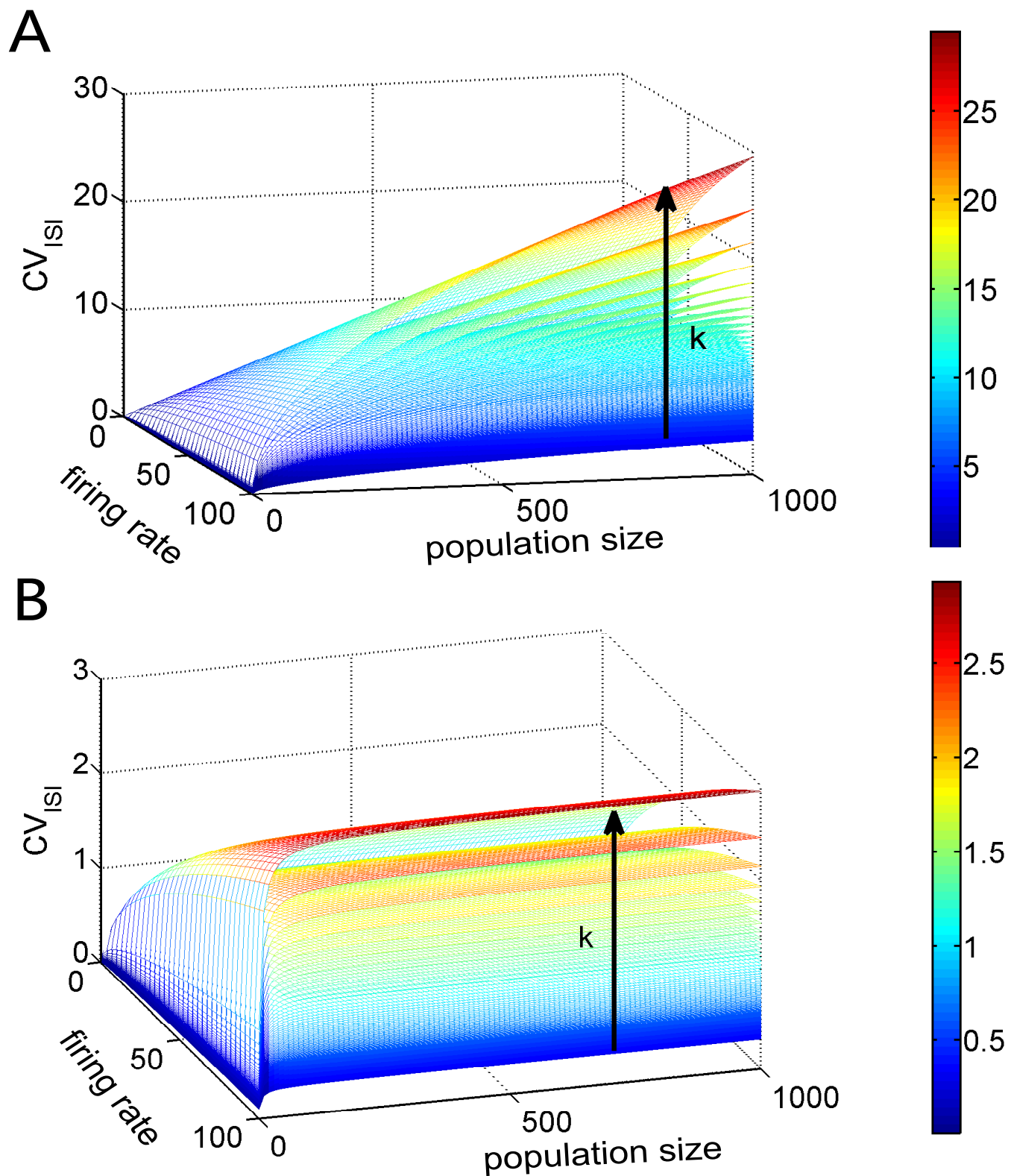


**Figure 4.5** The parameters relation under Weber's Equation for (A) independent superposition process and (B) correlated superposition process. (A) If population neurons are independent,  $CV_{ISI}$  tends to be extremely large under high firing rate and large population size. Different layers represent different values of the Weber's constant  $k$ . When  $k$  gets bigger,  $CV_{ISI}$  increases dramatically. (B) Under weakly correlated superposition process, the saturated value of  $CV_{ISI}$  is around 3 when population size tends to infinity at firing rate 100 Hz.  $CV_{ISI}$  is an increasing function of the Weber's constant  $k$  and the firing rate  $\mu$ .

tal observation by Britten et al (Britten et al., 1992).

However, the assumption of statistical independence among cortical neuron interactions is not realistic. Nearby cortical neurons are usually highly interconnected and sharing common inputs. Robust correlations among neuronal activity have been reported in a number of cortical areas from electrophysiological recordings, with an averaged correlation coefficient typically ranging from 0.1 to 0.2 (Britten et al., 1992; Gawne and Richmond, 1993). What the effect would be if correlation between neurons is introduced?

#### 4.3.5 Superposition of correlated neural discharge process

Cortical cells do not generate spikes independently, but rather, the spiking activity is correlated, spatially and temporally (Smith et al., 2008). Correlation arises from shared excitatory and inhibitory inputs (Morita et al., 2008), either from other stimulus-driven neurons or from ongoing activities (Fiser et al., 2004). In this chapter, we only concentrate on the effect of spatial correlation on neural spike trains, and we only consider the positive correlation here.

Assume that each neuron in the population is pair-wise correlated with the same coefficient correlation  $\rho = 0.1$ , and Weber's Equation becomes (see Methods for detailed derivation)

$$CV_{\text{ISI}} = \frac{k}{C(k+2)} \sqrt{\frac{\mu p}{1 + (p-1)\rho}}.$$

Therefore, the corresponding Weber's range becomes (compare with inequality (4.3.3)):

$$\frac{\sqrt{\frac{\mu p}{1+(p-1)\rho}}}{100} < CV_{\text{ISI}} < \frac{\sqrt{\frac{\mu p}{1+(p-1)\rho}}}{10}.$$

As the population size  $p \rightarrow \infty$ , we have

$$\frac{\sqrt{\frac{\mu}{\rho}}}{100} < CV_{\text{ISI}} < \frac{\sqrt{\frac{\mu}{\rho}}}{10}.$$

Consequently, the values of  $CV_{\text{ISI}}$  lie in between  $[0.45, 1]$  for neuronal discharge rate  $10 < \lambda < 200$  Hz for infinite population neurons (see Table 4.1). The simulation results are presented in Fig. 4.6. When the population size  $p$  is 10, the feasible range of firing rate has a lower bound—the boundary is proportional to  $CV_{\text{ISI}}$  (Table 4.1 and Fig. 4.6. bottom panel). When the population size  $p$  increases to 100, Weber's law holds (Fig. 4.6, middle panel). When population size increases from 100 to 1000, there is no significant improvement on the linear relation, but rather, the JND reveals more random property at super-Poisson process ( $CV_{\text{ISI}} = 1.5$ , Fig. 4.6, upper-right panel). Besides, for large population size ( $p = 1000$ ),  $\Delta\mu$  is very big ( $\approx 15$  Hz) at low firing intensity ( $\mu = 2$  Hz), which is not biologically plausible. The effect of the weak correlation ( $\rho = 0.1$ ) among neurons in the superposition process can be seen from Fig. 4.5B. The value of  $CV_{\text{ISI}}$  is bounded above by  $\sqrt{\frac{\mu}{10}}$ , which is approximately 3 for  $\mu = 100$  Hz and  $k = 0.3$ . The different layers of the mesh represent different values of the Weber's constant  $k$ , and most regions

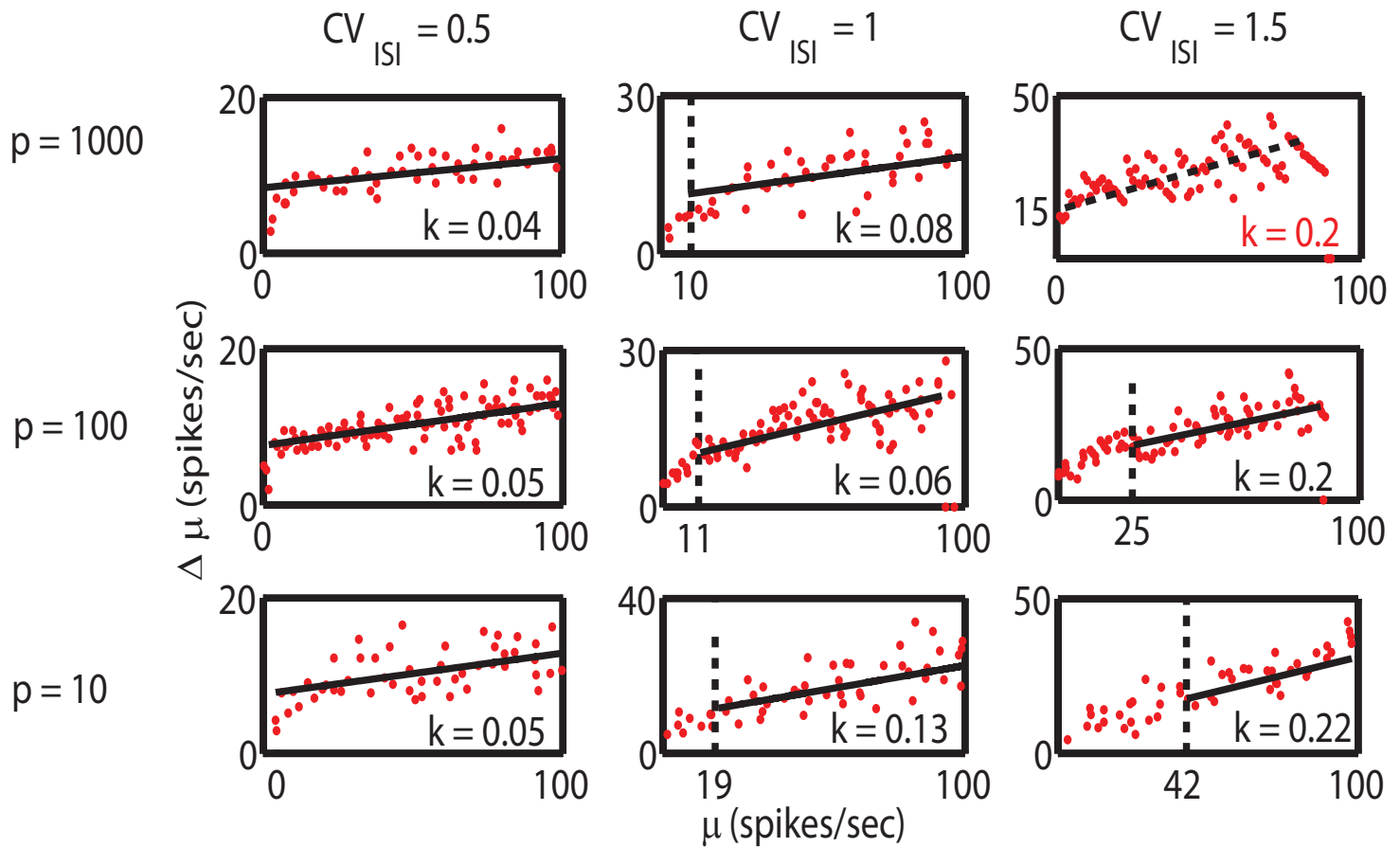


**Figure 4.6** The relation of JNDs and standardized reference spiking intensity  $\mu$  for sub-Poisson ( $CV_{ISI} = 0.5$ ), Poisson ( $CV_{ISI} = 1$ ) and super-Poisson ( $CV_{ISI} = 1.5$ ) process under correlated superposition process with different population size ( $p = 1000, 100$  and  $10$ ) and correlation coefficient  $0.1$ . The simulated data are fitted by linear regression and the slopes are indicated in each plot. The neuronal discharge rate has a lower bound for small population ( $p = 10$ , bottom panel) but fitting is quite well for relative large population size ( $p = 100$  or  $1000$ ). The vertical dashed line represents the lower bounds of the feasible range of firing intensity, and the red  $k$  in the top-right corner indicates the situation when Weber's law does not hold, even though the slope of the linear regression looks reasonable. Note that Weber's law holds well under small  $CV_{ISI}$  ( $0.5$ ), which is consistent with our theory and Table 4.1.

of  $CV_{\text{ISI}}$  lie below one for small values of  $k$ .

Shadlen and Newsome (Shadlen and Newsome, 1998) pointed out that the fidelity of signal transmission approaches an asymptote at 50 to 100 input neurons, and that there is little to be gained by involving more neurons in psychophysical performance. In our simulations, the performance of the population neurons of size 100 with correlation 0.1 matches their experimental observations very well.

### **4.3.6 Neural network based on competition attractor network**

In order to confirm our theoretical results ( $0.5 < CV_{\text{ISI}} < 1$ ) derived from Weber's law, we use the model based on a competitive attractor network for decision making (Fig. 4.7A), firstly proposed by Brunel and Wang (2001) and subsequently examined by Deco and Rolls (2006). The  $CV_{\text{ISI}}$  of neuronal interspike intervals for each pool of the network was calculated. The description of construction of the network is presented in the Method section.

In this neural network model, the input spike train follows Poisson process, and the network can make the decision following Weber's law (Fig. 4.7). The measured  $CV_{\text{ISI}}$  values in inhibitory, nonspecific and winning pools (see Fig. 4.7A) are all less than one, while the losing pool has  $CV_{\text{ISI}} > 1$ . When the input spike train follows a different distribution (ISIs uniformly distributed between 0 and  $2/F_{in}$ , where  $F_{in}$  is the input frequency), Weber's



law no longer holds. In this case, the  $CV_{ISI}$  values for the inhibitory, nonspecific and winning pools become greater than one, while the losing pool has  $CV_{ISI} < 1$ .

The results are demonstrated in Fig. 4.7B-E. Fig. 4.7B and 4.7C show the rastergrams of randomly selected neurons from each pool in the network. Fig. 4.7B is the rastergram when the  $CV_{ISI}$  of the winning pool (pool A) is less than one. The spatio-temporal spiking activity shows the transition to the correct final state attractor. When a decision is made (after a transition period of about 700 ms), the winning pool A generates most spikes and becomes highly activated, while the losing pool B becomes relatively silent. This rastergram illustrates how pool A wins the competition and the network performs a transition to a single-state final attractor corresponding to a correct discrimination. Fig. 4.7C is the case when the winning pool A has  $CV_{ISI} > 1$ . Contrary to Fig. 4.7B, the winning pools A with  $CV_{ISI} > 1$  are very silent at the beginning, following by a bursting for a short time (at 700 ms), then have a subsequent phase similar to Fig. 4.7B. The reason that causes the differences between these network behaviours can attribute to the input distribution. Originally, the input spike train follows Poisson distribution (or equivalently, the interspike interval is exponential distribution heavily distributed near zero), and this entails a very short transition time, after which the total network input is more or less constant. In the alternative case, the input spike train have its ISIs following uniform distribution, and this implies that the total input to the network is lower at the beginning of the simulation, then peaks around

time  $2/F_{in}$  (which is 660 ms since  $F_{in}$  is 3 Hz) and finally becomes nearly constant; this trend in the total input level is mirrored by the network firing activity.

Fig.4.7D plots the linear relationship between the values of  $\Delta F$  and  $F$  (where  $F$  is the input spike frequency) when the winning pool has  $CV_{ISI} < 1$ , supporting our theoretical results for Weber's law. The misclassification rate is fixed to be 15% and the linear regression has slope  $k$  that varies between 0.24 and 0.32. Fig. 4.7E is the case when the winning pool has  $CV_{ISI} > 1$ , and as a result, the relationship between the reference frequencies  $F$  and the values of  $\Delta F$  is far from linear and is not even monotone.

## 4.4 Discussion

In this chapter, I derived the linear relationship between the mean and the standard deviation of neuronal discharge rate when Weber's law holds, and expressed the relation in terms of  $CV_{ISI}$ . It is found that under Weber's law ( $CV_{ISI} \in [0.45, 1]$ ), neurons generate more regular spikes than a Poisson process. For single neuron, relative regular discharge process can satisfy Weber's law, but for superimposed population neurons, the firing variability can be larger either with a small group of independent spiking neurons or a large group of correlated cortical cells. The findings may shed light on the theory between cortical neuronal firing property and this psychophysical law quantitatively.

#### 4.4.1 Nonlinear relation of stimulus-neuronal responses

Cortical neurons *in vivo* usually have a nonlinear response to external stimulus, and the input-output relation is commonly described by a sigmoid function (S-shaped). We carry out the analysis on this nonlinear input-output relation to show that our conclusions based on the linear assumption in the Method section still hold.

One of the commonly used sigmoid functions to describe the relation between the input stimulus ( $I$ ) and the mean output neural response rate ( $\mu$ ) is of the form

$$\mu = \frac{R_0}{1 + \exp\left(\frac{-k_0(I - \frac{1}{2}I_0)}{R_0}\right)}, \quad (4.4.1)$$

where the parameters  $R_0$ ,  $I_0$  and  $k_0$  represent the maximal neural response rate, the maximal input stimulus intensity, and the steepness (larger  $k_0$  implies a step function), respectively. When the neuronal-stimulus relation is of sigmoid function (Fig. 4.8A, dashed line) instead of linear (Fig. 4.8A, solid line), the ratio of the increment of the neural firing rate  $\Delta\mu$  over the reference firing intensity  $\mu$  is no longer Weber's constant  $k$ , but can be expressed in terms of the input stimulus intensity  $I$ :

$$g(I) = \frac{\Delta\mu}{\mu} = \frac{\exp\left(\frac{-k_0(I - \frac{1}{2}I_0)}{R_0}\right) - \exp\left(\frac{-k_0((k+1)I - \frac{1}{2}I_0)}{R_0}\right)}{1 + \exp\left(\frac{-k_0((k+1)I - \frac{1}{2}I_0)}{R_0}\right)}.$$

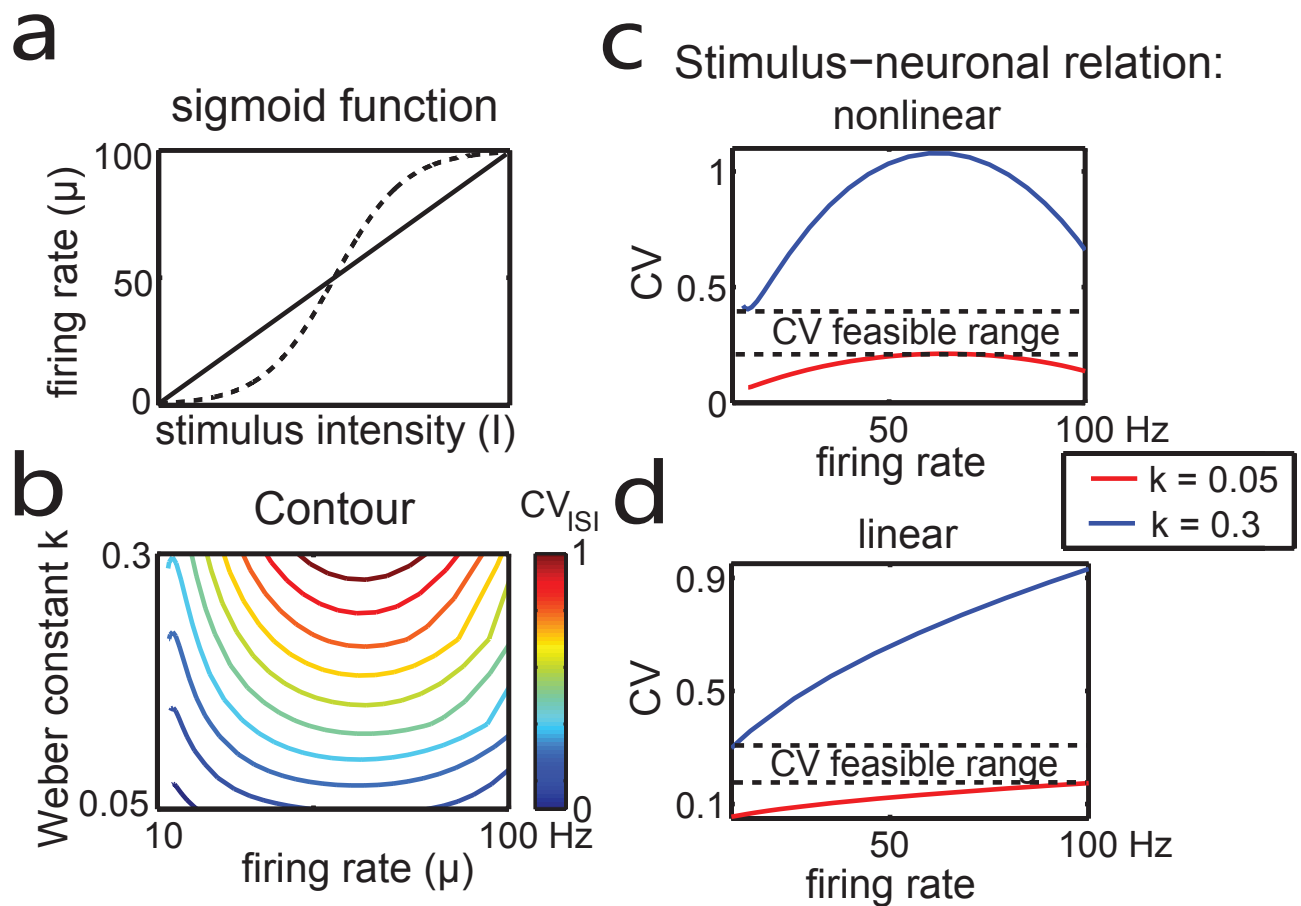


**Figure 4.8:** Analysis on the effects of CVISI range if the input-output relationship between the stimulus intensity and the neural response rate is of sigmoid function. Parameter values used for the numerical simulation are:  $R_0 = 120$ ,  $k$  in  $[0.05, 0.3]$ ,  $k_0$  in  $[0.3, 2]$ . **(a)** Illustration for the sigmoid function compared with linear relation between the neuronal firing rate versus input stimulus intensity. **(b)** Contour plots for CV<sub>ISI</sub> values with respect to firing rate  $\mu$  and Weber's constant  $k$ . **(c)** Numerical solution of CV<sub>ISI</sub> versus firing rate  $\mu$  when the input-output is of nonlinear relation, under different Weber's constant  $k$  (0.05 and 0.3). For every value of  $k$  and  $\mu$ , the feasible range of CV<sub>ISI</sub> in  $[0.2, 0.4]$  is determined by the maximal and minimal value of the red line ( $k = 0.05$ ) and blue line ( $k = 0.3$ ). **(d)** When the input-output are of linear relation, the feasible range of CV<sub>ISI</sub> in  $[0.17, 0.3]$ , as a comparison with the nonlinear case presented in (c).

Re-interpreting Eq. (4.4.1), we have

$$I = \frac{1}{2}I_0 - \frac{R_0}{k_0} \log(R_0/\mu - 1),$$

so  $\Delta\mu/\mu$  can also be expressed in terms of the mean firing rate  $\mu$ :

$$h(\mu) = \frac{\Delta\mu}{\mu} = \frac{R_0}{\mu + (R_0 - \mu) \left(\frac{R_0}{\mu} - 1\right)^k \exp\left(\frac{-k_0 k I_0}{2R_0}\right)}, \quad (4.4.2)$$

Similar to the analysis presented in the Method section, we obtain the first order non-homogeneous ODE under the nonlinear stimulus-neuronal relation from the new expression (Eq. (4.4.2)):

$$f'(\mu) + \frac{2}{\mu h(\mu)} f(\mu) - \frac{1}{C} = 0$$

The ODE above yields a theoretical solution

$$\sigma(\mu) = f(\mu) = \exp(-a(\mu)) \cdot \left( \int \frac{1}{C} \exp(a(\mu)) d\mu + \mu_0 \right),$$

where  $\mu_0$  is the constant of integration determined by the initial condition and

$$a(\mu) = \int \frac{2}{\mu h(\mu)} d\mu.$$

The solution cannot be expressed explicitly, but we can obtain the solution numerically, and calculate the corresponding  $CV_{\text{ISI}}$  with respect to the firing

rate from

$$CV_{\text{ISI}} = \sigma(\mu)\sqrt{\mu}.$$

Fig. 4.8b is the contour plot of the  $CV_{\text{ISI}}$  with respect to Weber's constant  $k$  and firing rate  $\mu$ . The maximum value of  $CV_{\text{ISI}}$  is reached at the middle value of the firing rate (around 60 Hz), because of the nonlinearity of the input-output relation, and  $CV_{\text{ISI}}$  is always smaller than 1 under these parameter regions. Fig. 4.8c and 4.8d is the illustration for the feasible range of  $CV_{\text{ISI}}$  under reasonable biological parameter regions ( $k \in [0.05, 0.3]$  and  $\mu \in [10, 100]$ ). Comparing the effects on  $CV_{\text{ISI}}$  ranges for nonlinear input-output relation (Fig. 4.8c) with the linear case (Fig. 4.8d), the feasible range for  $CV_{\text{ISI}}$  does not change much ( $CV_{\text{ISI}}$  for nonlinear relation;  $CV_{\text{ISI}}$  for linear relation). Therefore, our conclusions obtained from linear stimulus-neuronal relation from the previous analysis still hold for nonlinear input-output relation under Weber's law.

#### 4.4.2 Relation between the mean and variance of neural signal

The Weber's Equation (Eq.(4.3.2)), which describes the linear relation between the standard deviation and the mean of the neural firing rate, is of consistent form with the movement control model proposed by Harris and Wolpert (Harris and Wolpert, 1998), who assumed that the variance of the

neural signal (neuronal firing rate) is proportional to the square of the mean neural signal. There are also experimental and theoretical evidences from force production supporting the linear scaling of force signal variability (STD) with respect to the mean force level as a natural by-product of the organization of motor neurons and muscle fibres (Jones et al., 2002; Faisal et al., 2008).

Some researchers are arguing that neural discharge rate with the standard deviation ( $\sigma$ ) linearly related to the mean ( $\mu$ ) is a super-Poisson control signal because  $\alpha = 1$  in  $\sigma = \kappa\mu^\alpha$ , while a Poisson process should satisfy  $\alpha = 0.5$  (and sub-Poisson process  $\alpha < 0.5$ ) (Feng et al., 2002; Feng et al., 2004). In fact, the definition above only considers the power  $\alpha$  of the mean neural signal but neglects the scale coefficient  $\kappa$ . In this chapter, it is concluded that Weber's law implies neural discharge more regular than a Poisson process ( $CV_{ISI} < 1$ ) even though Weber's Equation matches the case  $\alpha = 1$ . In Weber's Equation, the constant scale  $\kappa$  is very small (range from 0.01 to 0.1), and it is the range of the scale  $\kappa$  that determines the range of  $CV_{ISI} \in [0.5, 1]$  at the given power  $\alpha = 1$ . Hence, the scale factor  $\kappa$  should also be taken into consideration to determine which process (sub-Poisson, Poisson or super-Poisson) the neuronal signal satisfies.

### 4.4.3 Weber's law in single neuron or system level?

Traditional view in sensory physiology attributes to each neuron a unique role in signaling the presence of a particular feature in the visual environment (Barlow and Narasimhan, 1972). In contrast, more recent psychophysical ap-

proaches have tended to emphasize the role of large neuronal networks and pools in solving even simple perceptual problems. It has been widely accepted that subjective intensity is based on the response of population neurons, rather than a single neurons (Vega-Bermudez and Johnson, 1999). However, a most surprising finding of sensory neurophysiology is that single neurons in visual cortex can encode near-threshold stimuli with a fidelity that approximates the psychophysical fidelity of the entire organism (Britten et al., 1992; Celebrini and Newsome, 1994). This finding is understandable (in light of Weber's range for correlated superposition), which implies that psychophysical sensitivity can exceed neural sensitivity by little more, given a modest amount of correlation in the pool of sensory neurons.

In this chapter, I studied both the discharge patterns of single neurons and superimposed population neurons (independent and correlated) when Weber's law is satisfied. To satisfy Weber's law, single neuron has to have a more regular discharge process while population neurons maintain large neuronal discharge variability. This interesting finding is quite consistent with the phenomenon presented in (Newsome et al., 1989), where Newsome proposed one possible explanation that either signals from many neuronal sources are not pooled to enhance the signal strength, or the variability in the responses of similarly tuned neurons is correlated, when the neuronal performance is similar or better than the psychophysical performance.

#### **4.4.4 Variability of spatial correlation in spike train**

The correlation between neuronal spike trains depends on distance between neurons, and neuronal correlation would decrease as the distance increases. Besides, correlation among ISIs can be affected by other factors as well, such as firing rate (de la Rocha et al., 2007), the neuron assembly microscopic structure and type of stimulus (Kohn and Smith, 2005). In this chapter, I have only studied the simplest homogeneous superposition process of the population neurons by assuming that each neuron is independent (or equally correlated, neglecting the spatial effect), identical and evenly weighted. For non-homogeneous population neurons or non-stationary, non-static neuronal discharge, the situation would be much more complicated and we did not discuss it.

Moreover, the idea of linearly summation of neuronal signals may not be the best way to pool neuronal activity in the cortex. A number of psychophysical studies suggest that neuronal signals contribute disproportionately to perceptual judgments. However, Britten and colleagues (Britten et al., 1992) applied the idea of nonlinearly summing the responses of members of each pool, and did not find significant difference from linear summation among pools.

#### 4.4.5 Argument on Weber's law

There are many literatures studying Weber's law from different aspects on neuronal responses. Some literatures defined Weber's law as a logarithmic relationship between the strength of the stimulus and the mean response rate of the nervous system, by stating Weber's law as  $\Delta\mu = \Delta I/I$ , where  $\mu$  denotes the mean response rate of neurons,  $I$  the stimulus intensity, and  $\Delta$  stands for the difference. However, this logarithmic relation between the input stimulus intensity and the mean output firing rate over simplifies Weber's law. The mean firing rate is considered to be a continuous function of stimulus intensity, and by integrating on both side of the formula yields the logarithmic relation  $\mu = \ln(I)$ . But this continuous function is unable to perform the discrimination task in terms of probability of making the right decision. In other words, this logarithmic relation only considers the mean discharge rate but does not take into account of the variability of the spike train. There lacks of experimental evidence supporting the logarithmic relation of stimulus intensity and mean firing rate.

Even though there are some new psychophysical law emerged (Stevens, 1961) when the expectation of Weber's law is not fulfilled in some experimental methods, Weber's law is still widely accepted and supported by various experiments (Mahns et al., 2006) in psychophysics as a basic law. One argument on this psychophysical law is the 'near-miss Weber's law', describing the observation that Weber's law holds for a majority range of stimulus intensity but

fails in certain range. My theory can explain this observation quite well, as for given population size ( $p$ ) and single neuron firing property ( $CV_{ISI}$ ), the feasible range of the firing rate (or equivalently the stimulus intensity) can be determined under Weber's range.

## **4.5 Final Remarks**

In this chapter, we derived the relation between the mean and standard deviation of the neural signal (firing rate in this case) when Weber's law was satisfied. However, the relations between the first two order statistics of neural signals under different conditions, e.g., sensory discrimination, perceptual judgement, or even motor control, are still under debate in neuroscience. Therefore, we further extended our work into movement control, trying to develop a systematic study on the variability of neural signal and its impact on the precise control of movement in the next chapter.

**Table 4.1.** Parameter region under Weber's Equation.

	Correlation $\rho$	Population size $p$	Firing rate $\lambda$ (Hz)			$CV_{ISI}$
			$CV_{ISI} = 0.5$	$CV_{ISI} = 1$	$CV_{ISI} = 1.5$	
$0.05 \leq k \leq 0.3$		$p = 1$	[25, 2500]	[100, 10 <sup>4</sup> ]	[225, 2·10 <sup>4</sup> ]	$10 \leq \lambda \leq 200$
	$\rho = 0$	<b><math>p = 10</math></b>	<b>[3, 250]</b>	<b>[10, 1000]</b>	<b>[23, 2250]</b>	<b>[0.45, 1]</b>
		$p = 100$	[0.25, 25]	[0, 100]	[2, 500]	[1.4, 3.2]
		$p = 1000$	[0.02, 3]	[0.1, 10]	[0.2, 23]	[4.5, 10]
	$\rho = 0.1$	$p = 10$	[5, 472]	[19, 1900]	[42, 4200]	[0.3, 0.73]
		<b><math>p = 100</math></b>	<b>[3, 270]</b>	<b>[11, 1100]</b>	<b>[25, 2500]</b>	<b>[0.43, 0.95]</b>
		<b><math>p = 1000</math></b>	<b>[3, 250]</b>	<b>[10, 1000]</b>	<b>[23, 2300]</b>	<b>[0.45, 1]</b>

**Table description:**

This table describes the feasible range of the parameter values ( $k$ ,  $\rho$ ,  $p$ ,  $CV_{ISI}$  and  $\mu$  under Weber's

Equation:  $CV_{ISI} = \frac{k}{c(k+2)} \sqrt{\mu \frac{p}{1+(p-1)\rho}}$ . We mainly focus on the range of the firing rate  $\mu$  at given

$CV_{ISI}$  (0.5, 1 and 1.5) and the range of  $CV_{ISI}$  at feasible firing rate ( $10 \leq \mu \leq 200$ ), with the rest parameters fixed. It is concluded that the population size is  $p \leq 11$  for independent superposition process and  $p > 51$  for correlated superposition process, under biological feasible  $CV_{ISI}$  ranging from 0.5 to 1, that the Weber's law is validated. It is illustrated in the bold highlighted region.

## **Chapter 5**

# **A Novel Approach of Precise Movement Control**

In the previous two sections, I have discussed how neurons code sensory stimulus input in terms of neural signal (firing rate) in Chapter 3, and how neural activities are related psychophysical behavior with respect to stimulus intensity (Weber's law) in Chapter 4. In this chapter, I am going to study the effect of neural signal to movement control.

From Chapter 4, I derived from Weber's law that the standard deviation of neural spiking intensity increases linearly with its mean value—the more spikes generated, the more variability of the neural discharge process. In biological systems, the variability and the mean of neural signal may have a positive correlation, but they are not necessarily of a linear relation. In this chapter, I studied the effect of the variability of the neural signal, and found

that in terms of movement control, the less the noise, the more precise the control can be.

## **5.1 Introduction**

The sheer complexity of movement control is often masked by the effortless ease with which we move our body, and only becomes evident when we try to build machines that perform similar tasks as we do. What makes the problem hard is the presence of uncertainty both in the external world, and in our own sensory-motor systems (Harris and Wolpert, 1998; Osborne et al., 2005; Tanaka et al., 2006). Indeed, one of the central issues in Neuroscience is to explain how the nervous system deals so effectively with noise and variability.

The minimum-variance principle proposed by Harris and Wolpert in their seminal work (Harris and Wolpert, 1998), has largely influenced the theoretical studies on the neural basis of motor control. There, the authors argued that the observed characteristics of our movements (e.g. the trajectories and velocity profiles of the eyes during a saccade or of the hand in a reaching task) are the end result of a process whereby the brain seeks to minimize the execution error (variance) caused by noise inherent in the neural control signals. Within such framework, the actual control signals issued by the nervous system would be the (approximately) optimal solutions to related stochastic control problems. In spite of its wide success, this theory still presents some

open issues.

One of its main conclusions is that, assuming that noise in the neural control signals is signal-dependent, and that the objective is to reduce the movement error, the optimal control signals are smooth function of time, as opposed to the degenerate, bang-bang controls that would result if the noise was independent of the signal. In Harris and Wolpert (1998), this result was obtained numerically under the specific assumption that the control signal is a stochastic process with an index of dispersion equal to one ( $\alpha = 1$  in my setting, see Fig. 1 and Model section). Later, an analytical solution was found (Feng and Zhang, 2002; Feng et al., 2004) that generalized this result to a whole range of noise models ( $\alpha \geq 0.5$  in my setting). However, for  $\alpha < 0.5$  the scenario changes radically due to lack of convexity of the related cost functional. In this case, the cost function tends to favor brief pulses of increasingly large amplitude, hence the optimal control signals turn out to be degenerate, i.e. delta functions. It is remarked that any pulse-like form of control which may be taken to approximate the optimal solution in this case, will produce velocity profiles with abrupt acceleration and deceleration phases, which differ markedly from the bell-shaped profiles observed experimentally.

In the light of these results, one may draw the conclusion that large noise is necessary to smooth out our movements. However, in most *in vivo* experiments (including multi-electrode array recordings from our group (Christen et al., 2006; Horton, 2005)) neurons appear to receive and emit spike trains which are at most as variable as Poisson processes, i.e.  $\alpha < 0.5$ . Besides,

one must take into account that *in vivo* recordings are performed in a highly non-stationary environment which could lead to significantly overestimate the irregularity of firing. In conclusion, one is left to wonder whether the noise regime considered in Harris and Wolpert (1998) is relevant.

This is linked to another issue. As illustrated in Fig.5.1A, for  $\alpha \geq 0.5$  the movement error has a positive lower bound, which sets an unsurpassable limit to the precision of the movement. Yet recent experimental evidence (Osborne et al., 2005) has indicated that most of the movement error is due to inaccurate sensory estimates of the external parameters which define the task, so noise in the motor system may not, by itself, limit our ability to move precisely.

All this brings the fundamental question: Is it possible to achieve a precise control with a stochastic signal? As mentioned above, the answer has to be negative for  $\alpha \geq 0.5$ , hence one must look further into the case  $\alpha < 0.5$  to find possible solutions. However, in this case the problem is much harder to tackle because the cost functional of the optimal control task is no longer convex.

Here I will firstly show how to construct suitably defined *generalized* solutions for the optimal control signal when  $0 < \alpha < 0.5$ , inspired by the idea of Young measure theory (Hanson, 2007; Valadier, 1990; Young, 1937; Young, 1942). In terms of these solutions, I will demonstrate that the movement error can be made to approach zero, thus achieving a precise movement control.

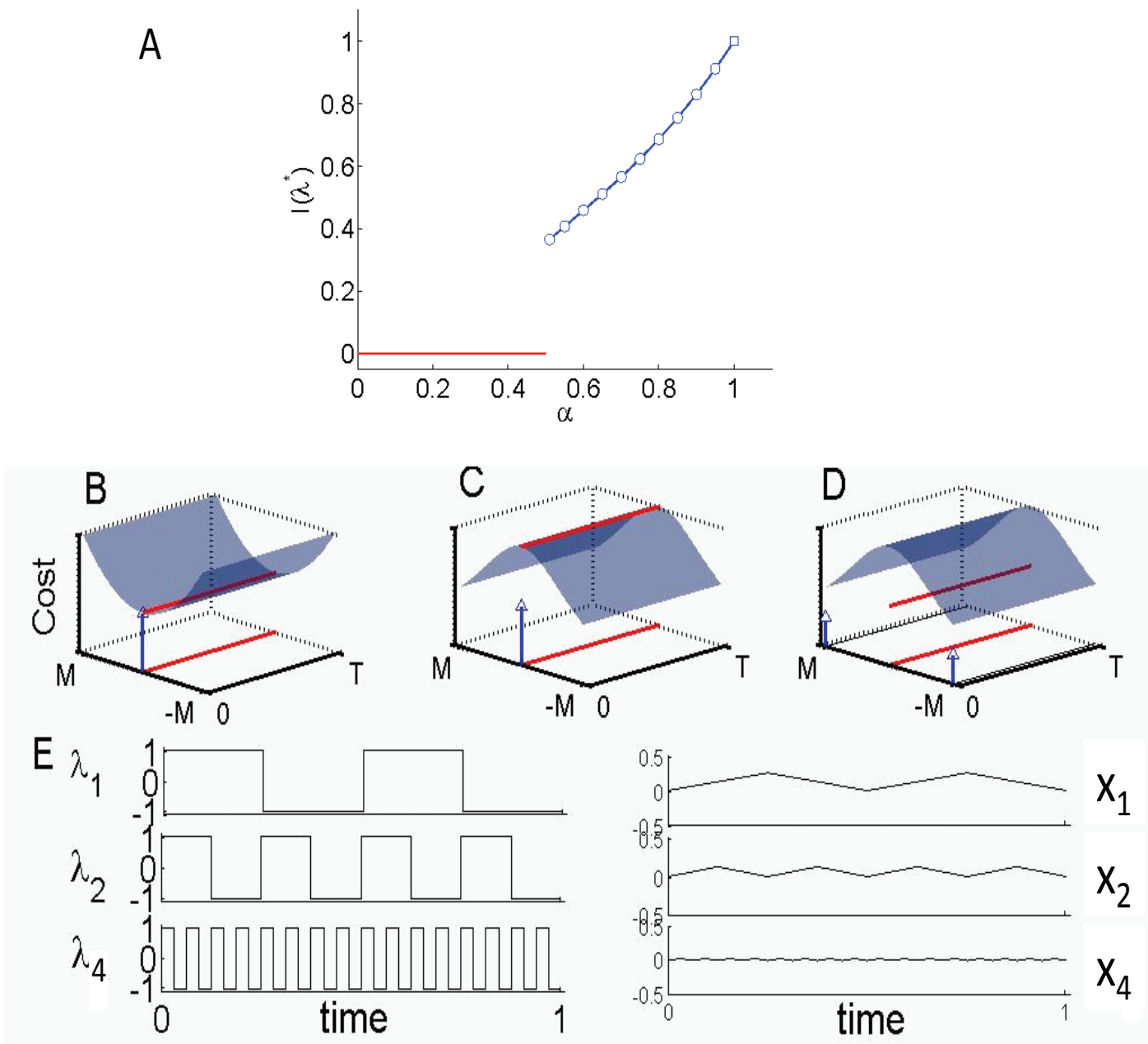


Fig. 5.1 (A) Plotted is the optimal variance  $I(\alpha)$  vs. the noise parameter  $\alpha$ . Results are scaled so that the case of  $\alpha = 1$ , corresponds to unity. (B). A convex cost function allows us to find the minimal solution, corresponding to the case of  $\alpha > 0.5$  in A. (C). For a concave cost function, the minimal points are the boundary, corresponding to the case of  $\alpha < 0.5$  in A. Hence the constraint is usually violated. (D). A proper combination of the boundary solutions (toggling between the boundary) leads to a minimal solution, and satisfies the constraint as well. (E).  $I_0(\lambda)$  for different  $\lambda_1, \lambda_2$  and  $\lambda_4$ . We see that increasing the frequency of toggling will reduce the variance.

## 5.2 Young measure

For an optimization problem, suppose  $I_0 \in \mathbf{R}$  is the objective functional to be optimized on set  $\mathcal{U}$ . The optimization problem is to find  $u \in \mathcal{U}$  such that

$$I_0(u^*) = \inf_{u \in \mathbf{R} \cup \{+\infty\}} I_0(u) \in \mathbf{R}. \quad (5.2.1)$$

If the objective functional  $I_0(u)$  is of the form

$$I_0(u) = \int_{\Omega} F_0(x, u(x), \nabla u(x)) dx,$$

where  $\Omega \subset \mathbf{R}^N$ ,

$$F_0 : \Omega \times \mathbf{R}^m \times \mathbf{M}^{m \times N} \rightarrow \mathbf{R}^*,$$

and the integrand  $F_0$  is convex (Fig. 1B), direct method of the Calculus of Variations is the common technique to solve this kind of questions. However, when there is lack of existence of the classical solutions to the optimization problem (5.2.1), Young measure approach can be applied.

In most of the cases of lack of solutions in optimal control, the essential reason is the oscillatory behavior of minimizing sequences<sup>1</sup> (Pedregal, 1999).

I will demonstrate oscillatory behavior of the control solution by the following

---

<sup>1</sup>The minimizing sequences asymptotically minimize the cost but have no limit in ordinary sense.

example. Consider the functional

$$I_0(\lambda) = \int_0^1 [X(t)^2 + (1 - \lambda(t)^2)] dt,$$

where  $\lambda$  is a measurable function from  $[0, 1]$  to  $[-1, 1]$  and  $X$  satisfies  $dX/dt = \lambda$  with boundary conditions  $X(0) = 0, X(1) = 0$ . There is no admissible  $\lambda^*$  such that  $I(\lambda^*) = \inf I(\lambda)$ . It is clear that the functions  $\lambda_n(t) = \text{sign}[\sin(2^{n+1}\pi t)]$  form a minimizing sequence which asymptotically minimize the cost for  $n \rightarrow \infty$ , but due to the increasingly rapid oscillations, the sequence  $\{\lambda_n\}$  admits no ordinary limit (see Fig. 1E).  $I(\lambda^*) = 0$  is impossible for a single function.

The scenario described above is typical. To deal with the oscillatory behavior of the optimal solutions, Young measure was proposed by L. C. Young (Young, 1937 and 1942) as a tool. The basic idea underlying the Young measure approach is simple: enlarging the class of the competing functions in such a way that, when extended to this new class, the optimization problem always admits a solution. Each competing function  $u(x), x \in \Omega$ , can be regarded as a family of probability measures  $\nu_x = \delta_{u(x)}$  considered as a mapping  $\nu: \Omega \rightarrow \mathcal{M}$  where  $\mathcal{M}$  is huge. Any such mapping  $\nu = \{\nu_x\}_{x \in \Omega}$  is called a *Young measure*. The success of Young measure in the field of optimization is due to the fact that the cost functionals are integrals (Pedregal, 1999). The advantage of this approach is that regardless of whether we have precise information about existence or nonexistence of the optimal solution, we

lose nothing in considering a generalized formulation with the help of Young measure, but we may gain a lot by doing so.

Originally introduced in the context of optimal control problems (Tuckwell, 1984), Young measure have been successfully used in the field of engineering, material science and partial differential equations (Valadier, 1990). So far, Young measure have not yet been used in the field of biology, but it can be a convenient tool to solve some optimization problems in biological systems. The following sections provide examples illustrating the application of Young measure in motor control problems of saccadic eye movement and straight-trajectory arm movement.

### 5.3 Example 1: Saccadic eye movement model

In order to illustrate this ideas, consider a commonly used model of saccadic eye movements (Harris and Wolpert, 1998; Robinson et al., 1986) which is simple enough to obtain analytical results. Let  $x$  denotes the (horizontal) eye displacement from the rest position measured in degrees (eccentricity). Consider saccades from the primary position ( $x(0) = 0$ ) to targets located at a given eccentricity ( $x(T) = D$ ). Assume  $x$  evolves in time according to

$$\ddot{x} = -\frac{1}{\tau_1\tau_2}x - \frac{\tau_1 + \tau_2}{\tau_1\tau_2}\dot{x} + \gamma[\lambda(t) + \xi(t)] \quad (5.3.1)$$

where  $\tau_1, \tau_2, \gamma$  are parameters characteristic of the oculomotor plant. The driving term in brackets models the motor commands, i.e. the output of the motor neurons which innervate the extraocular muscles<sup>2</sup>, and is assumed to be stochastic in nature. Separate a deterministic term  $\lambda(t)$  (which is denoted as the control signal in the following) and a noise part  $\xi(t)$ , which is modelled as a mean zero, gaussian white noise with

$$\mathbb{E}[\xi(t)\xi(t')] = \kappa|\lambda(t)|^{2\alpha}\delta(t - t') \quad (5.3.2)$$

where  $\kappa$  and  $\alpha > 0$  are parameters. Eq.(5.3.2) describes the experimental observation that the variability of neuronal signals *in vivo* tends to increase with the signal strength  $\lambda(t)$ , and generalizes the signal-dependent noise model considered in Harris and Wolpert's (1998), where  $\alpha = 1$ . Remark that the driving term in Eq.(5.3.1) is only a continuous approximation to the actual neural signal, which would be more suitably described as a stochastic point process (Brown et al., 1999; Feng, 2004; Feng and Tuckwell, 2003; Tuckwell, 1984). In particular, for  $\alpha < 0.5$ ,  $\alpha = 0.5$ , or  $\alpha > 0.5$ , the input approximates of a process is less, equally, or more variable than a Poisson process, respectively.

Solving Eq.(5.3.1) we obtain solution  $x(t)$  which is driven by  $\lambda(t)$ , with

---

<sup>2</sup>We assume that force, or torque produced by the muscle is simply proportional to the neural signal. More refined models taking into account the temporal filtering property of the muscles, lead to higher-order systems.

initial conditions  $x(0) = 0, \dot{x}(0) = 0$ :

$$\begin{pmatrix} x(t) \\ \dot{x}(t) \end{pmatrix} = \begin{pmatrix} \gamma \int_0^t b_{12}(t-s)\lambda(s)ds \\ \gamma \int_0^t b_{22}(t-s)\lambda(s)ds \end{pmatrix} + \begin{pmatrix} \gamma \int_0^t b_{12}(t-s)\lambda^\alpha(s)dB(s) \\ \gamma \int_0^t b_{22}(t-s)\lambda^\alpha(s)dB(s) \end{pmatrix},$$

where

$$\begin{cases} b_{12}(t) = \frac{\tau_1\tau_2}{\tau_2 - \tau_1} \left[ \exp\left(-\frac{t}{\tau_2}\right) - \exp\left(-\frac{t}{\tau_1}\right) \right] \\ b_{22}(t) = \frac{\tau_1\tau_2}{\tau_2 - \tau_1} \left[ \frac{1}{\tau_1} \exp\left(-\frac{t}{\tau_1}\right) - \frac{1}{\tau_2} \exp\left(-\frac{t}{\tau_2}\right) \right]. \end{cases}$$

and  $B(t)$  stands for the standard Brownian motion.

The optimal control problem is then defined as follows: For a target position  $D$ , and time  $T, R > 0$ , find a control signal  $\lambda^*(t)$  such that

$$\mathbb{E}[x(t)] = D, \text{ for } t \in [T, T + R] \quad (5.3.3)$$

and

$$\begin{aligned} I(\lambda^*) &= \min_{\lambda \in \mathcal{L}^{2\alpha}[0, T+R]} I(\lambda) \\ &= \min_{\lambda \in \mathcal{L}^{2\alpha}[0, T+R]} \int_T^{T+R} \text{Var}[x(t)] dt. \end{aligned} \quad (5.3.4)$$

The physical meaning of the problem is clear: at time  $T$ , the eye must be on average on the target (Eq.(5.3.3)), and as precisely as possible (Eq.(5.3.4)). Also, the requirement that the average eye position is a constant in the post-

movement period  $t \in [T, T + R]$  implies that the average velocity must be zero on the target.

Note that

$$\int_T^{T+R} \text{Var}(x(t)) dt \quad (5.3.5)$$

$$= \gamma^2 \left\langle \int_T^{T+R} \left[ \int_0^t b_{12}(t-s) \lambda(s)^\alpha \cdot dB(s) \right]^2 dt \right\rangle \quad (5.3.6)$$

$$= \gamma^2 \int_T^{T+R} \left[ \int_0^t b_{12}^2(t-s) |\lambda(s)|^{2\alpha} ds \right] dt, \quad (5.3.7)$$

then the original control problem defined by Eq.(5.3.3) and (5.3.4) is reduced to the following optimization problem: Find  $\lambda^*(s) \in \mathcal{L}^{2\alpha}[0, T + R]$  which minimizes

$$I(\lambda) = \int_T^{T+R} \left[ \int_0^t b_{12}^2(t-s) |\lambda(s)|^{2\alpha} ds \right] dt \quad (5.3.8)$$

subject to the constraint

$$\int_0^t b_{12}(t-s) \lambda(s) ds = \frac{D}{\gamma}, \text{ for } t \in [T, T + R]. \quad (5.3.9)$$

Rewrite the above objective functional  $I(\lambda)$  and express it by during-movement ( $I_1(\lambda)$ ) and post-movement ( $I_2(\lambda)$ ) functionals:

$$I(\lambda) = I_1(\lambda) + I_2(\lambda),$$

where

$$\begin{aligned} I_1(\lambda) &= \int_0^T \left[ \int_T^{T+R} b_{12}^2(t-s) dt \right] |\lambda(s)|^{2\alpha} ds \\ I_2(\lambda) &= \int_T^{T+R} \left[ \int_T^s b_{12}^2(t-s) dt \right] |\lambda(s)|^{2\alpha} ds. \end{aligned} \quad (5.3.10)$$

When  $2\alpha > 1$ , the objective functional  $I(\lambda)$  is convex, and this optimal control problem can be solved theoretically with the method Calculus of Variation. The detailed technique and solution is presented as follows.

### 5.3.1 Ordinary solution when $\alpha > 0.5$

**Post-movement solution in  $t \in [T, T + R]$**

The optimal post-movement solution  $\lambda^*$  for  $t \in [T, T + R]$  of the objective functional  $I_2(\lambda^*)$  is determined by the constraint (5.3.9) and its derivative directly. By differentiating Eq.(5.3.9) (since  $R > 0$ ), we obtain

$$\begin{aligned} -\frac{1}{\tau_2} \exp\left(-\frac{t}{\tau_2}\right) \int_0^t \exp\left(\frac{s}{\tau_2}\right) \lambda(s) ds + \frac{1}{\tau_1} \exp\left(-\frac{t}{\tau_1}\right) \\ \cdot \int_0^t \exp\left(\frac{s}{\tau_1}\right) \lambda(s) ds = 0 \end{aligned} \quad (5.3.11)$$

for  $t \in [T, T + R]$ . Solving Eq.(5.3.9) and Eq.(5.3.11) we see that

$$\begin{cases} \int_0^t \exp\left(\frac{s}{\tau_2}\right) \lambda(s) ds = \frac{D}{\tau_1 \gamma} \exp\left(\frac{t}{\tau_2}\right) \\ \int_0^t \exp\left(\frac{s}{\tau_1}\right) \lambda(s) ds = \frac{D}{\tau_2 \gamma} \exp\left(\frac{t}{\tau_1}\right) \end{cases} \quad (5.3.12)$$

for  $t \in [T, T + R]$ . This implies

$$\lambda^*(t) = \frac{D}{\tau_1 \tau_2 \gamma}, \quad \forall t \in [T, T + R]$$

and in particular

$$\begin{cases} \int_0^T \exp\left(\frac{s}{\tau_2}\right) \lambda(s) ds = \frac{D}{\tau_1 \gamma} \exp\left(\frac{T}{\tau_2}\right) \\ \int_0^T \exp\left(\frac{s}{\tau_1}\right) \lambda(s) ds = \frac{D}{\tau_2 \gamma} \exp\left(\frac{T}{\tau_1}\right). \end{cases} \quad (5.3.13)$$

**During-movement solution in  $t \in [0, T]$**

To find the optimal signal  $\lambda^*(t)$  in  $t \in [0, T]$  for the objective functional  $I_1(\lambda)$  during saccadic eye movement, we apply the calculus of variations method in (5.3.10). To this end, let us define

$$\left\{ \lambda, \int_0^T b_{12}(T-s)\lambda(s) ds = \frac{D}{\gamma}, \lambda(t) = \frac{D}{\tau_1 \tau_2 \gamma}, t \in [T, T + R] \right\} = \mathcal{U}_D. \quad (5.3.14)$$

For a small  $\tau$ , consider  $\lambda + \tau\phi \in \mathcal{U}_D$ , i.e.

$$\begin{aligned} \phi &\in \left\{ \phi, \int_0^T \exp\left(\frac{s}{\tau_1}\right) \phi(s) ds = 0, \int_0^T \exp\left(\frac{s}{\tau_2}\right) \phi(s) ds = 0, \phi(t) = 0, t \in [T, T + R] \right\} \\ &= \mathcal{U}_D^0. \end{aligned} \quad (5.3.15)$$

The first two constraints in  $\mathcal{U}_D^0$  are from Eq. (5.3.13). We then have

$$\left. \frac{dI_1(\lambda + \tau\phi)}{d\tau} \right|_{\tau=0} = 0,$$

which gives

$$\int_0^T \left\{ \left[ \int_T^{T+R} b_{12}^2(t-s) dt \right] |\lambda(s)|^{2\alpha-1} \text{sgn}(\lambda(s)) \phi(s) \right\} ds = 0. \quad (5.3.16)$$

Comparing Eq. (5.3.16) with the first two constraints in  $\mathcal{U}_D^0$ , we conclude that

$$\left[ \int_T^{T+R} b_{12}^2(t-s) dt \right] |\lambda(s)|^{2\alpha-1} \text{sgn}(\lambda(s)) = A(\xi, \eta) \quad (5.3.17)$$

almost surely for  $s \in [0, T]$  and  $A(\xi, \eta)$  with two parameters  $\xi, \eta \in \mathbb{R}$  is of the form

$$A(\xi, \eta) = \xi \exp\left(\frac{t}{\tau_1}\right) + \eta \exp\left(\frac{t}{\tau_2}\right), \quad (5.3.18)$$

being the solution of the following equations

$$\left\{ \begin{array}{l} \frac{D}{\tau_1 \gamma} \exp\left(\frac{T}{\tau_2}\right) = \int_0^T \exp\left(\frac{s}{\tau_2}\right) \cdot |A(\xi, \eta)|^{\frac{1}{2\alpha-1}} \\ \quad \cdot \text{sgn}[A(\xi, \eta)] \left( \int_T^{T+R} b_{12}^2(t-s) dt \right)^{-\frac{1}{2\alpha-1}} ds \\ \frac{D}{\tau_2 \gamma} \exp\left(\frac{T}{\tau_1}\right) = \int_0^T \exp\left(\frac{s}{\tau_1}\right) \cdot |A(\xi, \eta)|^{\frac{1}{2\alpha-1}} \\ \quad \cdot \text{sgn}[A(\xi, \eta)] \left( \int_T^{T+R} b_{12}^2(t-s) dt \right)^{-\frac{1}{2\alpha-1}} ds. \end{array} \right.$$

Therefore, for  $\alpha > 0.5$  we obtain

$$\lambda^*(t) = |A(\xi, \eta)|^{\frac{1}{2\alpha-1}} \text{sgn}[A(\xi, \eta)] \cdot \left( \int_T^{T+R} b_{12}^2(s-t) ds \right)^{-\frac{1}{2\alpha-1}} \quad (5.3.19)$$

for  $t \in [0, T]$ . Also, for the post-movement period  $t \in (T, T+R]$  the optimal

solution is simply given by the hold-on control  $\lambda^* = D/(\tau_1\tau_2\gamma)$ , as derived earlier. When  $\alpha = 0.5$ , the solution is harder to find analytically, but similar conclusions hold. Hence, for  $\alpha \geq 0.5$ , a minimizer  $\lambda^*$  is guaranteed to exist and to be unique by the convexity of the cost functional and the set of admissible controls. Finally one can easily verify that  $I(\lambda^*) > 0$ .

For  $0 < \alpha < 0.5$  the cost functional is concave, therefore according to Young measure theory, a solution, if exists, must be found among the extreme points of the set of admissible control  $\Omega = \{\lambda \in \mathcal{L} : \text{the constraint is verified}\}$  (Fig. 1C-D). This means that any solution must be a superposition of delta functions. For instance, one can easily verify that, for  $t \in [0, T]$ , all controls of the form  $\lambda(t) = \sum_i A_i \delta(t - t_i)$  with  $t_i \in [0, T]$  and suitable choice of the constants  $A_i$ , will drive the system on the target with absolute precision, i.e. they bear a vanishing contribution to the error<sup>3</sup>. It can be concluded that for  $0 < \alpha < 0.5$ , the optimal control is degenerate and not unique, with  $I(\lambda^*) = 0$ .

In Fig. 1A is the minimum movement error,  $I(\lambda^*)$ , as a function of  $\alpha$ . The meaning of this result is clear. For  $\alpha \geq 0.5$  there is a lower bound to the movement error. In other words, although there exists an implementable and finite signal which minimizes the error, the end result will be degraded by higher noise levels in the system, consistent with our intuition. By contrast, for  $0 < \alpha < 0.5$  the minimum error is zero, although there is no finite control

---

<sup>3</sup>For  $t > T$ , one could consider solutions of the form  $\int_T^{T+R} \delta(t - t') A(t') dt'$

signal that can achieve it. The question to be addressed in the next section is whether- and most importantly how- such minimum can be approached.

### 5.3.2 Generalized control when $\alpha < 0.5$

Based on the previous discussion, for  $\alpha < 0.5$  we can achieve an arbitrary degree of precision, although the optimal control  $\lambda^*$  which would reduce the error to zero is not implementable. Obviously, if we could find a sequence of finite controls  $\{\lambda_M^*\}$  satisfying

$$\lim_{M \rightarrow \infty} I(\lambda_M^*) = 0, \quad (5.3.20)$$

we could use these as a replacement for  $\lambda^*$  and improve the accuracy as we wished. For instance, one may consider selecting  $\lambda_M^*$  among the minimizers of  $I$  in the space of bounded controls

$$\Omega_M = \Omega \wedge \{f \in \mathcal{L}^{2\alpha}[0, T + R], |f| \leq M\}.$$

Unfortunately this approach is not directly feasible in practice. Indeed, when the cost functional is not convex, there is no guarantee that the minimizers  $\lambda_M^*$  exist among ordinary functions.

From the previous discussion on Young measure in section 2, we can construct a generalized control for this nonconvex optimization problem. Particularly, this generalized control is a one-parameter family of probability distri-

butions over the control domain indexed by time, i.e.  $\tilde{\nu} = \{\tilde{\nu}_t\}_{t \in I}$ . In other words, while an ordinary control is a mapping which assigns to each time a precise value to the driving signal, a generalized control provides at each time a probability distribution over all the allowed control values. One sees that ordinary controls map naturally onto (or can be identified with) a subset of generalized controls<sup>4</sup>, hence the latter provides an extension of the former in some sense.

Let us see how our control problem can be reformulated here. For convenience of notation, we will represent this generalized control  $\tilde{\nu}$  by a stochastic process  $\nu(t)$  such that  $P(\nu(t) \in A) = \tilde{\nu}_t(A)$  for any subset  $A \in [0, T]$ <sup>5</sup>. Then, for a generalized control  $\tilde{\nu}$  we define the functional

$$\tilde{I}(\tilde{\nu}) \doteq EI(\nu) = \begin{cases} \int_0^T \left[ \int_0^{T+R} b_{12}^2(t-s) dt \right] E(|\nu(s)|^{2\alpha}) ds & s \in [0, T] \\ \int_T^{T+R} \left[ \int_T^s b_{12}^2(t-s) dt \right] E(|\nu(s)|^{2\alpha}) ds & s \in [T, T+R], \end{cases}$$

where  $E(\cdot)$  denotes the expectation with respect to the measure of the process  $\nu(t)$ . Finally, the constraints on the admissible generalized control are

<sup>4</sup>Every ordinary control  $\lambda$  can be identified with its associated generalized control  $\tilde{\lambda}_t = \delta_{\lambda(t)}$  where  $\delta$  stands for the Dirac mass.

<sup>5</sup>However, we remark that the stochastic process  $\nu$  here is only a formal ‘handle’ to the underlying generalized control, and that strictly speaking, there are no ‘realizations’ of  $\tilde{\nu}$ , since the latter does not take values in  $U$ .

obtained in a similar fashion, i.e.

$$\begin{cases} \int_0^t \exp\left(\frac{s}{\tau_2}\right) E(\nu(s)) ds = \frac{D}{\tau_1 \gamma} \exp\left(\frac{t}{\tau_2}\right) \\ \int_0^t \exp\left(\frac{s}{\tau_1}\right) E(\nu(s)) ds = \frac{D}{\tau_2 \gamma} \exp\left(\frac{t}{\tau_1}\right) \end{cases} \quad (5.3.21)$$

for  $t \in [T, T + R]$ .

We are now in a position to reconsider our original problem in its generalized formulation. Starting from any ordinary control, we can thus consider all the generalized controls whose average correspond to it. In particular, when the cost functional is concave, any generalized control which is not exclusively concentrated on the signal, will bring a lower generalized cost, and the cost will be minimum for those measures which are concentrated on the extreme control values, say  $\{0, M\}$ . Thus, for any ordinary controls which obeys our problem constraints, we obtain a corresponding 'optimal' generalized control in the form

$$\tilde{\nu}_t = (1 - \beta(t))\delta_0 + \beta(t)\delta_M,$$

with  $\beta(t) \in [0, 1]$  and  $\delta$  as the delta function.

By this we proved that it is relatively easy in our case to find good, albeit perhaps not optimal, generalized solutions. These class of solutions are now defined in terms of a simple function,  $\beta(t)$  and may be identified with a stochastic processes toggling between two values, i.e.  $\nu$  such that  $\nu(t) \in \{0, M\}$ , with  $P(\nu(t) = M) = \beta(t)$ .

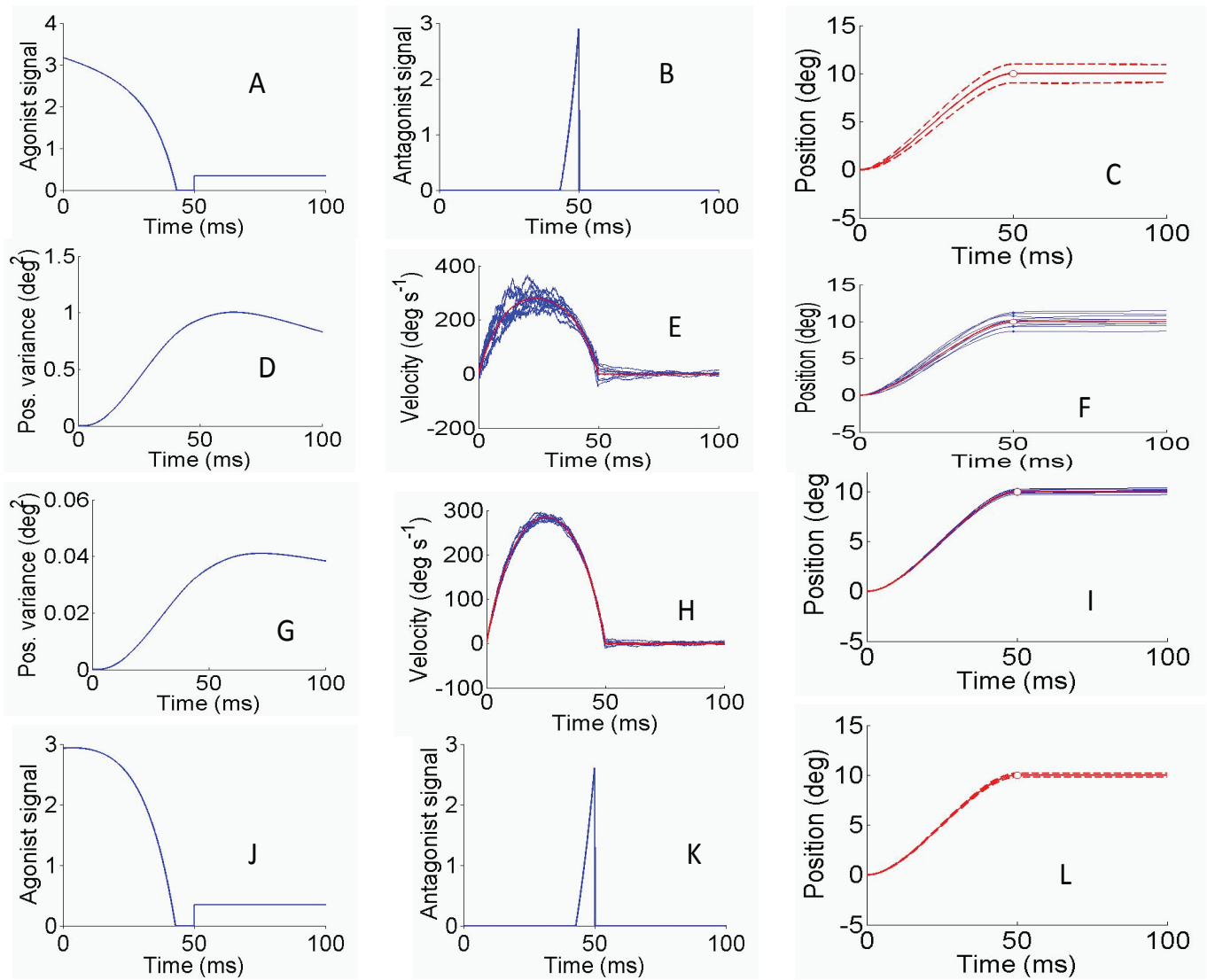


**Fig. 5.2** Simulation results for saccadic eye movement model. *A, B, C, D, E, F* are the case for  $\alpha = 1$  and *G, H, I, J, K, L* are the case for  $\alpha = 0.25$ . *E, F, H, I* are sample velocities and sample paths. Red curves are the mean. *C, L* are the mean and standard deviations.

**Generalized post-movement solution in  $t \in [T, T + R]$** 

To minimize the post-movement objective functional  $I_2(\lambda)$  with constraint (5.3.9) for  $t \in [T, T + R]$ , we restrict ourselves to consider generalized controls which are concentrated on extreme values only. To this end, consider the stochastic process  $\nu(t)$ ,  $t \in [T, T + R]$ , where  $\nu(t) \in \{0, M\}$  and  $P(\nu(t) = M) = \beta(t) \in [0, 1]$ . Let us see the implications of our construction:

$$\begin{aligned} EI_2(\nu) &= \int_T^{T+R} \left[ \int_T^s b_{12}^2(t-s) dt \right] E[|\nu(s)|^{2\alpha}] ds \\ &= \int_T^{T+R} \left[ \int_T^s b_{12}^2(t-s) dt \right] M^{2\alpha} \beta(s) ds \end{aligned}$$

with the constraints

$$\left\{ \begin{array}{l} \int_0^t \exp\left(\frac{s}{\tau_2}\right) E[\nu(s)] ds = \int_0^t \exp\left(\frac{s}{\tau_2}\right) M\beta(s) ds \\ \qquad \qquad \qquad = \frac{D}{\tau_1\gamma} \exp\left(\frac{t}{\tau_2}\right) \\ \int_0^t \exp\left(\frac{s}{\tau_1}\right) E[\nu(s)] ds = \int_0^t \exp\left(\frac{s}{\tau_1}\right) M\beta(s) ds \\ \qquad \qquad \qquad = \frac{D}{\tau_2\gamma} \exp\left(\frac{t}{\tau_1}\right) \end{array} \right. \quad (5.3.22)$$

for  $t \in [T, T + R]$ . The constraints equations above imply that  $\beta(s)$  is a constant measure, independent of  $s$  and

$$\beta(s) = \frac{D}{M\tau_1\tau_2\gamma}$$

for  $s \in [T, T + R]$  and  $M \gg 1$ .

To further explore the advantages of our approach here, let us estimate the

term  $EI_2(\nu)$  in more details. Summarizing results above we have

$$EI_2(\nu) = C_2(T, R) \cdot \frac{D}{M^{1-2\alpha}\tau_1\tau_2\gamma}$$

where

$$C_2(T, R) = \int_T^{T+R} \left[ \int_T^s b_{12}^2(t-s) dt \right] ds$$

is a constant depending on  $T$  and  $R$ . Therefore the variance goes to zero as  $M$  goes to infinity at a rate of  $1/M^{1-2\alpha}$  for  $\alpha < 1/2$ . In other words, the smaller the  $\alpha$  is (the less noisy the system is), the faster the variance approaches zero.

Numerically, the generalized control solution  $\lambda_M^*(t)$  for  $t \in [T, T+R]$  can be constructed in the following way. For a given time step  $h$  and  $t+(k+1)h \leq T+R$ ,  $k = 0, 1, 2, \dots$ , we define

$$\lambda_M^*(t) = \begin{cases} M & \text{if } 0 \leq t - T - kh < h * \beta(T + kh) \\ 0 & \text{if } h * \beta(T + kh) \leq t - T - kh < h \end{cases} \quad (5.3.23)$$

Therefore,  $\lambda_M^*(t)$  is a pulse function of width  $\beta(t)$ . Obviously, when  $h \rightarrow 0$ ,  $\lambda_M^*(t) \sim \nu(t)$  for  $t \in [T, T+R]$ .

### Generalized during-movement solution in $t \in [0, T]$

The same idea can be applied to finding the generalized solution in  $[0, T]$  as well. The problem we consider here is to minimize the objective functional during movement  $I_1(\lambda^*)$  with constraints (5.3.9) for  $\lambda \in \mathcal{L}^{2\alpha}[0, T+R] \wedge$

$[-M, M]$ . It is easily seen that  $\nu(t)$  should be a random process taking values in  $\{-M, 0, M\}$ . To simplify the issue further, we only consider a stochastic process  $\nu(t)$  taking two values alternatively. Denote  $E = \{t, \nu(t) \geq 0\}$  and define  $P(\nu(t) = M) = w(t)$  for  $t \in E$ . For  $t \in [0, T] - E$ , we have  $P(\nu(t) = -M) = w(t)$ . Hence the process  $\nu(t)$  is uniquely defined by a one-dimensional function  $w(t)$ .

Define  $\beta(t) = [w(t)I_E - w(t)I_{[0, T] - E}]$ , the optimal problem becomes to find  $w(t)$  to minimize

$$I_1 = \int_0^T \left[ \int_T^{T+R} b_{12}^2(t-s) dt \right] M^{2\alpha} |\beta(s)| ds \quad (5.3.24)$$

with constraints

$$\begin{cases} \int_0^T \exp\left(\frac{s}{\tau_2}\right) \beta(s) ds = \frac{D}{M\tau_1\gamma} \exp\left(\frac{T}{\tau_2}\right) \\ \int_0^T \exp\left(\frac{s}{\tau_1}\right) \beta(s) ds = \frac{D}{M\tau_2\gamma} \exp\left(\frac{T}{\tau_1}\right) \end{cases} \quad (5.3.25)$$

for  $|\beta(t)| \leq 1$ .

To obtain the generalized control signal which asymptotically approaches the global minimum, we define

$$\beta(t) = \frac{\xi_1}{\tau_1} \exp\left(\frac{t-T}{\tau_1}\right) + \frac{\xi_2}{\tau_2} \exp\left(\frac{t-T}{\tau_2}\right),$$

where  $\xi_1, \xi_2$  are two constants to be determined later. For simplicity, let us further define  $\omega_i(t) = \frac{1}{\tau_i} \left[ \exp\left(\frac{t-T}{\tau_i}\right) \right]$  for  $i = 1, 2$ . The definitions above and

the constraints yield

$$\begin{cases} \|\omega_1\|^2 \xi_1 + \langle \omega_1, \omega_2 \rangle \xi_2 = \frac{D}{M\tau_1\tau_2\gamma} \\ \langle \omega_1, \omega_2 \rangle \xi_1 + \|\omega_2\|^2 \xi_2 = \frac{D}{M\tau_1\tau_2\gamma}, \end{cases} \quad (5.3.26)$$

where  $\langle \omega_1, \omega_2 \rangle = \int_0^T \omega_1(s)\omega_2(s)ds$ . Therefore

$$\begin{pmatrix} \xi_1 \\ \xi_2 \end{pmatrix} = \frac{1}{\|\omega_1\|^2\|\omega_2\|^2 - (\langle \omega_1, \omega_2 \rangle)^2} \begin{pmatrix} \|\omega_2\|^2 & -\langle \omega_1, \omega_2 \rangle \\ -\langle \omega_1, \omega_2 \rangle & \|\omega_1\|^2 \end{pmatrix} \cdot \begin{pmatrix} \frac{D}{M\tau_1\tau_2\gamma} \\ \frac{D}{M\tau_1\tau_2\gamma} \end{pmatrix}.$$

Summarize the result we have

$$EI_1(\nu) = C_1(T, R) \cdot \frac{D}{M^{1-2\alpha}\tau_1\tau_2\gamma}$$

where

$$C_1(T, R) = \int_T^{T+R} \left[ \int_T^s b_{12}^2(t-s)dt \right] W(s)ds$$

is a constant depending on  $T$  and  $R$ , and

$$W(t) = \frac{\omega_1\|\omega_2\|^2 + \omega_2\|\omega_1\|^2 - \langle \omega_1, \omega_2 \rangle \cdot (\omega_1 + \omega_2)}{\|\omega_1\|^2\|\omega_2\|^2 - (\langle \omega_1, \omega_2 \rangle)^2}$$

It can be easily shown that  $EI_1$  converges to zero with a rate of  $1/M^{1-2\alpha}$ , similar to  $EI_2$ .

Numerically,  $\lambda_M^*$  for  $t \in [0, T]$  can be exactly constructed as  $\lambda_M^*$  for  $t \in [T, T+R]$  with the width of being  $M$  or  $-M$  depending on  $t$ . More precisely,

for a given time step  $h$  and  $t + (k + 1)h \leq T, k = 0, 1, 2, \dots$ , we define

$$\lambda_M^*(t) = \begin{cases} \text{sign}(\beta(kh)) \cdot M & \text{if } 0 \leq t - kh < h * |\beta(kh)| \\ 0 & \text{if } h * |\beta(kh)| \leq t - kh < h \end{cases} \quad (5.3.27)$$

### 5.3.3 Numerical simulations

In Fig. 5.2, we plot two cases of  $\alpha = 1$  (A,B,C,D,E,F) and  $\alpha = 0.25$  with  $M = 500$  (G,H,I,J,K,L). It is clearly shown that when  $M = 500, \alpha = 0.25$ , the control accuracy is improved considerably, in comparison with the case of  $\alpha = 1$ . This numerical simulation is in agreement with our theoretical results derived above. The parameters used are  $\tau_1 = 224$  ms  $\tau_2 = 13$  ms,  $T = 50$  ms,  $R = 50$  ms,  $D = 10$  degree,  $\gamma = 1e - 2, \kappa = 0.58$ , exactly the same set of parameters as in Harris and Wolpert's (1998). It is interesting to compare Fig. 2D with Fig. 2G, for example. With our approach, the accuracy is improved by 25 times!

## 5.4 Example 2: Straight-trajectory arm movement control

Another optimization problem related to biological signal control is the arm movement. This model is relative more complicated than the saccadic eye movement model owing to its multi-variables and nonlinearity. This sensorimotor transformations are often formalized in terms of coordinate trans-

formations. The nonlinearity arises from the geometry of our joints. The change in spatial location of the hand that results from bending the elbow depends not only on the amplitude of the elbow movement, but also on the state of the shoulder joint.

For simplicity, I ignore the gravity and viscous forces, and only consider the movement of hand on a horizontal plane in the absence of friction. Let  $\theta_1$  denote the angle between the upper arm and horizontal direction, and  $\theta_2$  the angle between the forearm and upper arm (Fig. 5.3A). When reaching between two points, humans move their arms to make the path of the hand between the two points roughly straight. These straight movements are smooth: the acceleration profile of the movement contains no discontinuities. This results in a characteristic bell-shaped velocity profile for the movement.

The straight-trajectory hand movement can be defined as follows. Let  $H_0 = (x_H(0), y_H(0))$  be the initial position of hand at time  $t = 0$ , and  $H_1 = (x_H(T), y_H(T))$  the target position of hand (Fig. 5.3B).  $T$  is the total duration of movement,  $d$  is the distance between  $H_0$  and  $H_1$ , and the straight hand trajectory can be expressed by

$$\begin{cases} x_H(t) = x_H(0) + d \cdot \phi_n\left(\frac{t}{T}\right) \cdot \cos \varphi \\ y_H(t) = y_H(0) + d \cdot \phi_n\left(\frac{t}{T}\right) \cdot \sin \varphi, \end{cases}$$

where  $\varphi$  is the angle between the vector  $\overrightarrow{H_0H_1}$  and the  $x$ -axis, and  $\phi_n$  is the

one-parameter family of functions

$$\phi_n(z) = z^n - \frac{1}{2\pi} \sin(2\pi z^n). \quad (5.4.1)$$

For  $n = 1$ , the velocity profile is bell-shaped and symmetric; for  $n > 1$ , the velocity is shifted towards the end, for  $n < 1$  towards the start.

From the expression above we have the hand start from  $H_0$  at time  $t = 0$  and reach  $H_1$  at time  $t = T$ . The trajectory is straight, and the distance from  $H_0$  increases monotonically. Also, the tangential hand velocity and accelerations are zero for both  $t = 0$  and  $t = T$ . The corresponding joint angles can be obtained from the following equations (see Fig. 5.3)

$$\begin{cases} \theta_1(t) = \tan^{-1} \left( \frac{y(t)}{x(t)} \right) - \tan^{-1} \left( \frac{l_2 \sin \theta_2(t)}{l_1 + l_2 \cos \theta_2(t)} \right) \\ \theta_2(t) = \cos^{-1} \left( \frac{x^2(t) + y^2(t) - l_1^2 - l_2^2}{2l_1 l_2} \right). \end{cases} \quad (5.4.2)$$

Furthermore, the whole arm movement dynamic system satisfies the Euler-Lagrange equation, which can be expressed by the following non-linear system of differential equation

$$M(\theta_1, \theta_2) \begin{pmatrix} \ddot{\theta}_1 \\ \ddot{\theta}_2 \end{pmatrix} + C(\theta_1, \theta_2, \dot{\theta}_1, \dot{\theta}_2) \begin{pmatrix} \dot{\theta}_1 \\ \dot{\theta}_2 \end{pmatrix} = \gamma_0 \begin{pmatrix} Q_1 \\ Q_2 \end{pmatrix} \quad (5.4.3)$$

where  $\gamma_0$  is the scale parameter,  $M$  and  $C$  are  $\theta$ -dependent matrices<sup>6</sup>, and  $Q_i$

<sup>6</sup> $M$  is the mass matrix of the form  $M = \begin{pmatrix} I_1 + m_1 r_1^2 + m_2 l_1^2 + I_2 + m_2 r_2^2 + 2k \cos \theta_2 & I_2 + m_2 r_2^2 + k \cos \theta_2 \\ I_2 + m_2 r_2^2 + k \cos \theta_2 & I_2 + m_2 r_2^2 \end{pmatrix}$

are the external forces (torques) applied to the joints of arm,  $i = 1, 2$ . We use the minimum variance model for this optimal control task (optimization in the presence of signal-dependence noise), which has more advantages over other optimization based models for the control of a robot arm (Simmons and Demiris, 2005). We regard the torques  $Q_i = \lambda_i(t) + \xi_i(t)$  as the motor commands, which is assumed to be stochastic in nature. We separate the motor command signal into a deterministic term  $\lambda_i(t)$  and a noise term  $\xi_i(t)$ , which is modelled as a mean zero, gaussian white noise with

$$E[\xi_i(t)\xi_i(t')] = \kappa_0|\lambda_i(t)|^{2\alpha}\delta(t - t'),$$

where  $\kappa_0$  and  $\alpha > 0$  are parameters.

We define our objective functional as the minimal end-point error

$$I = \min_{\lambda_1, \lambda_2 \in \mathcal{L}^{2\alpha}[0, T]} \sqrt{\sigma_1^2 + \sigma_2^2},$$

where  $\sigma_1$  and  $\sigma_2$  are the eigenvalues of the covariance matrix of the final hand position  $H_1 = (x_H(T), y_H(T))$  for  $t = T$ .

It is not possible to find a theoretical solution to this problem. However, numerical simulation demonstrates the advantage of Young measure control signal with less noise ( $\alpha < 0.5$ ) compared with ordinary control when more

and  $C = k \sin \theta_2 \begin{pmatrix} \dot{\theta}_2 & \dot{\theta}_1 + \dot{\theta}_2 \\ \dot{\theta}_1 & 0 \end{pmatrix}$ , with  $m_i, l_i, I_i, i = 1, 2$  being the mass, the length and the moment of inertia with respect to the center of mass for the  $i$ -th link,  $k = m_2 l_1 r_2$ .  $i = 1$  denotes the upper arm,  $i = 2$  the forearm (see Fig. 3A).

noise ( $\alpha \geq 0.5$ ) are presented.

## Numerical simulation

We obtain the control signals  $\lambda_1$  and  $\lambda_2$ , which are the torques  $Q_1$  and  $Q_2$  to be applied to the joints to move the hand along the prescribed from the trajectory  $(x(t), y(t))$ , by numerically estimate the first and second order derivatives of the angle  $(\theta_1, \theta_2)$  from Eq.( 5.4.2). After corrupting the control signal  $(\lambda_1(t), \lambda_2(t))$  with the corresponding noises, we generate a set of trajectories by solving the system (5.4.3). We only show the simulation for the symmetric velocity profile (with skewness index  $n = 1$ ), but similar results are obtained for right-shift ( $n > 1$ ) or left-shift ( $n < 1$ ) arm-movement velocity.

Fig. 5.4A shows the case for  $\alpha = 1$  with end of point error 0.07 m, while Fig.4B is the case when  $\alpha = 0.25$ , and the end of point error equals 0.01 m with the large Young measure value  $M$ . To increase the value of  $M$ , more accurate control can be achieved. 10 trials of the simulation results are shown for each case. The parameters used in the simulation are:  $m_1 = 2.28$  kg,  $m_2 = 1.31$  kg,  $l_1 = 0.305$  m,  $l_2 = 0.254$  m,  $I_1 = 0.022kg \cdot m^2$ ,  $I_2 = 0.0077kg \cdot m^2$ ,  $r_1 = 0.133$  m,  $r_2 = 0.109$  m,  $T = 650$  ms,  $dt = 0.01$  ms,  $\varphi = 3\pi/4$ . These parameter values are consistent with morphological data (Simmons and Demiris, 2005).

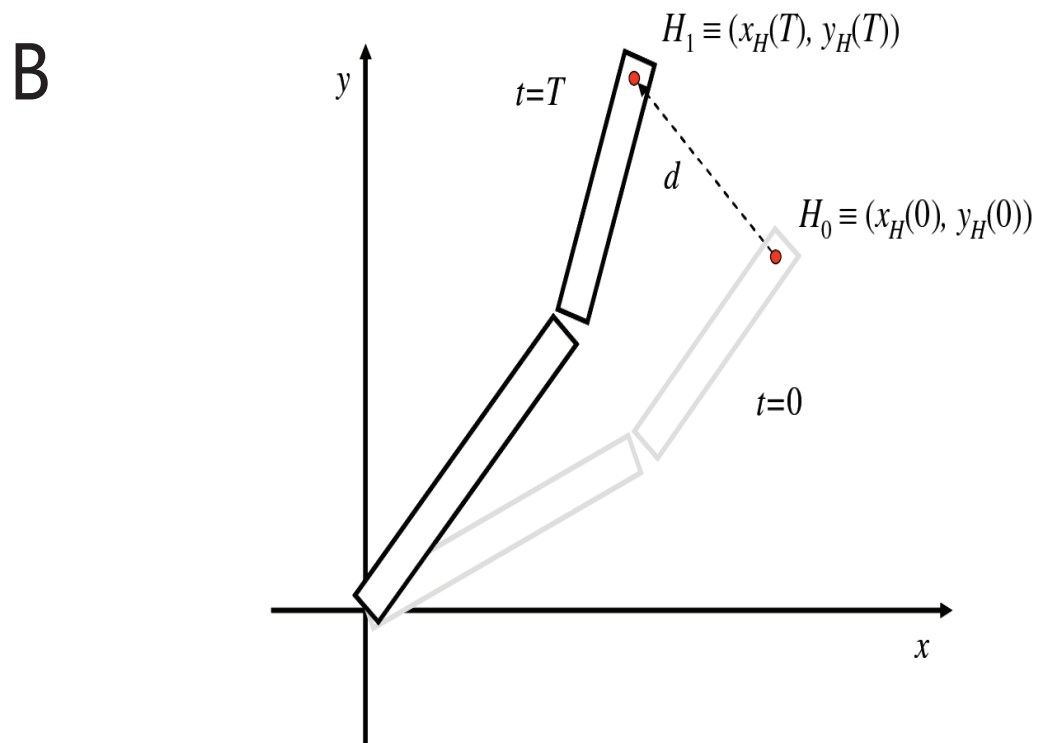
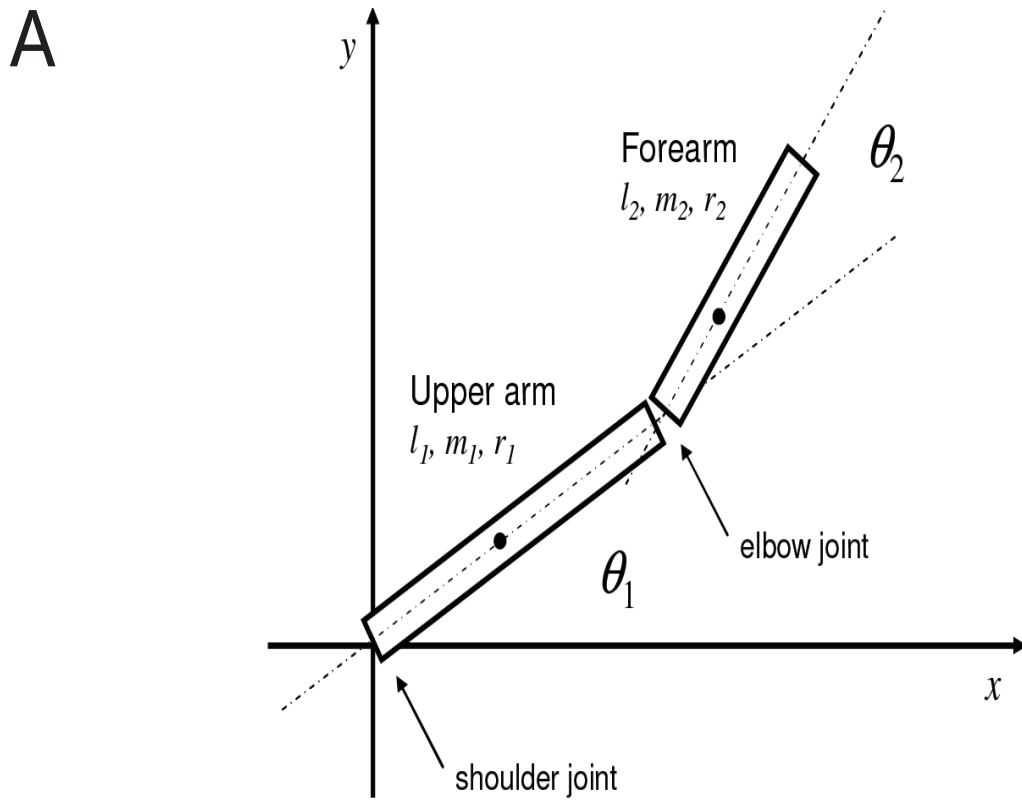


**Fig. 5.3 (A)** Illustration for an arm model. Let  $m_1$ ,  $l_1$  and  $I_1$  be the mass, length and the moment of inertia with respect to the centre of mass for the upper arm, and  $m_2$ ,  $l_2$  and  $I_2$  for the forearm. Also,  $r_1$  and  $r_2$  are the distances of the upper arm and forearm centre of mass from the shoulder and elbow joint, respectively. Besides,  $\theta_1$  and  $\theta_2$  are the angles as indicated in the figures. **(B)** Illustration for the case of straight hand trajectory with movement duration  $T$  and distance  $d$ .

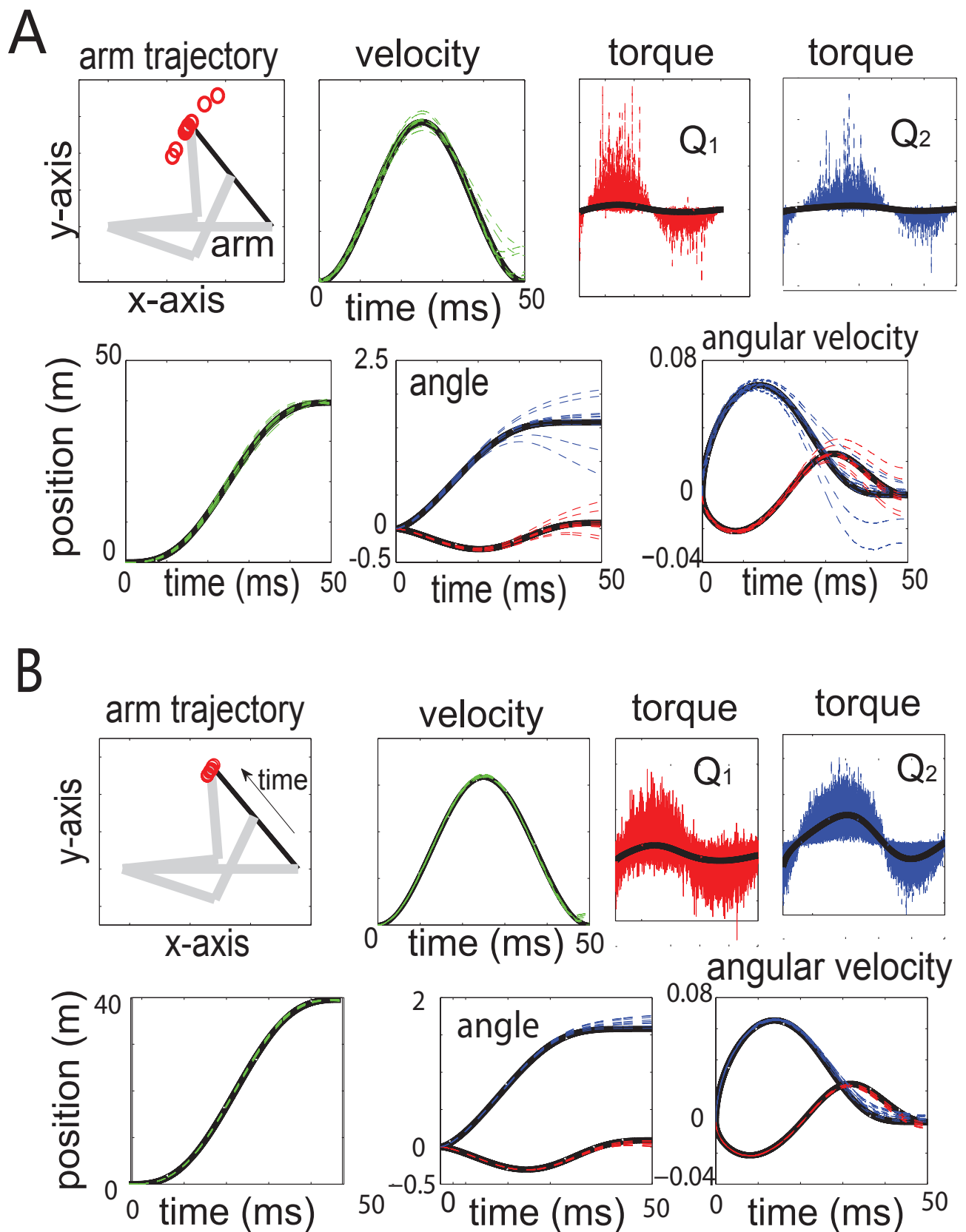


**Fig. 5.4** Simulation results for straight trajectory hand movement model. (A)  $\alpha = 1$ . The red circles represent the final position of hand at time  $t = T$  in the arm trajectory plot. (B)  $\alpha = 0.25$ . Black curves are the mean.

## 5.5 Discussion

Thanks to a novel theoretical approach, it is demonstrated in this chapter that the presence of noise in the neural control signals does not necessarily limit the precision of movements. This idea originated from the analysis of a classical model of movement control. In particular the solution to this problem changes qualitatively, depending on how fast the noise (its variance) scale with the signal amplitude. That is, while in the supralinear case ( $\alpha \geq 0.5$ ) there is a positive lower bound on the movement error, in the sublinear case ( $0 < \alpha < 0.5$ ) such lower bound vanishes, hence we can in principle find controls which reduce the movement error arbitrarily close to zero. This abrupt transition reflects the loss of convexity of the cost functional for  $\alpha < 0.5$ , which makes the most interesting case for our purposes. Clearly the only 'obvious' optimal solutions in this case, i.e. delta functions, are of little significance. Moreover, any finite approximation of this sort of control, would require an extreme temporal precision (apart from sizable power) and therefore it is hardly an option in practice.

It turns out that concentrating the control signal in two large and short pulses is not the only way to minimize the cost. The larger the pulse is, the better the control is. However, to fully comprehend what other features could lead to minimize the cost, it is necessary to reformulate the problem in more abstract terms and to introduce the concept of generalized control. Far from being only a theoretical construct, however, this approach allows us

to find sequences of ordinary control signals which asymptotically approach absolute precision. These signals are markedly different from the solutions of  $\alpha > 0.5$ , and most interestingly, lead to trajectories and velocity profiles which are compatible with the experimental ones.

Also, because our control signals are effectively distributed throughout the whole duration of the movement, they are inherently more robust to perturbations. One can see that variability in the actual implementation of our control strategy have little effect on the performance.

This theory opens up many new and significant issues to be further explored, inspired by neuroscience research but has potential ramifications in other fields, e.g. robotics.

# Chapter 6

## Conclusion and Future Work

### 6.1 Conclusion and contribution

This thesis has investigated how neurons code the external information and control movement precisely using noisy neural signals (spike frequencies and ISIs). Both biological experiments and mathematical modelling approaches were utilized to investigate the functions of single neurons and the central nervous system in discrimination and control tasks. In the first part of this thesis, the experiments of intracellular recording using the patch-clamp technique on single neurons in rat brain slices have shown increasing, decreasing, or constant firing patterns when the input stimulus frequency increases. It was experimentally observed that the neuronal responses (increasing, decreasing, or constant) depend on the amplitude of the oscillatory input. Moreover, the LIF model with the sinusoidal current injection and Poisson noise can pre-

cisely mimic the neuronal firing patterns observed in the experiment; this thesis proposed a simple mechanism to explain the principle regarding how the three firing patterns are generated (from the relative positions of the threshold value and the limit cycle of the neuronal dynamic system). The implication of this piece of work is the consistency between the experimental observations and simulation results of single neuron discrimination on stimulus frequencies. Another focus in this thesis is the novel idea to quantitatively link the psychophysical perception property (Weber's law) with neural activity. We have derived the linear relationship between the mean and the standard deviation of neural firing rate under Weber's law, which implies that the efferent spike train of a single neuron is less variable than a Poisson process, as supported by much of the literature (Harris and Wolpert, 1998; Deco and Rolls, 2006). This work further demonstrates how psychophysical behaviour reflects intrinsic neural activities quantitatively. The final focus in this thesis is how to apply a novel theoretical approach to resolve a seemingly contradictory result in the movement control problem. With the application of the Young measure method, pulses are used as neural signals; a precise control of movement is achievable even at the presence of signalling noise. Applications to saccadic eye movement and arm movement demonstrate the significant improvement of movement precisions using this novel optimization approach.

The main contributions of this thesis are:

1. An experimental design of single-neuron recording with patch-clamp and dynamic clamp techniques. In order to demonstrate the discrimi-

nation ability of the single neuron to external stimuli with various frequencies, the random permuted artificial stimuli were designed and injected into biological neurons to record the single neuron activities at different values of the mean intensities of stimulus and stimulus frequencies and to examine each neuron's sensitivity to stimulus intensities and frequencies. The experimental results indicate that single neurons could encode the stimuli frequency in their firing rates.

2. **Mathematical modelling.** The simple neuron model (LIF model) was employed to successfully simulate the experimental observations by our considering a broader but still biologically feasible parameter region, compared with earlier literature (Feng and Brown, 2004). A simple mechanism (limit cycle position in neural dynamic system) was used to explain the underlying reason of the heterogenous types of neuronal spiking patterns (increasing, decreasing, and flat), as observed in the experiments. Furthermore, the proposal was put forth that the reason for the existence of the opposing (increasing and decreasing) neural responses in the nerve system was that biological ensembles may benefit from the opposing responses in terms of the enhancement of the gain of contrast, making discrimination tasks easier to perform.
3. **Linking the psychophysical responses with neuronal behaviours.** This work theoretically derived the condition for the neuronal spike rate using a psychophysical law—namely, Weber's law. This work quantita-

tively linked psychological behaviour with neural firing property, and provided the necessary and sufficient conditions of Weber's law at the neuronal level. Weber's law indicates the conditions for the variability of neuronal spike train ( $CV_{ISI} < 1$ ); meanwhile, given a series of spike train data stimulated at different intensities, it can be justified from the spike train statistics regarding whether Weber's law holds. This study sheds light on the relation between the psychophysical behaviour and neuronal responses.

4. A novel approach to the optimization problem. This thesis applied a novel method—Young measure—to construct *generalized* solutions for the optimal movement control problems when earlier methods failed. In the presence of stochastic noise in the neural signal, this method can make the end-point error approach zero, thereby achieving a precise movement control. Two examples (saccadic eye movement and arm movement) were used to illustrate the advantages of this generalized approach to precise movement control.

## 6.2 Further extensions

### 6.2.1 Frequency coding extension

Chapter 3 primarily focused on the single neurons activity when the fixed ( $F$  is a constant) stimulus frequency was applied in the experiments and mod-

elling (periodic stimuli). In the literature, experimentalists have also applied aperiodic (or stochastic) vibrotactile stimuli in monkeys to demonstrate that firing rate encodes important information in frequency discrimination rather than periodic spike timing as neurons behave similarly to periodic and aperiodic stimuli in both S1 and S2 areas. Experiments have not yet been conducted on aperiodic stimuli on single neurons *in vitro* or simulated with the aperiodic stimulus input in modelling; it would be interesting to compare the numerical results with the experimental observations for such stochastic input frequencies. Based on the current work, stochastic artificial stimuli can be designed and applied in the experiments, and modification of current models with a stochastic frequency input could be examined in the near future.

Previous studies have demonstrated that the firing rate changes little within flutter ranges in the S1 unit (Talbot et al., 1968; Mountcastle et al., 1969; Mountcastle et al., 1990; Recanzone et al., 1992); it was initially believed that it is the periodicity of the stimuli that drove neurons to evoke highly periodic spiking trains containing the input information rather than the efferent firing rate. Although in this work it was sufficient to use neural firing rate to code the input temporal information in certain parameter regions, spike timing and the phase-locking effects of the output spike train may contain more information in other parameter regions. Thus, the research on spike timings and phase modulation at different oscillation frequencies will be further researched in greater depth.

In this work, only the simplest case of encoding and decoding one di-

mensional information-temporal frequency  $F$  was studied in detail. In fact, neurons can also decode the stimulus amplitude in terms of their firing rate as the output firing rate of a neuron is always an increasing function of the magnitude  $a$  of the applied stimulus. Future work will investigate the neural coding mechanism in high dimensions, for example, decoding both the amplitude and frequency  $(a, F)$  from the mean and CV (coefficient of variance) of efferent spike train rates rather than simply using the firing rate alone.

### **6.2.2 More systematic study on links between psychophysical laws and neural activities**

This thesis also derived the conditions for neural discharge process from a psychophysical law (Weber's law), while earlier studies focused on how to adjust single neuron models or network models to match Weber's law. Chapter 4 of this work did not consider the effect of the refractory period on the neural activities according to Weber's law; however, theoretically, the existence of the refractory period does not affect the conclusion and the simulation results. Detailed simulation results will be presented in another paper currently being finalized.

Deco and Rolls' (2006) observed Weber's law in population neurons in biased competition attractor networks. The authors claimed that the synaptic connectivity of the neural network rather than the firing rate or spike timing of single neurons resulted in the implementation of a psychophysical law.

The preliminary simulation results from work using the same neural network as Deco and Rolls support the conclusion derived from Chapter 4 that the coefficient of variation of a neural spike train is less than 1. Future studies should examine the underlying principle behind the network effects compared with the relatively simple case of single neurons.

One of the most controversial conclusions of this work in Chapter 4 was the derivation of the relation between the STD and mean of neural firing rate from Weber's law as most researchers believe that the variance, not the STD, is linearly proportional to the mean firing rate. Thus far, it is still unclear how the variability of the neural spiking process is related to its firing intensity when performing a specific task. I will focus on extending this derivation from Weber's law into other psychophysical behaviours, such as Fitts' law, Hick's law, or Steven's power law, in the near future in order to investigate whether the neural activities derived herein from Weber's law also fit other psychophysical observations.

### **6.2.3 Applications of movement control**

Chapter 5 made advances by applying the generalized control method (using Young measure theory) to understanding the principle of movement control at a computational level. This control method has proven very useful through the two simplified movement simulations. This approach has huge potential in the application of motor control of biological systems. Therefore, I will seek to realize this novel approach in the applications of clinical indus-

try, such as human-robot interfaces or the treatment of Parkinson's disease.

# Appendix A

## Bibliography

Adrian EDA (1932) The mechanism of nervous action; electrical studies of the neurone. Philadelphia, London,: University of Pennsylvania Press; H. Milford, Oxford University Press.

Barlow HB, Narasimhan R (1972) Visual pattern analysis in machines and animals. *Science* 177(4049), 567-575 .

Bays PM, Wolpert DM (2007) Computational principles of sensorimotor control that minimize uncertainty and variability. *Journal of Physiology-London* 578:387-396.

Bear MF, Abraham WC (1996) Long-term depression in hippocampus. *Annual Review of Neuroscience* 19:437-462.

Britten KH, Shadlen MN, Newsome WT, Movshon JA (1992) The Analysis of Visual-Motion - a Comparison of Neuronal and Psychophysical Performance. *Journal of Neuroscience* 12:4745-4765.

- Brody CD, Hernandez A, Zainos A, Romo R (2003) Timing and neural encoding of somatosensory parametric working memory in macaque prefrontal cortex. *Cerebral Cortex* 13:1196-1207.
- Brown D, Feng JF, Ferrick S (1999) Variability of firing of Hodgkin-Huxley and FitzHuge-Nagumo neurons with stochastic input. *Phys. Rev. Lett.* 82: 4731-4734.
- Burkitt AN (2006) A review of the integrate-and-fire neuron model: I. Homogeneous synaptic input. *Biological Cybernetics* 95:1-19.
- Campos F.M.M.O and Calado J.M.D. (2009) Approaches to human arm movement control—A review. *Annu Rev in Control.* 33: 69-77.
- Celebrini S, Newsome WT (1994) Neuronal and Psychophysical Sensitivity to Motion Signals in Extrastriate Area Mst of the Macaque Monkey. *Journal of Neuroscience* 14:4109-4124.
- Christen M, Nicol A, Kendrick K, et al (2006) Odour Encoding in Olfactory Neuronal Networks Beyond Synchronisation. *Neuroreport* 17: 1499-1502.
- Cox D. R SWL (1954) One the superposition of renewal processes. *Biometricka* 41:91-99.
- Cox DR, Isham V (1980) Point processes. London ; New York: Chapman and Hall.
- Cox DR, Miller HD (1965) The theory of stochastic processes. New York,,: Wiley.
- Dayan P, Abbott LF (2001) Theoretical neuroscience : computational and mathematical modeling of neural systems. Cambridge, Mass.: Massachusetts

Institute of Technology Press.

de la Rocha J, Doiron B, Shea-Brown E, Josic K, Reyes A (2007) Correlation between neural spike trains increases with firing rate. *Nature* 448:802-806.

Deco G, Rolls ET (2006) Decision-making and Weber's law: a neurophysiological model. *European Journal of Neuroscience* 24:901-916.

Destexhe AaB, T. (2009) *The Dynamic-Clamp: From Principles to Applications*, in press, Edition: Springer.

Djurisic M, Antic S, Chen WR, Zecevic D. (2004) Voltage imaging from dendrites of mitral cells: EPSP attenuation and spike trigger zones. *Journal of Neuroscience* 24:6703-6714.

Douglas RJ, Martin KAC (1991) Opening the Gray Box. *Trends in Neurosciences* 14:286-293.

Drachman DA (2005) Do we have brain to spare? *Neurology* 64:2004-2005.

Enoki R, Namiki M, Kudo Y, Miyakawa H (2002) Optical monitoring of synaptic summation along the dendrites of CA1 pyramidal neurons. *Neuroscience* 113:1003-1014.

Faisal AA, Selen LPJ, Wolpert DM (2008) Noise in the nervous system. *Nature Reviews Neuroscience* 9:292-303.

Fechner GT, Adler HE, Howes DH, Boring EG (1966) *Elements of psychophysics*. New York,: Holt.

Feng JF (2001) Is the integrate-and-fire model good enough? a review. *Neural Networks* 14:955-975.

Feng JF (2004) *Computational Neuroscience*, Chapman and Hall/CRC Press.

- Feng JF, Brown D (2004) Decoding input signals in time domain - A model approach. *Journal of Computational Neuroscience* 16:237-249.
- Feng JF, Tartaglia G, and Tirozzi B (2004) A note on the minimum variance theory and beyond. *J. Phys. A.* 37: 4685-4700.
- Feng JF, Tuckwell H.C (2003) Optimal Control of Neuronal Activity. *Phys. Rev. Lett.* 91: 018101.
- Feng JF, and Zhang KW (2002) Towards A Mathematical Foundation of Minimum-Variance Theory. *J. Phys. A* 35: 7287-7304.
- Fenton AA, Muller RU (1998) Place cell discharge is extremely variable during individual passes of the rat through the firing field. *Proc Natl Acad Sci U S A* 95:3182-3187.
- Fiser J, Chiu CY, Weliky M (2004) Small modulation of ongoing cortical dynamics by sensory input during natural vision. *Nature* 431:573-578.
- Gawne TJ, Richmond BJ (1993) How Independent Are the Messages Carried by Adjacent Inferior Temporal Cortical-Neurons. *Journal of Neuroscience* 13:2758-2771.
- Gescheider GA, Bolanowski SJ, Verrillo RT, Arpajian DJ, Ryan TF (1990) Vibrotactile Intensity Discrimination Measured by 3 Methods. *Journal of the Acoustical Society of America* 87:330-338.
- Goenechea L, von der Emde G (2004) Responses of neurons in the electrosensory lateral line lobe of the weakly electric fish *Gnathonemus petersii* to simple and complex electrosensory stimuli. *Journal of Comparative Physiology a-Neuroethology Sensory Neural and Behavioral Physiology* 190:907-922.

Hamilton AFD, Jones KE, Wolpert DM (2004) The scaling of motor noise with muscle strength and motor unit number in humans. *Experimental Brain Research* 157:417-430.

Hanson FB (2007) *Applied Stochastic Processes and Control for Jump-Diffusions: Modeling, Analysis and Computation*, SIAM Books: Advances in Design and Control Series, Cambridge University Press: Cambridge UK.

Harris CM, Wolpert DM (1998) Signal-dependent noise determines motor planning. *Nature* 394:780-784.

Harsch A, Robinson HPC (2000) Postsynaptic variability of firing in rat cortical neurons: The roles of input synchronization and synaptic NMDA receptor conductance. *Journal of Neuroscience* 20:6181-6192.

Hirase H, Czurko A, Csicsvari J, Buzsaki G (1998) Hippocampal pyramidal neurons "space-clamped" in a running wheel task: Place cells or path integrators? *European Journal of Neuroscience* 10:259-259.

Holt GR, Koch C (1997) Shunting inhibition does not have a divisive effect on firing rates. *Neural Computation* 9:1001-1013.

Horton P, et. al. (2005) Applications of multi-variate analysis of variance (MANOVA) to multi-electrode array electrophysiology data *J. Neurosci. Methods* 146: 22-41.

Jones KE, Hamilton AFD, Wolpert DM (2002) Sources of signal-dependent noise during isometric force production. *Journal of Neurophysiology* 88:1533-1544.

Kandel ER, Schwartz JH, Jessell TM (2000) *Principles of Neural Science*, 4th

ed. McGraw-Hill, New York.

Kara P, Reinagel P, Reid RC (2000) Low response variability in simultaneously recorded retinal, thalamic, and cortical neurons. *Neuron* 27:635-646.

Kast B (2001) Decisions, decisions... *Nature* 411:126-128.

Keener JP, Hoppensteadt FC, Rinzel J (1981) Integrate-and-Fire Models of Nerve Membrane Response to Oscillatory Input. *Siam Journal on Applied Mathematics* 41:503-517.

Knierim JJ, Vanessen DC (1992) Neuronal Responses to Static Texture Patterns in Area-V1 of the Alert Macaque Monkey. *Journal of Neurophysiology* 67:961-980.

Kohn A, Smith MA (2005) Stimulus dependence of neuronal correlation in primary visual cortex of the macaque. *Journal of Neuroscience* 25:3661-3673.

Kolobov MI (1999) The spatial behavior of nonclassical light. *Reviews of Modern Physics* 71:1539-1589.

Koulakov AA, Raghavachari S, Kepecs A, Lisman JE (2002) Model for a robust neural integrator. *Nature Neuroscience* 5:775-782.

Lawrance AJ (1973) Dependency of Intervals between Events in Superposition Processes. *Journal of the Royal Statistical Society Series B-Statistical Methodology* 35:306-315.

Leng G, Brown CH, Bull PM, Brown D, Scullion S, Currie J, Blackburn-Munro RE, Feng JF, Onaka T, Verbalis JG, Russell JA, Ludwig M (2001) Responses of magnocellular neurons to osmotic stimulation involves coactivation of excitatory and inhibitory input: An experimental and theoretical

analysis. *Journal of Neuroscience* 21:6967-6977.

Luna R, Hernandez A, Brody CD, Romo R (2005) Neural codes for perceptual discrimination in primary somatosensory cortex. *Nature Neuroscience* 8:1210-1219.

Machens CK, Romo R, Brody CD (2005) Flexible control of mutual inhibition: A neural model of two-interval discrimination. *Science* 307:1121-1124.

Mahns DA, Perkins NM, Sahai V, Robinson L, Rowe MJ (2006) Vibrotactile frequency discrimination in human hairy skin. *Journal of Neurophysiology* 95:1442-1450.

Meyer DE, Kornblum S, Abrams RA, Wright CE, Smith JEK (1988) Optimality in Human Motor-Performance - Ideal Control of Rapid Aimed Movements. *Psychological Review* 95:340-370.

Miller P, Wang XJ (2006) Inhibitory control by an integral feedback signal in prefrontal cortex: A model of discrimination between sequential stimuli. *Proceedings of the National Academy of Sciences of the United States of America* 103:201-206.

Morita K, Kalra R, Aihara K, Robinson HPC (2008) Recurrent synaptic input and the timing of gamma-frequency-modulated firing of pyramidal cells during neocortical "UP" states. *Journal of Neuroscience* 28:1871-1881.

Neher E, Sakmann B (1976) Single-channel currents recorded from membrane of denervated frog muscle fibres. *Nature* 260:799-802.

Newsome WT, Britten KH, Movshon JA (1989) Neuronal Correlates of a Perceptual Decision. *Nature* 341:52-54. Nicolelis MAL (2003) Brain-machine

interfaces to restore motor function and probe neural circuits. *Nature Reviews Neuroscience* 4:417-422.

Osborne LC, Lisberger SG and Bialek W (2005) Time course of information about motion direction in visual area MT. *Nature* 437: 412-416.

Parker AJ, Newsome WT (1998) Sense and the single neuron: Probing the physiology of perception. *Annual Review of Neuroscience* 21:227-277.

Pedregal P (1999) Optimization, Relaxation and Young Measures. *Bull. Amer. Math. Soc.* 36: 27-58.

Recanzone GH, Merzenich MM, Schreiner CE (1992) Changes in the Distributed Temporal Response Properties of Si Cortical-Neurons Reflect Improvements in Performance on a Temporally Based Tactile Discrimination Task. *Journal of Neurophysiology* 67:1071-1091.

Robinson DA, Gordon JL, Gordon SEA (1986) A model of the smooth pursuit eye movement system. *Biol Cybern* 55: 43-57.

Robinson HPC, Kawai N (1993) Injection of Digitally Synthesized Synaptic Conductance Transients to Measure the Integrative Properties of Neurons. *Journal of Neuroscience Methods* 49:157-165.

Romo R (2001) Touch and go: Decision-making mechanisms in somatosensation. *Annual Review of Neuroscience* 24:107-137.

Romo R, Hernandez A, Zainos A, Salinas E (2003) Correlated neuronal discharges that increase coding efficiency during perceptual discrimination. *Neuron* 38:649-657.

Romo R, Salinas E (2003) Flutter discrimination: Neural codes, perception,

- memory and decision making. *Nature Reviews Neuroscience* 4:203-218.
- Sakmann B, Neher E (1995) *Single-channel recording*, 2nd Edition. New York: Plenum Press.
- Salinas E, Hernandez A, Zainos A, Romo R (2000) Periodicity and firing rate as candidate neural codes for the frequency of vibrotactile stimuli. *Journal of Neuroscience* 20:5503-5515.
- Sawamura H, Shima K, Tanji J (2002) Numerical representation for action in the parietal cortex of the monkey. *Nature* 415:918-922.
- Schmidt RA, Zelaznik H, Hawkins B, Frank JS, Quinn JT (1979) Motor-Output Variability - Theory for the Accuracy of Rapid Motor Acts. *Psychological Review* 86:415-451.
- Shadlen MN, Newsome WT (1994) Noise, neural codes and cortical organization. *Curr Opin Neurobiol* 4:569-579.
- Shadlen MN, Newsome WT (1998) The variable discharge of cortical neurons: Implications for connectivity, computation, and information coding. *Journal of Neuroscience* 18:3870-3896.
- Sharp AA, Oneil MB, Abbott LF, Marder E (1993) The Dynamic Clamp - Artificial Conductances in Biological Neurons. *Trends in Neurosciences* 16:389-394.
- Simmons G and Demiris Y (2005) Optimal Robot arm control using the minimum variance model. *J. Robotic Systems* 22: 677-690.
- Smith VC, Pokorny J, Lee BB, Dacey DM (2008) Sequential processing in vision: The interaction of sensitivity regulation and temporal dynamics. Vi-

sion Research 48:2649-2656.

Stevens SS (1961) To Honor Fechner and Repeal His Law: A power function, not a log function, describes the operating characteristic of a sensory system. Science 133:80-86.

Stuart GJ, Dodt HU, Sakmann B (1993) Patch-Clamp Recordings from the Soma and Dendrites of Neurons in Brain-Slices Using Infrared Video Microscopy. Pflugers Archiv-European Journal of Physiology 423:511-518.

Talbot WH, Darian-Smith I, Kornhuber HH, Mountcastle VB (1968) The sense of flutter-vibration: comparison of the human capacity with response patterns of mechanoreceptive afferents from the monkey hand. J Neurophysiol 31:301-334.

Tanaka H, Krakauer J, and Qian N. (2006) An Optimization Principle for Determining Movement Duration. J. Neurophysiol. 95: 3875-3886.

Tuckwell H. C (1984) Theoretical Neurobiology, CUP: Cambridge, UK.

Tuckwell H. C (1989) Stochastic processes in the neurosciences. Philadelphia, Pa.: Society for Industrial and Applied Mathematics.

Valadier M (1990) Young measures. Methods of Nonconvex Analysis, Lecture Notes Math. 1446, Springer-verlag: Berlin, 152-188.

Van Beers RJ (2007) The Sources of Variability in Saccadic Eye Movements. Journal of Neuroscience 27: 8757-8770.

Vega-Bermudez F, Johnson KO (1999) SA1 and RA receptive fields, response variability, and population responses mapped with a probe array. Journal of Neurophysiology 81:2701-2710.

Vonderemde G, Bell CC (1994) Responses of Cells in the Mormyrid Electroreceptive Lobe to Eods with Distorted Wave-Forms - Implications for Capacitance Detection. *Journal of Comparative Physiology a-Sensory Neural and Behavioral Physiology* 175:83-93.

Vonderemde G, Bleckmann H (1992) Differential Responses of 2 Types of Electroreceptive Afferents to Signal Distortions May Permit Capacitance Measurement in a Weakly Electric Fish, *Gnathonemus-Petersii*. *Journal of Comparative Physiology a-Sensory Neural and Behavioral Physiology* 171:683-694.

Werner G, Mountcastle VB (1963) The Variability of Central Neural Activity in a Sensory System, and Its Implications for the Central Reflection of Sensory Events. *J Neurophysiol* 26:958-977.

Wilbur WJ, Rinzel J (1983) A Theoretical Basis for Large Coefficient of Variation and Bimodality in Neuronal Interspike Interval Distributions. *Journal of Theoretical Biology* 105:345-368.

Williams RW, Herrup K (1988) The Control of Neuron Number. *Annual Review of Neuroscience* 11:423-453.

Winter DA (2004) *Biomechanics and Motor Control of Human Movement*, Wiley.

Yoshimura Y, Dantzker JLM, Callaway EM (2005) Excitatory cortical neurons form fine-scale functional networks. *Nature* 433:868-873.

Young LC (1937) Generalized curves and the existence of an attained absolute minimum in the calculus of variations. *C.R. Soc. Sci. Lettres de Varsovie*,

Cl. III 30: 212-234.

Young LC (1942) Generalized surfaces in the calculus of variations. *Ann. of Math.* 43: 84-103; 530-544.

Zohary E, Shadlen MN, Newsome WT (1994) Correlated Neuronal Discharge Rate and Its Implications for Psychophysical Performance (Vol 370, Pg 140, 1994). *Nature* 371:358-358.

# Appendix B

## Selected Matlab code used in this thesis

Due to the length of the Matlab code that I wrote for modelling and simulation throughout my PhD work, selected Matlab code are presented in this appendix. For the complete set of the programming, please go to my ePortfolio at

<http://www2.warwick.ac.uk/study/csde/gsp/eportfolio/directory/pg/msrfai/matlabcodings> .

### B.1 Code for modelling in chapter 3

```
clear all;
clc;
close all;

a =[20.5 16.8 10]; %value of a for three different cases: 1.flat, 2.
decrease, 3.increase
ratio = 0; %ratio between # of inhibitory synapses and excitatory
synapses
refr = [5 1 1]; % refractory period
%NN = [50 39 50]; % number of neurons in a network
NN = [1 1 1]; %single neuron
T = 1000; %ms, total time
dt = .01; % in msec, time step
F=[ 10:10:60];
w = [1 1 1]; % ;
```

*Appendix B: Matlab code used in this thesis*

```

gamma = [20 20 9];
k = [0 0 1.5];

runs = 1000;
FR = zeros(runs,size(F,2));

for z = 1:3
    if z == 1
        weight=randn(NN(z),NN(z));
        Tsteps = round((T+refr(z))/dt);
        vshow=zeros(size(F,2),Tsteps-1);
        Iapp = zeros(size(F,2),Tsteps);
        for y=1:size(F,2)
            for x=1:runs
                [FR(x,y),vshow(y,:), Iapp(y,:)] = IF_network1(NN(z), T,
dt,Tsteps, F(y),a(z),ratio(1), gamma(z),w(z),k(z),weight, refr(z));
            end
        end
        FF1=mean(FR);
        figure(1); subplot(3,2,2*z-1); plot(F, FF1,'o-'); hold off;
        figure(2); subplot(3,2,2*z); plot(vshow(1,:)); axis([2000 7000
-10 50]);
                subplot(3,2,4*z); plot(vshow(3,:)); axis([2000 7000
-10 50]);
                subplot(3,2,6*z); plot(vshow(5,:)); axis([2000 7000
-10 50]);

        elseif z == 2
            weight = rand(NN(z), NN(z));
            Tsteps = round((T+refr(z))/dt);
            vshow = zeros(NN(z),Tsteps);
            Iapp = zeros(size(F,2),Tsteps);
            for y=1:size(F,2)
                for x=1:runs
                    [FR(x,y),vshow, Iapp(y,:)] = IF_network1(NN(z), T,
dt,Tsteps, F(y),a(z),ratio(1), gamma(z),w(z),k(z),weight, refr(z));
                end
            end
            FF2=mean(FR);
            figure(1); subplot(3,2,2*z-1); plot(F, FF2,'-'); %axis([0 55 -
10 100]);
            figure(2); subplot(3,2,z); plot(vshow); axis([2000 7000 -10
50]); hold on; plot(Iapp(1,:));
            %             subplot(3,2,2*z); plot(vshow(3,:)); axis([2000
7000 -10 50]); hold on; plot(Iapp(3,1:end-1));
            %             subplot(3,2,3*z); plot(vshow(5,:)); axis([2000
7000 -10 50]); hold on; plot(Iapp(5,:));

        else
            weight = randn(NN(z), NN(z));
            Tsteps = round((T+refr(z))/dt);
            vshow = zeros(NN(z),Tsteps-1);
            vol = zeros(size(F,2), Tsteps-1);
            Iapp = zeros(size(F,2),Tsteps);
            for y=1:size(F,2)
                for x=1:runs

```

### Appendix B: Matlab code used in this thesis

```

        [FR(x,y),vshow, Iapp(y,:)] = IF_network1(NN(z), T,
dt,Tsteps, F(y),a(z),ratio(1), gamma(z),w(z),k(z),weight, refr(z));
        vol(y,:) = vshow(1,:);
    end
end
FF3=mean(FR);
figure(1); subplot(3,2,2*z); plot(F, FF3,'o');hold on;
figure(2);
for g = 1:size(F,2)
    subplot(2,3,g);plot(vol(g,:), 'b'); hold on;
plot(Iapp(g,:), 'r');hold off;
end
end
end

%save('networkinc.mat','FR','F');

```

---

```

%IF model with population connected weight network
%dvi/dt=-(Vi-Vrest)/gamma+Isyn(t)+sum wji*delta(t-tjq)

function [FR,vshow, I] = IF_network1(NN,T,dt,Tsteps, F,a,r,gamma,w,
k,weight, refr)

thres = 20; %threshold value to define a spike
Vrest = 0; %mV, =EL
s = gamma/dt;
vshow = zeros(NN,Tsteps-1);

% initial conditions:
Volt = Vrest*zeros(NN,1); %ms
vshow(:,1) = Vrest;

Ns = 100; %number of synapses for each neuron
a = a*1e-3; F = F*1e-3; %ration between inh and exc.

mu_weight = 0;
st_weight = 1;
weight = mu_weight+st_weight*weight;

tt = [1:Tsteps]; %tt is a vector now
%brownian motion for Isyn
lambdaE = a/2*(1+cos(2.*pi.*F.*tt.*dt)); %
lambdat = lambdaE.*Ns;%size(lambdat)
mu = w*lambdat*(1-r);%size(mu)
sigma2 = w^2*lambdat*(1+r);% size(sigma2)
sigma = sqrt(sigma2);
[Bt] = brownian1(Tsteps,0,1,1);
dBt = Bt(2:end) - Bt(1:end-1);
dIapp = kron(mu*dt, ones(NN,1)) ;
dBt = dBt';
noise = kron(sigma.*dBt,ones(NN,1)); % NOTE THAT BROWNIAN
noise=sigma.*dBt;
% MOTION IS ACTUALLY N(0,T)*SQRT(STEP SIZE), HERE STEP SIZE IS dt,
but
Iapp=(dIapp + noise*1)/dt ;

```

### Appendix B: Matlab code used in this thesis

```

t = zeros(NN, 1);
j = ones(NN,1);
spikes = 0;
omega = randn(NN,1)*0*1e-3+50*1e-3;

while t < T
    for l = 1:NN
        j(l) = j(l)+1;
        t(l) = (j(l)-1)*dt;
        if Volt(l) > thres
            Volt(l) = Vrest;
            vshow(l,j(l)) = thres + 20;
            spikes = spikes + 1;
            for m = 1:NN
                if m ~= l
                    %Volt(m) = (s*Volt(m)+Vrest+gamma*(Iapp(m,j(l)-
1)+weight(m,l))+gamma*k*(cos(2*pi*omega(l)*t(l))+1))/(s+1);
                    Volt(m) = Volt(m) + weight(m,l);
                    vshow(m,j(l)) = Volt(m);
                end
            end
            j(l) = j(l) + round(refr/dt) ;
            t(l) = t(l) + refr;
        else
            % Volt(l) = (s*Volt(l)+Vrest+gamma*Iapp(l,j-1))/(s+1);
            Volt(l) = (s*Volt(l)+Vrest+gamma*Iapp(l,j(l)-
1)+gamma*k*(cos(2*pi*omega(l)*t(l))+1))/(s+1);
            vshow(l,j(l))=Volt(l);
        end
    end
end
end
T=T*1e-3;
FR=spikes/T/NN;
I = Iapp(1,:);

```

## B.2 Code for simulation in chapter 4

```

close all;
clc
clear all;

alpha = 0.15; %misclassification rate
C = sqrt(pi/2*log(1/(1-(1-alpha)^2)));

%define the renewal process:  $N_t \sim (1/ET, \text{Var}(T)/(ET)^3)$ , where T is the
ISI
%following gamma distribution

samples =1000;
dmu = 0.1;
mu = [2:dmu:200]'; % this is the mean for output spiking rate
n_ISI = round(1.2*mu);
Nt = zeros(size(mu,1),samples);

```

*Appendix B: Matlab code used in this thesis*

```

% %-----
---
% %using exponential ISI to generate Poisson distri spike count
% mu = [2:100]'; % this is the mean for output spiking rate
% sigma = sqrt(mu); %for poisson
% n_ISI = round(1.2*mu);
% Nt = zeros(size(mu,1),samples);
%
% for ii = 1:size(mu,1)
%     x = zeros(size(mu,1),n_ISI(ii));
%     x_time = zeros(size(mu,1),n_ISI(ii));
%     for jj = 1:samples
%         x(ii,:) = exprnd(1/mu(ii), [1 n_ISI(ii)]);
%         x_time(ii,:) = cumsum(x(ii,:));
%         Nt(ii,jj) = n_ISI(ii)/x_time(ii,end);
%     end
%     diff = var(x(ii,:))-(mean(x(ii,:)))^2;
% end
% mean_Nt = mean(Nt');
% var_Nt = var(Nt');
% std_Nt = std(Nt');
%
% compare_mu = mean_Nt - mu';
% compare_sigma = std_Nt-sigma';
% VMR = mean(var_Nt./mean_Nt);

%-----
%using gamma distri ISI to generate sub or supra-Poisson
%as for gamma distri, mu_gamma = k*theta = A*B, var_gamma = k*theta^2 =
%A*B^2, then for Nt~(1/(A*B), A*B^2/(A*B)^3),

%case 1. CV = 1
CV = .2;
A = 1/CV^2;
B = 1/A./mu; %these are the two parameter for gamma distri
sigma = 1/A./sqrt(B);
for ii = 1:size(mu,1)
    x = zeros(size(mu,1),n_ISI(ii));
    x_time = zeros(size(mu,1),n_ISI(ii));
        for jj = 1:samples
            x(ii,:) = gamrnd(A,B(ii), [1 n_ISI(ii)]);
            x_time(ii,:) = cumsum(x(ii,:));
            Nt(ii,jj) = n_ISI(ii)/x_time(ii,end);
        end
end

%     mean_Nt = mean(Nt');
%     var_Nt = var(Nt');
%     std_Nt = std(Nt');
%     sigma = 1/A./sqrt(B);
%     compare_mu = mean_Nt - mu';
%     compare_sigma = std_Nt-sigma';
%     VMR = mean(var_Nt./mean_Nt);
%     figure(100); plot(compare_mu,'b');hold on;
plot(compare_sigma,'r');hold on;

```

*Appendix B: Matlab code used in this thesis*

```

%      plot(VMR,'g');hold off;

delt = zeros( size(mu,1), 1);
for i = 1:size(mu,1)
    for j = i:size(mu,1)
        x0 = mu(j)*sigma(i)/(sigma(i)+sigma(j)) +
mu(i)*sigma(j)/(sigma(i)+sigma(j));
        A1 = sum(Nt(i,:)>x0);
        B1 = sum(Nt(j,:)<x0);
        area = A1+B1;
        alpha = area/2/samples;
        if alpha < 0.15
            delt(i) = (j - i)*dmu;
            break;
        end
    end
end
n = sum (delt >0);
m = round((CV*10)^2/dmu);
figure(1);
subplot(1,3,2);
plot(mu(1:ceil(1/dmu)*10:n),delt(1:ceil(1/dmu)*10:n),'.r');hold on;
coef = polyfit(mu(m:ceil(1/dmu)*10:n),delt(m:ceil(1/dmu)*10:n),1);
linfit = polyval(coef,mu(m:ceil(1/dmu)*10:n));
plot(mu(m:ceil(1/dmu)*10:n), linfit,'k-');hold on;
plot([m m]*dmu,[0 max(delt)],'k'); hold off;
slope = (max(linfit)-min(linfit))/range(mu(m:n));
title(['Poisson, CV_{ISI} = ' num2str(CV) ', slope = '
num2str(slope)]);
xlabel('\lambda (spikes/sec)');

```

---

```

%generate correlated spike trains over sliding window
% single neuron ISI generation follow Gamma(A,B)
clc;
clear all;
%close all;

Tref = 1*1e-3; %ms
CV = .5;
WIN = 20; %:10:100;%unit: second, take the length of each window as
20 ms
win = WIN*1e-3;
p = 10; % number of population neurons
dmu = .5;
mu = 2:dmu:120; %Hz, each neuron mean firing rate-correspond to Nt mean
n_window_count = 1001;
datay = zeros(size(mu,2),n_window_count-1);

%define the correlation matrix
rho = 0.1;
M = rho*ones(p,p);
for i = 1:p
    M(i,i) = 1;
end

rand('state',rem(now,1));

```

*Appendix B: Matlab code used in this thesis*

```

for aa = 1:size(mu,2)
    samp_freq = 100*mu(aa)*p; %for each second, we take 20000 divisions,
    like 20000 steps
    A = (1-mu(aa)*Tref)^2/CV^2;
    B = CV^2/(mu(aa).*(1-mu(aa)*Tref)); %these are the two parameter
for gamma distri
    % B = 1/(A*mu(aa)); %shape parameter
    samples = 1.2*mu(aa); % number of spikes generated by each neuron;
    %window
    window_step = samp_freq*win; % the length of each window in terms
    of how many steps used
    slide_step = 1*1e-3*samp_freq;

    x = gamrnd(A, B, p, samples); % unit: second. the ISI distribution
    generated for p neurons, with 1000spikes each
    x_time = cumsum(x,2); %spike timing, unit: second%
    x_count_w = zeros(p,n_window_count); %firing rate for each single
    neuron

        for i = 1:n_window_count-1
            timeduration = (slide_step*(i-
1)+1:window_step+slide_step*(i-1))/samp_freq;
            index1x = (x_time >= timeduration(1));
            index2x = (x_time <= timeduration(end));
            x_count_w(:,i) = sum(index1x & index2x, 2);
        end
        xw = x_count_w(:,1:end-1);
        xw1 = xw - mu(aa) *win;
        zw1 = sqrtm(M) * xw1; %expected var(zw) = win^2 * sigma^2 * M
        yw1 = ones(1,p) * zw1;
        yw = yw1 + mu(aa) * win * p;
        datay(aa,:) = yw/p;
end

figure(20);
subplot(2,2,1); plot(var(datay'));hold on; plot(mu*win *1/A*(1+(p-
1)*rho)/p, 'r');hold off;

muy = mean(datay,2)';
sigmay = std(datay');

%test Weber's law
delt = zeros(1, size(mu,2));
for ii = 1:size(mu,2)
    for jj = ii+1:size(mu,2)
        x0 = muy(jj)*sigmay(ii)/(sigmay(ii)+sigmay(jj)) +
muy(ii)*sigmay(jj)/(sigmay(ii)+sigmay(jj));
        A1 = sum(datay(ii,:) > x0);
        B1 = sum(datay(jj,:) < x0);
        area = A1+B1;
        totalarea = size(datay,2) * 2;
        alpha = area/2/totalarea;
        if alpha < 0.15
            delt(ii) = (jj - ii)*dmu;
            break;
        end
    end
end

```

*Appendix B: Matlab code used in this thesis*

```

        end
    end
end
n = sum (delt > 0);

%m = 1;
m = round(1/A*100/dmu/(p/(1+(p-1)*rho)));
m2 = n;
%m2 = round(1/A*10000/dmu/NN);

jump = 1;
figure(WIN); subplot(2,2,4);
plot(muy(1:ceil(1/dmu)*jump:n)/win,delt(1:ceil(1/dmu)*jump:n),'.r');
hold on;
%use linear regression to fit data
coef =
polyfit(muy(m:ceil(1/dmu)*jump:m2)/win,delt(m:ceil(1/dmu)*jump:m2),1);
linfit = polyval(coef,muy(m:ceil(1/dmu)*jump:m2)/win);
plot(muy(m:ceil(1/dmu)*jump:m2)/win, linfit,'k-');hold on;
plot([m m]*dmu,[0 max(delt)],'k'); hold off;
slope = (max(linfit)-min(linfit))/range(muy(m:ceil(1/dmu)*jump:m2))
*win;
xlabel('\mu_{yw}'); ylabel('\Delta \mu_{yw}');
title(['Weber law in window ' num2str(win*1e3) '(ms), slope = '
num2str(slope)]);

%plot out histogram for the superposition firing rate at each single
rate mu value
figure(200);
for cc = 1:round(1/dmu):size(mu,2)

subplot(10,10,ceil(cc*dmu));hist(datay(cc,:)/win,40);xlabel(['\mu_{sing
le} = ' num2str(mu(cc))]);
    %xlim([0 200]); ylim([0 100]);
end



---


clc; clear all; close all;
% theoretical solution for sigmoid input-output relation
C = 1.4;
R0 = 120;

%CV value when k = 0.05
k = 0.05;
color = ['r' 'b' 'g' 'k' 'y' 'm' 'p' 'o' '+' '*' 'r' 'b' 'g' 'k' 'y'
'm' 'p' 'o' '+' '*'];
time_step = 1000;
k0 = k*R0*(log(R0/5-1)-log(R0/(R0-5)-1))/(R0-10);
I0 = R0/k0*(log(R0/5-1)-log(R0/(R0-5)-1));
slope = (R0-10)/I0;
mu_range = 0:I0;
sigmoid = R0./(1+exp(-k0*(mu_range-1/2*I0)/R0));
figure(1); plot(mu_range, sigmoid);title(['mu vs. I_0']);hold on;
t1 = R0/(1+exp(-(0-0.5*I0)*k0/R0));
t2 = R0/(1+exp(-(I0-0.5*I0)*k0/R0));
Tspan = [t1 t2]; %t is the mean firing rate mu, y is sigma = f(mu)

```

*Appendix B: Matlab code used in this thesis*

```

ft = linspace(t1,t2,time_step); %define the time step, which is range
of valid mu
h = R0./(ft.*(1+(R0./ft -1).^(k+1)*exp(-k0*k*I0/(2*R0)))) -1;
f = 2./(ft.*h);
gt = ft;
g = 1/C*ones(size(gt));
validindex = find(h>0.01);
ft1 = ft(validindex);
h1 = h(validindex);
f1 = f(validindex);
gt1 = ft1;
g1 = g(validindex);
hk = k*ones(size(ft1));
fk = 2./(ft1*k);
newindex = find(f1<fk);
t1_new = ft1(newindex(1));
Tspan1 = [t1_new t2];
IC = k*t1; %y(t=t1) = slope k * initial firing rate t1;
[T Y] = ode23s(@(t,y) webfun(t,y,ft1,f1,gt1,g1),Tspan1,IC); % Solve ODE
CV = Y.*sqrt(1./T);
CVISI = CV;
smallindex = find( T <= 100 );
CV_rangel = max(CVISI(smallindex));

%calculate value of CV when k = 0.3
k = 0.3;
color = ['r' 'b' 'g' 'k' 'y' 'm' 'p' 'o' '+' '*' 'r' 'b' 'g' 'k' 'y'
'm' 'p' 'o' '+' '*'];
time_step = 1000;
k0_2 = k*R0*(log(R0/5-1)-log(R0/(R0-5)-1))/(R0-10);
I0 = R0/k0_2*(log(R0/5-1)-log(R0/(R0-5)-1));
slope = (R0-10)/I0;
mu_range = 0:I0;
sigmoid = R0./(1+exp(-k0_2*(mu_range-1/2*I0)/R0));
figure(1); plot(mu_range, sigmoid);title(['mu vs. I_0']);hold on;
t1 = R0/(1+exp(-(0-0.5*I0)*k0_2/R0));
t2 = R0/(1+exp(-(I0-0.5*I0)*k0_2/R0));
Tspan = [t1 t2]; %t is the mean firing rate mu, y is sigma = f(mu)
ft = linspace(t1,t2,time_step); %define the time step, which is range
of valid mu
h = R0./(ft.*(1+(R0./ft -1).^(k+1)*exp(-k0_2*k*I0/(2*R0)))) -1;
f = 2./(ft.*h);
gt = ft;
g = 1/C*ones(size(gt));
validindex = find(h>0.01);
ft1 = ft(validindex);
h1 = h(validindex);
f1 = f(validindex);
gt1 = ft1;
g1 = g(validindex);
hk = k*ones(size(ft1));
fk = 2./(ft1*k);
newindex = find(f1<fk);
t1_new = ft1(newindex(1));
Tspan1 = [t1_new t2];
IC = k*t1; %y(t=t1) = slope k * initial firing rate t1;
[T Y] = ode23s(@(t,y) webfun(t,y,ft1,f1,gt1,g1),Tspan1,IC); % Solve ODE

```

### Appendix B: Matlab code used in this thesis

```

CV = Y.*sqrt(1./T);
CVISI = CV;
MU = T;
SIGMA = Y;
largeindex = find(T <=100);
CV_range2 = min(CVISI(largeindex));

%test if k0 is bigger than the calculated value from k, what will
happen?
dk0 = .1;
i = 1;
k = 0.05;
while k0 < k0_2
    k0 = k0+dk0;
    i = i+1;
    I0 = R0/k0*(log(R0/5-1)-log(R0/(R0-5)-1));
    mu_range = 0:I0;
    sigmoid = R0./(1+exp(-k0*(mu_range-1/2*I0)/R0));
    figure(1); subplot(2,2,1); plot(mu_range, sigmoid);title(['mu
vs. I_0']);hold on;
    t1 = R0/(1+exp(-(0-0.5*I0)*k0/R0));
    t2 = R0/(1+exp(-(I0-0.5*I0)*k0/R0));
    Tspan = [t1 t2];
    ft = linspace(t1,t2,time_step); %define the time step, which is
range of valid mu
    h = R0./(ft.*(1+(R0./ft -1).^(k+1)*exp(-k0*k*I0/(2*R0)))) -1;
    f = 2./(ft.*h);
    gt = ft;
    g = 1/C*ones(size(gt));
    validindex = find(h>0.01);
    ft1 = ft(validindex);
    h1 = h(validindex);
    f1 = f(validindex);
    gt1 = ft1;
    g1 = g(validindex);
    hk = k*ones(size(ft1));
    fk = 2./(ft1*k);
    newindex = find(f1<fk);
    t1_new = ft1(newindex(1));
    Tspan1 = [t1_new t2];
    IC = k*t1; %y(t=t1) = slope k * initial firing rate t1;
    [T Y] = ode23s(@(t,y) webfun(t,y,ft1,f1,gt1,g1),Tspan1,IC); %
Solve ODE
    CV = Y.*sqrt(1./T);
    smallindex = find(T<=100);
    CV_rangel(i) = max(CV(smallindex));
end

subplot(2,2,2); plot([0.05:dk0:k0-2*dk0],CV_rangel,'r');hold on;
plot([0.05 k0], [CV_range2 CV_range2],'g');hold on;

```

## B.3 Code for simulation in chapter 5

```

clear all;
clc;

```

*Appendix B: Matlab code used in this thesis*

```

close all;

%%%%%%%%%%%%%%%%%%%%%%%%%%%%%%%%%%%%%%%%%%%%%%%%%%%%%%%%%%%%%%%%%%%%%%%%
%% TASK/MOTOR PLANT PARAMETERS
%%%%%%%%%%%%%%%%%%%%%%%%%%%%%%%%%%%%%%%%%%%%%%%%%%%%%%%%%%%%%%%%%%%%%%%%

task_parameters = 'R&F';
task_parameters = 'H&W';

switch task_parameters

    case 'R&F'

        %% (regular)
        pars.tau_1 = 1; pars.tau_2 = 2; pars.tau_3 = 0.15; pars.T = 1;
        pars.R = 0.1; pars.D = 2; pars.noise_scale=1;

        %% (anomalous)
        % pars.tau_1 = 1; pars.tau_2 = 2; pars.tau_3 = 15; pars.T = 1;
        pars.R = 0.1; pars.D = 2; pars.noise_scale=1;

        dt = 1e-3;

    case 'H&W'

        %% Default settings
        pars.tau_1 = 224; pars.tau_2 = 13; pars.tau_3 = 1e-2; pars.T =
50; pars.R = 50; pars.D = 10; pars.noise_scale = 0.58;

        %% noise_scale (CV) set as in de Beers et al. k_SDN = 0.172)
        % pars.tau_1 = 224; pars.tau_2 = 13; pars.tau_3 = 1e-2;
pars.T = 50; pars.R = 50; pars.D = 10; pars.noise_scale = 0.172;

        %% anomalous dependency of Optimal Var vs. alpha
        % pars.tau_1 = 224; pars.tau_2 = 13; pars.tau_3 = 1; pars.T =
50; pars.R = 50; pars.D = 10; pars.noise_scale = 0.58;

        %% for experimenting
        pars.tau_1 = 224; pars.tau_2 = 13; pars.tau_3 = 1e-2; pars.T =
50; pars.R = 50; pars.D = 10; pars.noise_scale = .58;

        % NB: Task duration superceded by empirical
        % Duration-Amplitude relation taken from
        % Collewijn et al.
        % Binocular co-ordination of human horizontal saccadic
eye movements.
        % The Journal of Physiology (1988)
        % vol. 404 pp. 157-82

        pars.T = 2.7 * pars.D + 23;

        dt = 1e-1; %% default 1e-2;

end

%% load previously stored initial guess values for csi/eta at different

```

*Appendix B: Matlab code used in this thesis*

```

%% alpha values

load_guess;

T_range = 10:10:150;
D_range = [5 10 20 30 40 50];
D_range = 50;
ifitts = 1;
% for T_fitts = T_range
for D_scan = D_range

    pars.D = D_scan;
%     pars.T = 2.7 * pars.D + 23;

    scan_control = [];

    %%%%%%%%%%%%%%%%%%%%%%%%%%%%%%%%%%%%%%%%%%%%%%%%%%%%%%%%%%%%%%%%%%%%%%%%%
    %% SIMULATION SETUP (EDIT THESE)
    %%%%%%%%%%%%%%%%%%%%%%%%%%%%%%%%%%%%%%%%%%%%%%%%%%%%%%%%%%%%%%%%%%%%%%%%%

    % rand('state',1);
    % randn('state',1);

    pars.M = 100;

    x0 = [0;0];

    alp_range =[0.51 0.55:0.05:1];    %% used to generate Fig. 1

    alp_range = 1;                %% set this for alpha

    %%%%%%%%%%%%%%%%%%%%%%%%%%%%%%%%%%%%%%%%%%%%%%%%%%%%%%%%%%%%%%%%%%%%%%%%%
    %% OPTIONS
    %%%%%%%%%%%%%%%%%%%%%%%%%%%%%%%%%%%%%%%%%%%%%%%%%%%%%%%%%%%%%%%%%%%%%%%%%

    ntrials = 10;    %10

    calculate_mean_variance = 1;
    calculate_partial_cost = 1;
    use_beta_pulse_solution = 0;
    plot_sample_mean_variance = 1;

    %% when use_HW_solution = 1, then alp=1 is used for calculation of
control
    %% signal

    use_HW_solution = 0;

    print_figures = 0;

    %%%%%%%%%%%%%%%%%%%%%%%%%%%%%%%%%%%%%%%%%%%%%%%%%%%%%%%%%%%%%%%%%%%%%%%%%
    %% DERIVED QUANTITIES
    %%%%%%%%%%%%%%%%%%%%%%%%%%%%%%%%%%%%%%%%%%%%%%%%%%%%%%%%%%%%%%%%%%%%%%%%%

    t_end = pars.T + pars.R;
    t = dt:dt:t_end;

```

*Appendix B: Matlab code used in this thesis*

```

iT = round(pars.T/dt);
k= pars.noise_scale^2/dt;
nsteps = round(t_end/dt);

lam_hold = pars.D/(pars.tau_1*pars.tau_2*pars.tau_3);

A = eye(2) + dt*[0 1; -1/(pars.tau_1*pars.tau_2) -
(pars.tau_1+pars.tau_2)/(pars.tau_1*pars.tau_2)];
B = dt*[0; pars.tau_3];

a_1 = -1/(pars.tau_1*pars.tau_2);
a_2 = -(pars.tau_1+pars.tau_2)/(pars.tau_1*pars.tau_2);
a_3 = pars.tau_3;
sqdt = sqrt(dt);

csi_opt = zeros(length(alp_range),1);
eta_opt = zeros(length(alp_range),1);

%%%%%%%%%%%%%%%%%%%%%%%%%%%%%%%%%%%%%%%%%%%%%%%%%%%%%%%%%%%%%%%%%%%%%%%%
%% GRAPHICS
%%%%%%%%%%%%%%%%%%%%%%%%%%%%%%%%%%%%%%%%%%%%%%%%%%%%%%%%%%%%%%%%%%%%%%%%

font_size = 28;
linewidth_1 = 2;
linewidth_2 = 0.5;
axis_linewidth = 1;

%%%%%%%%%%%%%%%%%%%%%%%%%%%%%%%%%%%%%%%%%%%%%%%%%%%%%%%%%%%%%%%%%%%%%%%%
%% RUN
%%%%%%%%%%%%%%%%%%%%%%%%%%%%%%%%%%%%%%%%%%%%%%%%%%%%%%%%%%%%%%%%%%%%%%%%

ii_scan = 1;
for alp = alp_range

    if use_HW_solution
        alp_calc = 1;
    else
        alp_calc = alp;
    end

    if (alp>=0.5) | (use_HW_solution)
        %% find an ordinary solution

        %% set initial point for optimizations by interpolating
        between stored guesses
        csi_0 = spline(pars.guess_points(:,1),
pars.guess_points(:,2), alp_calc);
        eta_0 = spline(pars.guess_points(:,1),
pars.guess_points(:,3), alp_calc);

        %% solve nonlinear equations for (csi, eta) and compute
        control signal
        [lam_star, csi, eta] = solve_optimal_lambda(pars.D, pars.T,
pars.R, alp_calc, pars.tau_1, pars.tau_2, pars.tau_3, t, csi_0, eta_0);
        lam_star = lam_star';

```

*Appendix B: Matlab code used in this thesis*

```

    %% concatenate hold-on solution in the post-movement period
    lam_star((iT+1):end) = lam_hold;

    %% store csi, eta solution
    csi_opt(ii_scan) = csi;
    eta_opt(ii_scan) = eta;

    SIGNAL = lam_star;
    NOISE   = abs(lam_star).^alp;

else
    %% find Young measure solution

    w1 = (1/pars.tau_1) * exp((t-pars.T)/pars.tau_1);
    w2 = (1/pars.tau_2) * exp((t-pars.T)/pars.tau_2);
    w1sq = 1/(2*pars.tau_1) * (1-exp(-2*pars.T/pars.tau_1));
    w2sq = 1/(2*pars.tau_2) * (1-exp(-2*pars.T/pars.tau_2));
    w1w2 = 1/(pars.tau_1+pars.tau_2) * (1-exp(-
pars.T*(pars.tau_1+pars.tau_2)/(pars.tau_1*pars.tau_2)));
    W = [w1sq w1w2; w1w2 w2sq];
    xi = (1/pars.M) * lam_hold * inv(W) * [1; 1];
    beta_t = xi(1) * w1' + xi(2) * w2';
    beta_t((iT+1):end) = (1/pars.M) * lam_hold;           %% hold-on

control

    %%         if use_beta_pulse_solution>0
    %%             [t_1, t_2 ] = optimal_beta(pars)
    %%             beta_t = zeros(size(beta_t));
    %%             beta_t((t<t_1)) = 1;
    %%             beta_t((t>t_2)&(t<pars.T)) = -1;
    %%             beta_t((t>=pars.T)) = (1/pars.M) * lam_hold;
    %%         end

    SIGNAL = pars.M*beta_t;
    NOISE   = (pars.M^alp)*sqrt(abs(beta_t));

end

if use_HW_solution
    beta_t = SIGNAL/pars.M;
    NOISE   = (pars.M^alp)*sqrt(abs(beta_t));
end

%%%%%%%%%%%%%%%%%%%%%%%%%%%%%%%%%%%%%%%%%%%%%%%%%%%%%%%%%%%%%%%%%%%%%%%%
%% PLOT CONTROL SIGNAL
%%%%%%%%%%%%%%%%%%%%%%%%%%%%%%%%%%%%%%%%%%%%%%%%%%%%%%%%%%%%%%%%%%%%%%%%

if alp>=0.5

    %% Agonist
    hfig_11 = figure(11);
    hh = plot(t,SIGNAL.*(SIGNAL>0), 'LineWidth', linewidth_1);
    xlim([0 pars.T+pars.R]);
    xlabel('Time (ms)', 'FontSize', font_size);

```

*Appendix B: Matlab code used in this thesis*

```

        ylabel('Agonist signal', 'FontSize', font_size)
        set(gca, 'FontSize', font_size, 'Linewidth', axis_linewidth,
'TickDir', 'out')
        box off

        %% Antagonist
        hfig_12 = figure(12);
        plot(t,-SIGNAL.*(SIGNAL<0), 'LineWidth', linewidth_1);
        xlim([0 pars.T+pars.R]); ylabel('Antagonist signal',
'FontSize', font_size);
        xlabel('Time (ms)', 'FontSize', font_size);
        set(gca, 'FontSize', font_size, 'Linewidth', axis_linewidth,
'TickDir', 'out')
        box off

    else

        %% Agonist
        hfig_11 = figure(11);
        hh = plot(t,beta_t, 'LineWidth', linewidth_1);
        xlim([0 pars.T+pars.R]);
        xlabel('Time (ms)', 'FontSize', font_size);
        ylabel('\beta(t)', 'FontSize', font_size)
        set(gca, 'FontSize', font_size, 'Linewidth', axis_linewidth,
'TickDir', 'out')
        box off

    end

    drawnow

    %%%%%%%%%%%%%%%%%%%%%%%%%%%%%%%%%%%%%%%%%%%%%%%%%%%%%%%%%%%%%%%%%%%%%%%%%
    %% THEOR. VARIANCE AT END-POINT
    %%%%%%%%%%%%%%%%%%%%%%%%%%%%%%%%%%%%%%%%%%%%%%%%%%%%%%%%%%%%%%%%%%%%%%%%%

    interval_integration = 1:iT;
    t_integration = pars.T - dt*interval_integration;
    endpoint_var(ii_scan) = pars.tau_3^2 * pars.noise_scale^2 * dt
* sum((NOISE(1:iT).^2)'.*(b_12(t_integration, pars.tau_1,
pars.tau_2).^2 ) );

    %%%%%%%%%%%%%%%%%%%%%%%%%%%%%%%%%%%%%%%%%%%%%%%%%%%%%%%%%%%%%%%%%%%%%%%%%
    %% THEOR. MEAN AND VARIANCE PROFILES
    %%%%%%%%%%%%%%%%%%%%%%%%%%%%%%%%%%%%%%%%%%%%%%%%%%%%%%%%%%%%%%%%%%%%%%%%%

    if calculate_mean_variance>0

        disp('Calculating theor. mean and variance, please
wait...');

        At = eye(2);
        a_t = zeros(2, nsteps);
        b_t = zeros(2,2,nsteps);
        c_t = zeros(1,nsteps);

        %% Define Propagators
        for isteps = 1:nsteps

```

*Appendix B: Matlab code used in this thesis*

```

        a_t(:, isteps) = At*B;      %% mean
        b_t(:, :, isteps) = (At*B)*(At*B)';    %% covariance
        At = A*At;
    end
    c_t = reshape(b_t(1,1,:), [1 nsteps]);

    %% for a delta-signal at 0
    % Varx_T = k*c_t(iT) * Pulse_amp(1);

    x_t = zeros(2,nsteps);
    Ex_t = zeros(2,nsteps);
    Varx_t = zeros(1,nsteps);

    if calculate_partial_cost>0

        NOISE_CUT = NOISE;
        NOISE_CUT((iT+1):end) = 0;
        for isteps = 1:nsteps
            Ex_t(:,isteps) = a_t(:,isteps:-
1:1)*SIGNAL(1:isteps);
            Varx_t(isteps) = c_t(isteps:-
1:1)*k*(NOISE_CUT(1:isteps)).^2;
        end

    else

        for isteps = 1:nsteps
            Ex_t(:,isteps) = a_t(:,isteps:-
1:1)*SIGNAL(1:isteps);
            Varx_t(isteps) = c_t(isteps:-
1:1)*k*(NOISE(1:isteps)).^2;
        end

    end

    %% check with calculation above
    %     endpoint_var(ii_scan) = Varx_t(iT);

    Cost(ii_scan) = sum(Varx_t(iT:end)*dt);

    %%%%%%%%%%%%%%%%%%%%%%%%%%%%%%%%%%%%%%%%%%%%%%%%%%%%%%%%%%%%%%%%%%%%%%%%%
    %% PLOT MEAN AND VARIANCE PROFILES
    %%%%%%%%%%%%%%%%%%%%%%%%%%%%%%%%%%%%%%%%%%%%%%%%%%%%%%%%%%%%%%%%%%%%%%%%%

    %% Trajectory mean and STD
    hfig_21 = figure(21);
    hold on
    plot(t, Ex_t(1,:), 'LineWidth', linewidth_1, 'Color', 'r')
    plot(t, Ex_t(1,:) + sqrt(Varx_t), 'LineWidth', linewidth_1,
'Color', 'r', 'LineStyle', '--')
    plot(t, Ex_t(1,:) - sqrt(Varx_t), 'LineWidth', linewidth_1,
'Color', 'r', 'LineStyle', '--')
    plot(pars.T, pars.D, 'Marker','o', 'MarkerSize',8, 'Color',
'r', 'MarkerFaceColor', 'w');
    xlabel('Time (ms)', 'FontSize', font_size);

```

*Appendix B: Matlab code used in this thesis*

```

        ylabel('Position (deg)', 'FontSize', font_size);
        set(gca, 'LineWidth', axis_linewidth, 'FontSize',
font_size);
        hold off

        %% Velocity mean profile
        hfig_22 =figure(22);
        hold on
        plot(t, Ex_t(2,:)*1e3, 'LineWidth',
linewidth_1, 'Color', 'r');
        xlabel('Time (ms)', 'FontSize', font_size);
        ylabel('Velocity (deg\cdot s^{-1})', 'FontSize', font_size);
        set(gca, 'LineWidth', axis_linewidth, 'FontSize',
font_size);
        hold off

        %% Positional variance
        hfig_23 =figure(23);
        hold on
        plot(t,Varx_t, 'LineWidth', linewidth_1 )
        xlabel('Time (ms)', 'FontSize', font_size);
        ylabel('Pos. variance (deg^2)', 'FontSize', font_size);
        set(gca, 'LineWidth', axis_linewidth, 'FontSize',
font_size);
        hold off

        fprintf(1, 'alpha = %f \t Cost = %f \t Endpoint Variance
= %f \n', ...
                alp, Cost(ii_scan), endpoint_var(ii_scan));

    end

    drawnow

%     disp('Generating sample trajectories');
%     pause(0.5)

%%%%%%%%%%%%%%%%%%%%%%%%%%%%%%%%%%%%%%%%%%%%%%%%%%%%%%%%%%%%%%%%%%%%%%%%
%% GENERATE SAMPLE TRAJECTORIES
%%%%%%%%%%%%%%%%%%%%%%%%%%%%%%%%%%%%%%%%%%%%%%%%%%%%%%%%%%%%%%%%%%%%%%%%

sample_mean      =    0;
sample_var       =    0;

if ntrials>0

    hfig_31 = figure(31);
    haxes_31 = axes;
    set(haxes_31 , 'NextPlot', 'add');
    set(haxes_31, 'LineWidth', axis_linewidth, 'FontSize',
font_size);
    xlabel('Time (ms)', 'FontSize', font_size);
    ylabel('Position (deg)', 'FontSize', font_size);

    hfig_32 = figure(32);
    haxes_32 = axes;
    set(haxes_32, 'NextPlot', 'add');

```

*Appendix B: Matlab code used in this thesis*

```

set(haxes_32, 'LineWidth', axis_linewidth, 'FontSize',
font_size);
xlabel('Time (ms)', 'FontSize', font_size);
ylabel('Velocity (deg\cdot s^{-1})', 'FontSize', font_size);

x_endpoint = zeros(ntrials,1);
v_endpoint = zeros(ntrials,1);

Xt = zeros(nsteps+1,1);
Vt = zeros(nsteps+1,1);
Xt_mean = zeros(size(Xt));
Vt_mean = zeros(size(Vt));

for itrial = 1:ntrials

    dB = sqdt*randn(nsteps,1);
    Vt(1) = 0;
    Xt(1) = 0;
    for isteps = 1:nsteps
        Xt(isteps+1) = Xt(isteps) + Vt(isteps) *dt;
        Vt(isteps+1) = Vt(isteps) + dt*(a_1*Xt(isteps) +
a_2*Vt(isteps) + a_3*SIGNAL(isteps))
+pars.noise_scale*a_3*NOISE(isteps)*dB(isteps);
    end
    Xt_mean = (itrial-1)/itrial * Xt_mean + Xt/itrial;
    Vt_mean = (itrial-1)/itrial * Vt_mean + Vt/itrial;
    x_endpoint(itrial) = Xt(iT+1);
    v_endpoint(itrial) = Vt(iT+1);

    figure(hfig_31);
    plot([0 t], Xt, 'LineWidth', 1)
    plot(pars.T, x_endpoint(itrial), 'LineStyle',
'none', 'Marker', '.')

    figure(hfig_32);
    plot([0 t], Vt*1e3, 'LineWidth', 1)

end

sample_mean = mean(x_endpoint);
sample_var = var(x_endpoint);

if plot_sample_mean_variance>0

    figure(hfig_31);
    plot([0 t], Xt_mean, 'r' )

    figure(hfig_32);
    plot([0 t], Vt_mean*1e3, 'r' )

end

% %% OVERLAY THEOR. MEAN AND VARIANCE
if calculate_mean_variance>0
    figure(hfig_31);

```

*Appendix B: Matlab code used in this thesis*

```

        plot(t, Ex_t(1,:), 'LineWidth', linewidth_1, 'Color',
'r');
        plot(pars.T, pars.D, 'Marker','o', 'MarkerSize',8,
'Color', 'r', 'MarkerFaceColor', 'w');
        hold off;

        figure(hfig_32);
        plot(t, Ex_t(2, :)*1e3, 'LineWidth', linewidth_1,
'Color', 'r');
        hold off
    end

        %         subplot(2,2,3);
        %         plot(t,SIGNAL); xlim([0 pars.T+pars.R]);
ylabel('\lambda^(t)', 'FontSize', font_size); xlabel('Time (ms)',
'FontSize', font_size);
        %         subplot(2,2,4);
        %         plot(t,SIGNAL); xlim([0 pars.T+pars.R]);
ylabel('Signal', 'FontSize', font_size); xlabel('Time (ms)', 'FontSize',
font_size);
        %         drawnow;

        fprintf(1,'alpha = %f \t Mean[X(T)] = %f \t Var[X(T)] = %f
\n', alp, sample_mean, sample_var);

    end

    scan_control(:,ii_scan) = SIGNAL;

    ii_scan = ii_scan + 1;
end %% end loop over alpha

%%%%%%%%%%%%%%%%%%%%%%%%%%%%%%%%%%%%%%%%%%%%%%%%%%%%%%%%%%%%%%%%%%%%%%%%
%% PLOT ERROR VS. ALPHA
%%%%%%%%%%%%%%%%%%%%%%%%%%%%%%%%%%%%%%%%%%%%%%%%%%%%%%%%%%%%%%%%%%%%%%%%

if length(alp_range)>1
    figure(4)
    plot(alp_range, endpoint_var, '-o' ); xlabel('\alpha',
'FontSize', font_size); ylabel('Var(x(T))', 'FontSize', font_size)
    figure(5)
    plot(alp_range, Cost, '-o' ); xlabel('\alpha');
ylabel('I(\lambda^*)', 'FontSize', font_size)
end

if print_figures>0

    string_eps= strcat('alp_', num2str(alp), 'M_',
num2str(pars.M), '.eps');
    string_fig= strcat('alp_', num2str(alp), 'M_',
num2str(pars.M), '.fig');

    if alp>=0.5

        filename = strcat('agonist_',string_eps);

```

*Appendix B: Matlab code used in this thesis*

```

print(hfig_11, '-depsec', filename);
filename = strcat('agonist_',string_fig);
saveas(hfig_11, filename);

filename = strcat('antagonist_',string_eps);
print(hfig_12, '-depsec', filename);
filename = strcat('antagonist_',string_fig);
saveas(hfig_12, filename);

else

filename = strcat('beta_',string_eps);
print(hfig_11, '-depsec', filename);
filename = strcat('beta_',string_fig);
saveas(hfig_11, filename);

end

if calculate_mean_variance>0

filename = strcat('traj_',string_eps);
print(hfig_21, '-depsec',filename);

filename = strcat('velprof_',string_eps);
print(hfig_22, '-depsec',filename);

filename = strcat('posvar_',string_eps);
print(hfig_23, '-depsec',filename);

filename = strcat('traj_',string_fig);
saveas(hfig_21,filename);

filename = strcat('velprof_',string_fig);
saveas(hfig_22, filename);

filename = strcat('posvar_',string_fig);
saveas(hfig_23 ,filename);

end

if ntrials>0

filename = strcat('sampletraj_',string_eps);
print(hfig_31, '-depsec',filename);

filename = strcat('samplelevel_',string_eps);
print(hfig_32, '-depsec',filename);

filename = strcat('sampletraj_',string_fig);
saveas(hfig_31, filename);

filename = strcat('samplelevel_',string_fig);
saveas(hfig_32, filename);

end

```

*Appendix B: Matlab code used in this thesis*

```

    end

    res_fitts(ifitts) = Cost;
    ifitts = ifitts + 1;
end

return

figure; plot(log2(2*pars.D./res_fitts), T_fitts_range, '-o')

```

---

```

function [y , csi, eta] = solve_optimal_lambda1(D, T, R, alp, tau_1,
tau_2, tau_3, s)

TOLERANCE = 1e-6;
%%%%%%%%%%%%%%%%%%%%%%%%%%%%%%%%%%%%%%%%%%%%%%%%%%%%%%%%%%%%%%%%%%%%%%%%
%  CONSTANTS
%%%%%%%%%%%%%%%%%%%%%%%%%%%%%%%%%%%%%%%%%%%%%%%%%%%%%%%%%%%%%%%%%%%%%%%%
bet = -1/(2*alp-1);
%% CHECKED OK
C1 = D/(tau_2*tau_3)*exp(T/tau_1);
C2 = D/(tau_1*tau_3)*exp(T/tau_2);
C3 = (tau_1*tau_2)/(tau_2-tau_1);
tau_12 = (tau_1 * tau_2)/(tau_1 + tau_2);
%%%%%%%%%%%%%%%%%%%%%%%%%%%%%%%%%%%%%%%%%%%%%%%%%%%%%%%%%%%%%%%%%%%%%%%%
% SOLUTION OF THE SYSTEM
%%%%%%%%%%%%%%%%%%%%%%%%%%%%%%%%%%%%%%%%%%%%%%%%%%%%%%%%%%%%%%%%%%%%%%%%
    %quadl-numerical calculate integral
    K11 = quadl( @phi_1, 0, T, TOLERANCE, [], bet, T, R, tau_1,
tau_2, tau_12, C3);
    K22 = quadl( @phi_2, 0, T, TOLERANCE, [], bet, T, R, tau_1,
tau_2, tau_12, C3);
    K12 = quadl( @phi_12, 0, T, TOLERANCE, [], bet, T, R, tau_1,
tau_2, tau_12, C3);

    detK = K11*K22 - K12*K12;%because as below: (but A(csi, eta)
into the constraint Eq(21)
    %csi * K11 + eta * K12 = C1;
    %csi * K12 + eta * K22 = C2;

    csi = (K22*C1 - K12*C2)/detK;
    eta = (K11*C2 - K12*C1)/detK;

    y = (csi*exp(s/tau_1) + eta*exp(s/tau_2)).*phi(s, bet, T, R,
tau_1, tau_2, tau_12, C3);

%%%%%%%%%%%%%%%%%%%%%%%%%%%%%%%%%%%%%%%%%%%%%%%%%%%%%%%%%%%%%%%%%%%%%%%%
function y = phi(s, bet, T, R, tau_1, tau_2, tau_12, C3)
%this is the integration of b12^2 part with power -1/(2\alpha-1)
%Eq(7) last term
b = 4*tau_12*(exp(-(T+R-s)/tau_12)-exp(-(T-s)/tau_12)) ...
-tau_2*(exp(-2*(T+R-s)/tau_2)-exp(-2*(T-s)/tau_2)) ...
-tau_1*(exp(-2*(T+R-s)/tau_1)-exp(-2*(T-s)/tau_1));

```

*Appendix B: Matlab code used in this thesis*

```

y = (0.5*(C3^2)*b).^bet;

%%%%%%%%%%%%%%%%%%%%%%%%%%%%%%%%%%%%%%%%%%%%%%%%%%%%%%%%%%%%%%%%%%%%%%%%

function y = phi_1(s, bet, T, R, tau_1, tau_2, tau_12, C3)

b = 4*tau_12*(exp(-(T-s+R)/tau_12)-exp(-(T-s)/tau_12)) ...
    -tau_2*(exp(-2*(T-s+R)/tau_2)-exp(-2*(T-s)/tau_2)) ...
    -tau_1*(exp(-2*(T-s+R)/tau_1)-exp(-2*(T-s)/tau_1)); % int^(T+R)_
b12(t-s)^2 dt

y = exp(2*s/tau_1).*((0.5*C3^2)*b).^bet;

%%%%%%%%%%%%%%%%%%%%%%%%%%%%%%%%%%%%%%%%%%%%%%%%%%%%%%%%%%%%%%%%%%%%%%%%

function y = phi_2(s, bet, T, R, tau_1, tau_2, tau_12, C3)

b = 4*tau_12*(exp(-(T-s+R)/tau_12)-exp(-(T-s)/tau_12)) ...
    -tau_2*(exp(-2*(T-s+R)/tau_2)-exp(-2*(T-s)/tau_2)) ...
    -tau_1*(exp(-2*(T-s+R)/tau_1)-exp(-2*(T-s)/tau_1));

y = exp(2*s/tau_2).*((0.5*C3^2)*b).^bet;

%%%%%%%%%%%%%%%%%%%%%%%%%%%%%%%%%%%%%%%%%%%%%%%%%%%%%%%%%%%%%%%%%%%%%%%%

function y = phi_12(s, bet, T, R, tau_1, tau_2, tau_12, C3)

b = 4*tau_12*(exp(-(T-s+R)/tau_12)-exp(-(T-s)/tau_12)) ...
    -tau_2*(exp(-2*(T-s+R)/tau_2)-exp(-2*(T-s)/tau_2)) ...
    -tau_1*(exp(-2*(T-s+R)/tau_1)-exp(-2*(T-s)/tau_1));

y = exp(s/tau_12).*((0.5*C3^2)*b).^bet;

```